UNIVERSITÀ DI PARMA

UNIVERSITA' DEGLI STUDI DI PARMA

DOTTORATO DI RICERCA IN
"*Scienza e tecnologia dei materiali*"

CICLO XXXI

Computer simulation and experimental investigation of materials for the organic memristive device

Coordinatore:
Chiar.mo Prof. Enrico Dalcanale

Tutore:
Dr. Victor Erokhin

Co-Tutore:
Dr. Silvia Battistoni

Dottoranda: Regina Burganova

Anni 2015/2018

Сначала ты теряешь всякую надежду, а потом все складывается как нельзя лучше (с) А.К.

Abstract

This thesis reports the results obtained during three years of PhD program in a co-tutorship agreement between Parma University (under the supervision of Prof. Victor Erokhin and cosupervision of Dr. Silvia Battistoni) and Kazan Federal University (under the supervision of Prof. Dmitrii Tayurskii). This research is focused on a combined theoretical and experimental study of materials for the organic memristive devices, namely, solid polyelectrolyte optimization towards design the device with improved characteristics starting from the optimization of materials and their properties. Poly(ethylene oxide)(PEO)-based solid polyelectrolyte is a medium providing reversible redox reactions in the acrive zone of the organic memristive device, composed of the thin polyaniline (PANI) film. Ionic transport in the solid polyelectrolyte media is a key characteristic responsible for the improved response speed ot the device. Polyelectrolyte structure mostly defines ionic movements, thus it should be constant over time and from sample to sample to provide endurance and reproducibility of the organic memristive device.

Initially, the study was addressed to probing the lithium transport in PEO using pulsed gradient field nuclear magnetic resonance technique. Then, using molecular dynamics simulations with a simple amorphous polyelectrolyte model we have investigated polyelectrolyte structure and lithium transport, revealing water content effect on these properties. X-ray diffractometry was used to examine polyelectrolyte composition of real systems and confirmed the results of the simulations. Further, electrochemical characterization of the polyelectrolyte/electrode and polyelectrolyte/PANI-coated electrode was done.

Taking into account the results of the complex theoretical and experimental studies, the organic memristive device, fabricated using the polyelectrolyte, containing half of the standard lithium salt concentration, was characterized. The improvement of its kinetic properties was explained in terms of the underlying ionic transport.

Table of Contents

List of Figures

List of Tables

Chapter 1

Introduction

1.1 Organic memristive device: component materials and working principle

Since the first statement of implementation of the memristor [1], predicted in 1971 by Chua [2], this area of research is increasingly evolving every year. Such interest is caused by the possibility to realize a new generation of computational systems. Similarly to the brain, these systems will combine functions of memory and information processing in a unit block, that provides learning. Similar properties are known in artificial neural networks, realized in the software, but memristors allow to build a completely new computer architecture, implying memory and processing in one physical element.

Organic memrisitve device (OMD) [3] was designed in 2005. Due to its organic realization, instead of inorganic, and pronounced ability to change its internal resistance depending on ionic charge that has passed through the element, it allows to consider the device as a synthetic analogue of biological synapse. Since its invention, OMD was used to realize logic elements with memory [4], adaptive network [5] and perceptron model [6, 7]. These applications show strong potential in future realization of the device as an element of neural networks.

The schematic representation of OMD and its connection to the external circuit are shown in Fig.1.1. The device is composed of a polymeric thin film – polyaniline (PANI) or polyaniline-based heterostructure (PANI-PSS composition

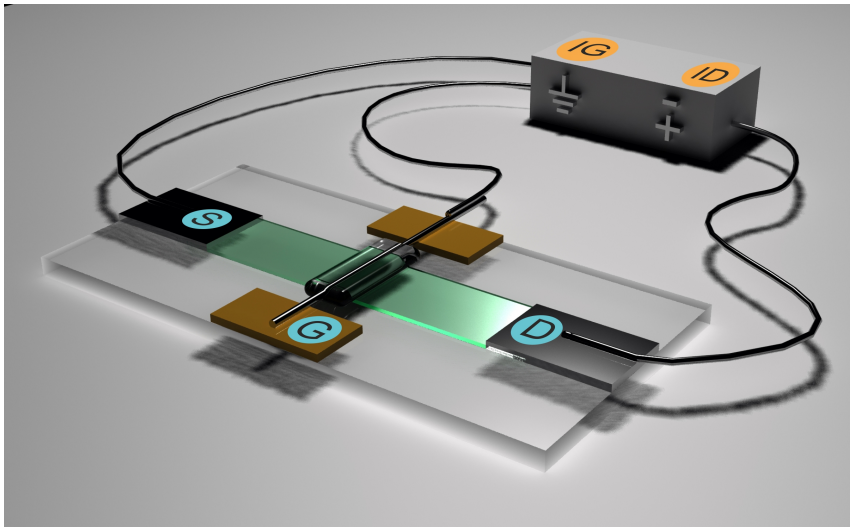

Figure 1.1. The schematic representation of organic memristive device

has been used to realize the device [8]), that forms conducting channel of OMD – contacting in the middle with solid polyelectrolyte, namely, lithium perchlorate ($LiClO_4$) doped poly(ethylene oxide) (PEO).

Polyaniline is the base material of the device. It represents a class of conducting polymers, intensively investigated in the past [9]. PANI possesses different intrinsic oxidation states, defining its conducting properties [10]. For instance, the working principle of the device is a result of reversible redox reactions, alternating PANI between conducting emeraldine salt (ES) and insulating leucoemeraldine base (LB) forms (Fig.1.2). This transformations, underlying the operation of the device, take place in the channel, formed at the junction of PANI and the polyelectrolyte, and called the active zone of OMD.

The connection of the device to the external circuit is divided by two branches – one is implemented through source (S) and drain (D) electrodes, and the second through the active zone of PANI and gate (G) electrode composed of silver wire (Fig.1.1). Even if the final state of the device is evaluated by measuring S-D current, gate current provides the complete picture on mechanism, controlling operation of the device. Generally, the conductivity of the active zone strongly depends on passed ionic charge, since ionic influx and outflux is controlled by redox reactions, alternating PANI between conducting and insulating states. This relation was confirmed by X-ray fluorescence measurements [11], and the following

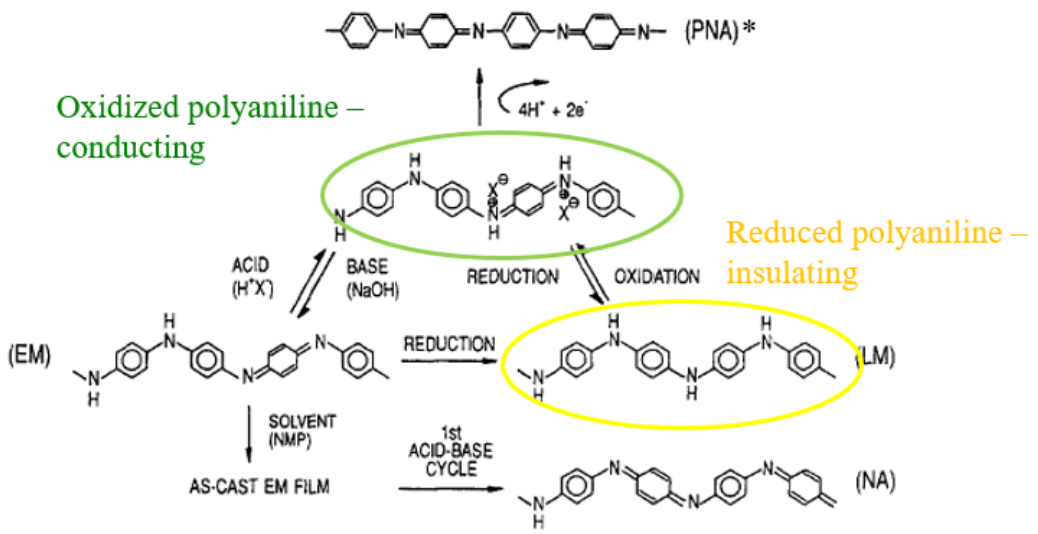

Figure 1.2. Different intrinsic states of PANI and transformations between them [10]

redox reaction was suggested as determining working principle of OMD:

$$PANI^{+} : Cl + Li^{+} + e^{-} \leftrightarrow PANI + Li^{+} + Cl^{-}. \tag{1.1}$$

This reaction shows that ionic flux provided by lithium ions to and from PANI active layer play an important role in the entire system. PEO-based polyelectrolyte serves as a source of ions and medium to move. From this point, the role of the polyelectrolyte is also defined as important. And the present research will consider possible ways towards improvement of characteristics of OMD by optimizing materials, particularly, starting with the polyelectrolyte medium.

Before the final formulation of the goals of the present research, the necessary framework regarding to component materials of OMD is provided in the next two sections.

1.2 Solid polymer electrolytes

Generally, solid polymer electrolytes (SPE) are well-known materials used as an alternative to conventional liquid electrolytes in secondary lithium-ion battery technologies [12]. Commonly, SPEs are composed by dissolving alkali metal salts in a polar polymer matrix. Polymer-based electrolytes, comparing to conventional

liquid ionic solutions, are favored due to their safety: no internal shorting, no leakage and nonflammable products of reaction on electrodes. Moreover, devices, fabricated using SPEs instead of liquid electrolytes can be mechanically flexible and advanced.

Poly(ethylene oxide) (PEO) has been intensively studied as the polymer host due to its low cost, electrochemical stability, non-toxicity, an easy processability and ability to dissolve a wide range of salts [13]. General chemical formula, describing PEO structure is expressed as $-(CH_2-CH_2-O)_n-$. It has a variety of available molecular weights ranging from 10^2 to 10^8 Da.

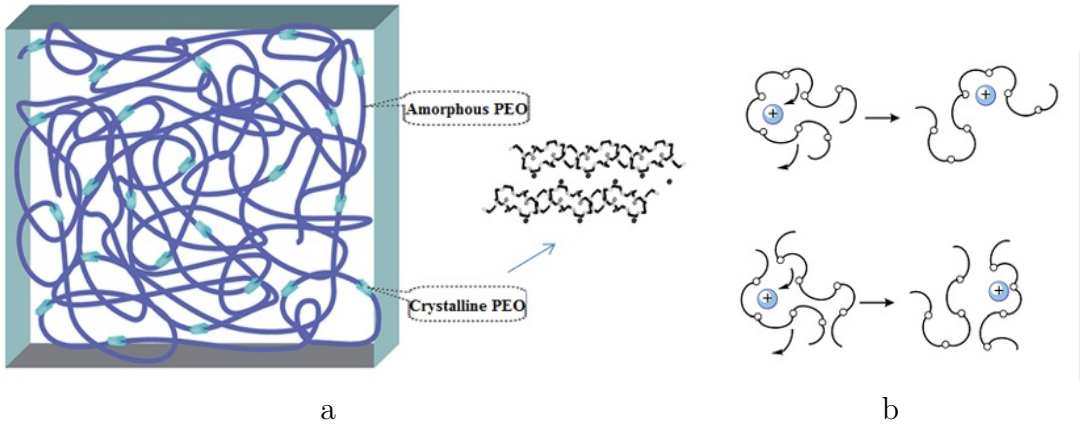

Figure 1.3. Multiphase structure of PEO-based polyelectrolytes at room temperature (a) and The mechanism of cationic transport in the amorphous phase (b) [12]

PEO-based solid polyelectrolytes has been widely investigated for different applications towards providing excellent ionic transport, because still they have relatively low ionic conductivity of the order of 10^{-8} S/cm at ambient temperature [14]. One of the major factors, arising this limitation is the polyelectrolyte structure, represented by coexisting amorphous and crystalline phases at room temperature (Fig.1.3a). And there are two principal mechanisms of ionic transport, corresponding to these phases.

According to the most common point of view on the conductivity mechanism, cation transport is coupled to PEO chains mobility. Namely, cations move consecutively associating and dissociating with coordinations made up ether oxygen ions of PEO with lone electron pairs (Fig.1.3b). Segmental relaxation of the polymer chain makes such movement between coordinations easier, so when a new energet-

ically more favorable coordination site appears, an cation hops there. Therefore, ionic conductivity can be improved by increasing the polymer chain mobility. This statement is supported by the fact that ionic conductivity is much lower, when ionic transport is depressed due to formation of PEO crystalline domains [15] (For instance, the ionic conductivity of a fully amorphous PEO-based polyelectrolyte is of order of 10^{-4} S/cm [14]). Consequently, many efforts to avoid PEO crystallization have been addressed to the possibility to increase mobility of PEO chains, or, in other words, to expand polyelectrolyte amorphous phase, using plastisizers [16, 17, 18] or nanofillers [19, 20, 21].

It was mentioned above, that ionic motion is coupled to polymer chain mobility, meaning that conductivity is higher in the amorphous phase. However, this belief has been contested, and it has been shown that in some cases conductivity is higher in the crystalline domains (polymer and cation motion is decoupled). It was found, that a crystalline polyelectrolyte, prepared using low molecular weight PEO (1000 Da) and $LiSbF_6$ salt, added in the concentration, corresponding to one Li ion per six ethylene oxide units of PEO (EO:Li ratio is 6:1) showed greater conductivity than fully amorphous analogue [22]. Using combined experimental and theoretical study (neutron diffraction and first principles calculations) the authors defined the structure of $(PEO)_6$:$LiSbF_6$ as pairs of PEO chains forming cylindrical tunnels. Cations are located inside these tunnels, and each lithium ion is coordinated by six ether oxygen ions, while anions are localized outside the tunnels. The conductivity appears as a direct ionic transport within the cylinders, aligned all together, that provides elevated ionic conductivity. Polyelectrolytes, sharing the same crystalline structure was found also for PEO, doped by $LiPF_6$ [23], $LiAsF_6$ [22] and LiTFSI [24] salts. At salt concentration, corresponding to 3:1 EO:Li ratio similar cylindrical structure, providing the pathways for lithium ions to promote, was found. In this phase PEO chain forms a helix, where lithium ions are coordinated by three ether oxygens and located within each turn of the chain [25]. The elevated ionic conductivity comparing to amorphous equivalent was found for $(PEO)_3$:LiTFSI [26], although similar structure was found also for PEO, doped by $LiAsF_6$ [27] and $LiBF_4$ [28] salts.

As discussed, these studies have shown that ionic conductivity is maintained and even enhanced in crystalline phase. But specific crystalline morphology defin-

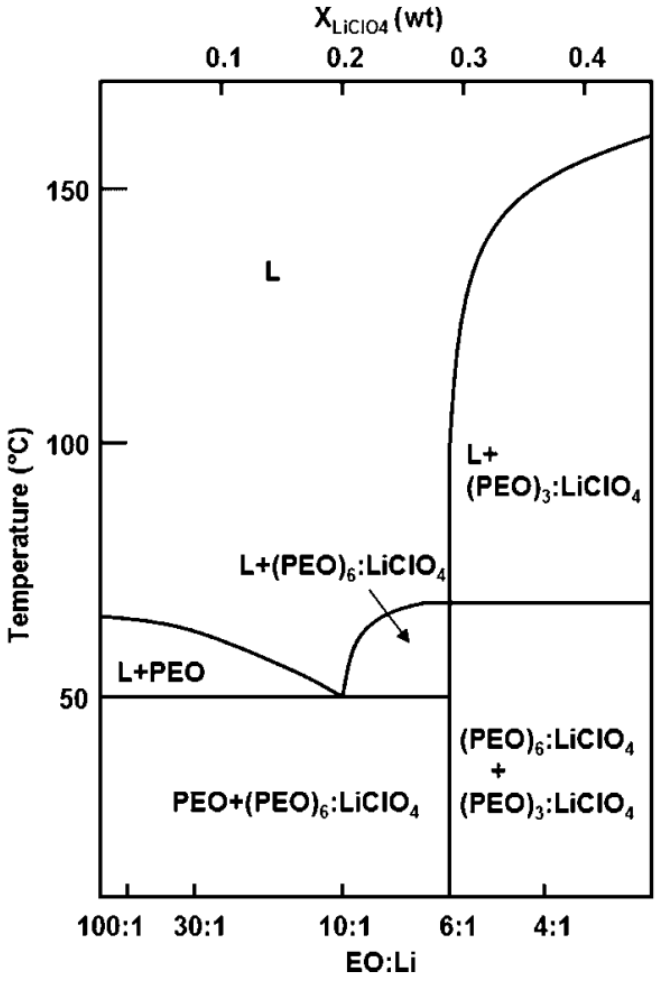

Figure 1.4. Phase diagram of PEO-$LiClO_4$ [22]; EO:Li refers to ratio between ether oxygen ions of PEO and lithium ions of salt; X_{LiClO4} represents the weight fraction of $LiClO_4$ salt

ing the large scale polyelectrolyte structure should also be taken into account, since lithium transport in PEO continuous as long as the conduction pathways exist over a large spatial scale.

Therefore, in general, polyelectrolyte phase behaviour through the temperature versus salt concentration dependence determines ionic mobility. Lithium perchlorate doped PEO, used as a component material of OMD, similarly to the most SPEs has a variety of different phases. As it is shown in the phase diagram in Fig.1.4, in a semicrystalline sample more than one crystalline phase can form [29, 30], in-

cluding pure PEO, $(PEO)_6$:$LiClO_4$ and $(PEO)_3$:$LiClO_4$ crystalline complexes. The last PEO complex has relatively high melting temperature – it keeps crystalline up to 150^0C, while the second melts at 50-65 ^{0}C depending on salt concentration. Above melting point PEO-$LiClO_4$ polyelectrolyte is fully amorphous. It is interesting, that crystallization of less concentrated $(PEO)_6$:$LiClO_4$ salt complex is delayed by days in vacuum and weeks in humid atmosphere [15], and the remnants of this structure persist even in amorphous phase [31]. However, no confirmation was found supporting the higher ionic conductivity in this crystalline phase [32], probably due to occurrence of not enough long paths for conduction.

In the context of the ionic conductivity in the PEO-salt systems, provided by specific phase, the particular attention should be addressed to effect of humidity, since PEO, as well as lithium salts have high hygroscopic nature. Generally, water increases the ionic conductivity in PEO-based polyelectrolytes by several orders of magnitude depending on salt concentration, cation-anion identity and water content [33, 34, 35, 36]. The contribution of water itself in total conductivity is insufficient. Different experimental techniques, including nuclear magnetic resonance [37], electron spin resonance [38], IR spectroscopy [39], and X-ray diffraction [39], have shown, that water diffuses into amorphous regions, containing dissolved salt and replaces anions. This replacement increases conductivity due to several reasons. First, water promotes salt clusters to break-up, that allows more salt dissociate and contribute to the conductivity. Second, it decreases interaction strength between cations and ether oxygen ions, coordinating with lithium. This leads to increased mobility of PEO chains, since less ether oxygens interact with lithium ions. Moreover, the size of the hydrated cations allowing to coordinate with more ether oxygens prevents chain folding, and consequently, pure PEO crystallization. In addition, it was demonstrated that in PEO-salt systems water destroys crystalline fraction more effectively, than in pure PEO. Namely, in the semicrystalline PEO-$Pb(CF_3SO_3)_2$ and PEO-$Zn(CF_3SO_3)_2$ systems (with EO:cation ratio 24:1) water incorporated in concentration EO:H_2O 1:1 completely destroys crystalline domains (initial fraction was 60%), while the same amount of water in pure PEO decreases crystallinity from 75 to 50%.

Hydrated complex is electrostatically neutral, when it is formed by a cation and four water molecules surrounding lithium ion [40, 41]. In this case water helps

to eliminate cation conduction, resulting in purely anionic transport [39].

Hydrated cations were also found in PEO-LiCl-water (with wt%=50) system [42] systems. Using Quasielastic Neutron Scattering and molecular dynamics methods authors have shown that besides lithium water hydrates PEO, increasing its mobility. Last case is associated with so called interfacial water in contrast to free or bulk water having faster dynamics. In addition, MD simulations suggest that smaller cation radius is a key factor to form hydrated cations, disrupting PEO-cation coordinations.

1.3 Conjugated polymers

Originally, polymeric materials were considered as insulators, since they are unable to carry electric charge. However, this belief was challenged after the discovery the particular class of polymers, which can behave as semiconductors or even demonstrate metallic behaviour under special treatment [9]. These polymers are intrinsically conductive, in contrast to polymer electrolytes, mentioned in the previous section, where conductivity was provided by introducing conducting species. Intrinsically conducting polymers are usually referred as conjugated polymers. Their structure is defined as alternating single-double bonds in the backbone: this sequence is formed by σ bonds between carbon atoms in sp^2p hybridization and unpaired π-electrons of out-of-plane p_z orbitals, continuously overlapping and forming conjugation. While σ-electrons are localized due to formation of covalent bonds, π-electrons can be delocalized upon doping, allowing charge to move freely along chains.

Polyaniline is a representative of conjugated polymers. Its general structural formula is shown in Fig.1.5. Unlike other members of this class of polymers PANI has several advantages, as environmental stability, controllable electrical conductivity, variety of redox states and high conductivity upon doping. Moreover, besides carbon, nitrogen atoms contribute to conjugation (A-B type of polymer).

As it was mentioned, PANI has different forms, defined by its oxidation state. Fully oxidized form is pernigraniline base (PANI PB), in general formula n=0 and m=1. In contrast fully reduced is leucoemeraldine base (PANI LB) with n=1, m=0. Half-oxidized state is emeraldine base (PANI EB) with n, m=0.5.

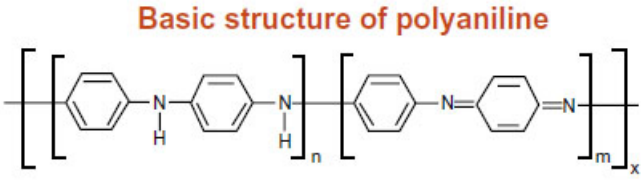

Figure 1.5. General structural formula of polyaniline

These PANI forms are non-conducting, but can be transferred to conducting state by doping. Generally, doping of conjugated polymers implies reversible charge-transfer chemistry: p-type doping in case of oxidation and n-type doping in case of reduction. In terms of band structure, similarly to semiconductors, doping involves occupation of defect levels. In contrast to semiconductors, these levels are symmetrically arranged in the band gap. Then, for example, when an electron is removed from the polymer chain (oxidation), the lowest state is occupied by a virtual particle, called positive polaron (negative in case of reduction). Positive polaron is a radical cation (radical anion in case of negative polaron), having half-integer spin and single electronic charge (positive or negative depending on polaron type). The formation of polarons is a result of the local geometrical relaxation of the bond lengths due to oxidation or reduction. Further oxidation leads to further occupation of polaron levels, and formation of two-polaron bound state due to enhanced geometrical relaxation of the bond lengths, or, in other words, lattice distortion. This bound state is called bipolaron – dication (or dianion when two negative polarons are bounded) that is spinless quasiparticle having double electronic charge (positive or negative depending on oxidation or reduction respectively). Bipolarons are found to be the main charge carriers in conjugated polymers, appearing due to lattice distortion, when structure rearranges to compensate charge created by its injection. However, this is not true for PANI. Electron Paramagnetic Resonance (EPR) signal was registered from conducting emeraldine salt sample, while no signal was expected, since bipolarons are spinless quasiparticles, thus they could not contribute to EPR signal [43]. Therefore, the conclusion was made that in PANI charge carriers are polarons.

Interestingly, PANI is the first conjugated polymer, transferred into conducting state by proton doping, implying acid-base chemistry. In fact, both mechanisms allow to obtain conducting ES form of PANI, with the only difference in initial

states. As it shown in Fig.1.6a, emeraldine salt can be obtained by the reduction of leucoemeraldine base form or proton doping of emeraldine base. The nature of the last mechanism was explained as a tree-step process (Fig.1.6b). First, PANI reacts with proton acid, that adds two protons per unit cell and bipolaron forms. But this bipolaron is unstable, thus bond length rearrangement is induced: quinoid ring relaxes to benzenoid, resulting in formation of two polarons. In the last step, polarons separate that leads to halving the unit cell [44].

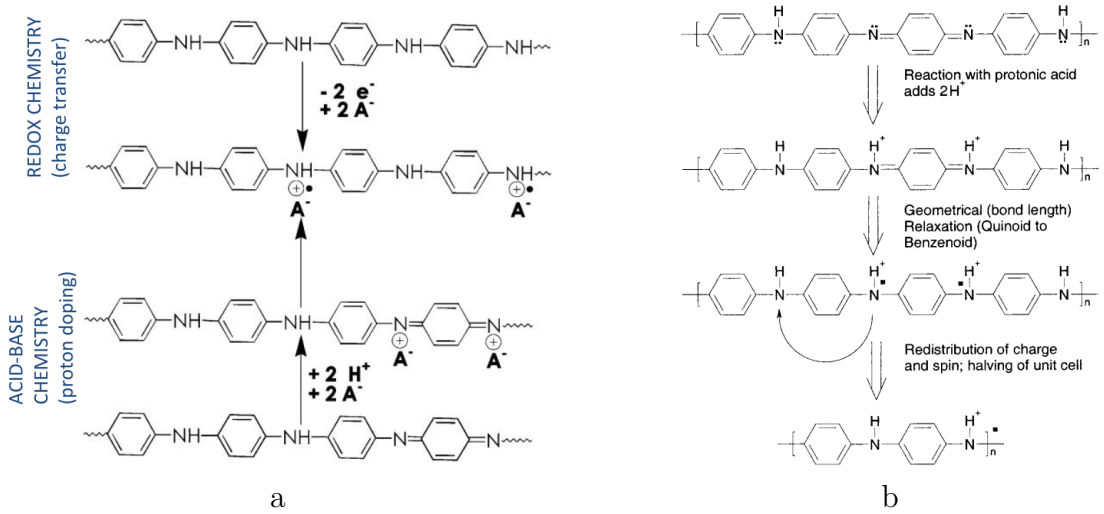

Figure 1.6. Two different mechanisms transferring PANI to its conductive ES form from LB or EB (a) and Three-step conversion of PANI EB into PANI ES form [44] (b)

In contrast to redox chemistry to transfer PANI into conducting state, although the protonation keeps constant the number of electrons in the polymer chain, it induces the rearrangement of electronic structure. Theoretically, this conversion has to transform PANI into polaronic metal and to change conductivity from 10^{-10} S/cm up to 400 S/cm. But typical conductivity of emeraldine salt samples, observed experimentally is 30 S/cm.

Depending on oxidation or doped-undoped state PANI has different colors ranging from yellow to purple. The full variety of polyaniline forms are presented in Fig.1.7.

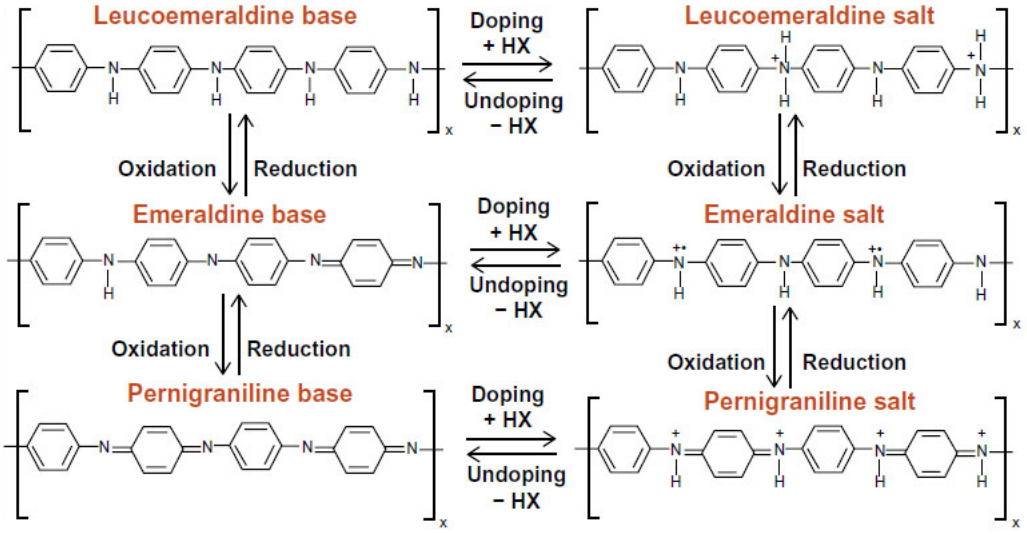

Figure 1.7. Variety of PANI forms includes undoped base and doped salt forms

1.4 Summary on component materials of organic memristive device

As it was mentioned in the Sec.1.1, the operation principle of OMD is considered to be based on transition of active layer of PANI between emeraldine salt and leucoemeraldine forms as a result of reversible reactions of Eq.1.1. It is important to notice, that these PANI transformations requires acidic environment, that, on the other hand, provides long-term persistence of proton doped ES state (detailed description of conducting channel fabrication is given in the Sec.2.1), which, in fact, tends to decrease with voltage cycling and time. This problem is usually referred as the polymer aging. In the short-term this problem is dissolved by adding hydrochloric acid to the composition of the polyelectrolyte.

The structure of real PEO-based polyelectrolytes, mainly defining their conductivity properties, are extremely complex to be predicted. When they applied as component materials of devices, the high attention should be paid to the effect of the humid atmosphere and time evolution of the structure, represented as amorphous and crystalline domains. Controlling this effects allow to design a reproducible and highly enduring device. The incorporation of hydrochloric acid can also influence the final structure of the polyelectrolyte, that defines its long-term

conducting properties. In its turn, ionic conductivity, as was mentioned before, can determine response speed of organic memristive device.

All these factors, defining the material properties have been considered in the whole in the present research towards optimization the working characteristics of OMD. Moreover, understanding how this factors influence the operation of OMD allows to develop a device with more stable and reproducible properties.

1.5 Motivation and Objectives

The **aim** of the present research is **to design an organic memristive device with improved working characteristics** starting from the optimization of materials and their properties. Namely, response speed, endurance and reproducibility are included in these improvements, motivated by the numerous applications in which this kind of elements are applied.

Memristors and memristive devices in general are widely considered as good candidates for memory elements due to their ability of having different internal resistive states that are accessible and modifiable with the operation of low voltage values. Thus, for employing organic memristors as memories, it is necessary to endow them to have a high response speed and high endurance in order to provide fast operation and safety of information. Same characteristics can be extended in the use of these devices as central elements for the realization of synaptic prosthesis: a high speed provides fast response, while high-level endurance keep usage of a prosthesis for a exploitation time. The most exciting application is related to use the memristor as a base elements in artificial neuronal networks, in which thousands of these elements are connected in circuits with the ability of classify input data. Therefore it is very important to provide a high reproducibility of the device properties, to ensure that every element of network has the same characteristics and to easily predict their behaviours. Possible applications of organic memristive device and required properties for their employment are shown in Fig.1.8.

We used combined theoretical and experimental methods in our research. Thesis organized is following. Chapter 2 describes fundamentals of experimental techniques, used in the present research. Chapter 3 gives the basic explanation of molecular dynamics method. Chapter 4 discusses the results of pulsed gradient

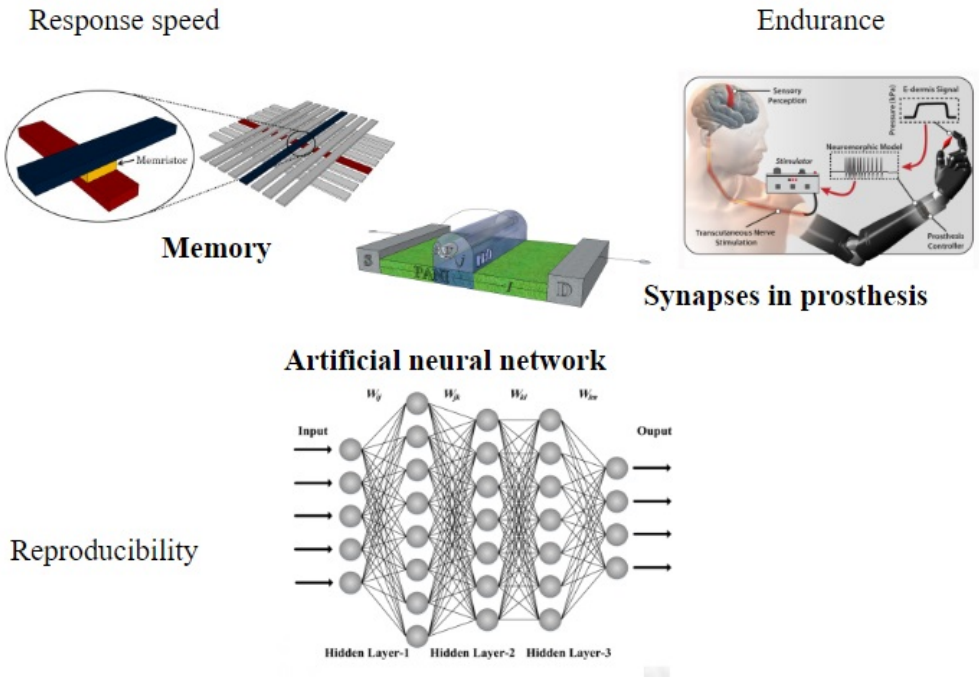

Figure 1.8. Possible applications of organic memristive device and required properties

field nuclear magnetic resonance study of PEO-$LiClO_4$ polyelectrolyte prepared using standard for OMD fabrication salt concentration in PEO. Molecular dynamics simulation results on the polyelectrolyte structure and lithium transport in PEO along with effect of different water concentration on this characteristics are presented in Chapter 5. The polyelectrolytes phase composition and electrochemical characterization depending on salt concentration are discussed in Chapters 6 and 7 as a results of X-ray diffractometry, optical microscopy and electrochemical impedance spectroscopy. Finally, using as a base of the results of previous chapters, we demonstrate the possibility of improving OMD kinetics in Chapter 8. The last Chapter 9 summarizes the thesis achievements.

Chapter 2

Experimental techniques

The first section of this chapter describes the standard protocol of preparation of component materials of organic memristive device and its fabrication. The remaining sections review basics of experimental techniques, employed in the present research.

2.1 Organic memristive device fabrication

The standard technology to fabricate organic memristive device is developed to maximize its performance. For this several important aspects must be provided. The main property of the element is the thickness of conducting channel made of PANI. As OMD operation is controlled by lithium diffusion into active zone, PANI film have to be thin enough to provide lithium penetration into PANI. But on the other hand it have to be thick enough to provide good electronic conductivity of the channel. Polyelectrolyte in its turn has to provide optimal ionic conductivity. The concentration of ionic species in PEO has to be sufficient to influence noticeably the PANI conductivity, on the other hand, high concentration of ionic species is unacceptable, because it can cause faster polyelectrolyte degradation (in case of high HCl concentration) or salt aggregation. But most importantly, the high ionic conductivity does not provide the necessary difference (3-4 orders of magnitude) between the high- and low-resistive states (called as ON and OFF states) of the OMD.

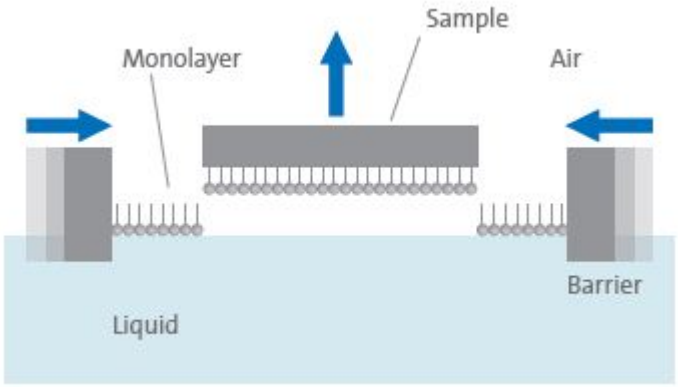

Figure 2.1. Schematic representation of Langmuir-Schaefer method used for PANI deposition

2.1.1 Materials

The fabrication of the organic memristive device conditionally can be divided into several steps: conducting channel production; polyelectrolyte preparation; the device assembly.

At the first step PANI solution was prepared. Polyaniline powder in emeraldine base form purchased from Sigma Aldrich was dissolved in N-Methyl-2-Pyrrolidone (NMP) organic solvent in 0.5 mg/ml concentration. PANI is purely soluble even in NMP, thus obtained solution was accurately filtered. Next, additional NMP containing 10% toluene organic solvent was added to filtered solution to obtain required PANI concentration of 0.1 mg/ml.

In the next step, the PANI film was formed. Langmuir-Schaefer method was employed for successive monolayer deposition. This method allows us to create films with a resolution of a single monolayer, thus the film thickness requirement, mentioned above, can be easily satisfied.

The main idea of the Langmuir-Schaefer method is the formation of a molecular monolayer of amphiphilic substance on water surface and its subsequent transfer to a solid substrate by horizontal lift (Fig.2.1). On the aqueous subphase amphiphilic molecules arrange on the air-water interface. In order to obtain a condensed monomolecular film the surface layer is compressed by special barriers. Consecutive transfer of the monolayer onto substrate is performed until desired number of layers is deposited.

Deposition of PANI EB films was made using KSV 5000 LB trough, filled by deionized Milli-Q water. The prepared PANI solution (300-450 μl) was spread on water surface and then compressed with 1 cm/s rate up to surface pressure reached 10 mN/m value. The formed monolayer was divided into small pieces using special grid. This is necessary to prevent the spread of PANI into parts of the surface where the monolayer has been already transferred onto substrate. PANI film containing 50 monolayers was deposited on a glass substrate of size 15×8 mm containing sputtered chrome electrodes (source and drain). To obtain conducting channel the film was proton doped by dipping the film into 1N hydrochloric acid for 2 minutes.

At the second step the polyelectrolyte is prepared. Lithium perchlorate trihydrate $LiClO_4 \times 3H_2O$ (Sigma Aldrich) was dissolved in Milli-Q water in 0.1 M concentration. PEO powder (Sigma Aldrich, molecular weight M_w=8×106) in 20 mg/ml concentration was dissolved in the salt solution. The prepared polyelectrolyte solutions were left overnight in closed container to let PEO swell to form homogeneous solution. Before use of about 2 μl of concentrated HCl acid was added to every 3 ml of polyelectrolyte solution.

Last step is the device assembly. The thin 1-2 mm stripe of the polyelectrolyte was inserted in the middle of PANI channel between two electrodes to form active zone of the device. Silver wire serving as a gate electrode was attached to the polyelectrolyte stripe. It is important to make sure of no mechanical contact of PANI and silver wire to avoid short circuit. Additional layer of the polyelectrolyte was added in order to totally wrap the wire. The assembled device was left to let the polyelectrolyte dry. Due to concentration gradient lithium ions can penetrate into PANI layer as the polyelectrolyte is casted on PANI, increasing conducting channel resistivity. Therefore before characterization the whole structure was additionally doped in HCl vapours to recover the active zone.

2.1.2 Characterization

In the standard operation regime source electrode is grounded, gate electrode is connected to source electrode through ammeter to measure ionic current flowing from active zone to gate. Voltage is applied to drain.

For characterization of OMD two currents are measured – ionic current in gate

electrode circuit and total current through PANI channel flowing between source and drain. Total current is the sum of electronic and ionic currents. However, the final state of OMD is evaluated in terms of electronic current – difference between measured total and ionic currents.

Typical characterization to evaluate OMD performance is current-voltage measurements. The response speed of the device is usually evaluated measuring kinetics of the device – current evolution at constant voltages.

2.2 Basics of Pulsed Gradient Field NMR

2.2.1 Introduction to NMR

Nuclear magnetic resonance (NMR) spectroscopy is based on the resonant interaction of atomic nuclei having non-zero spins placed in a constant magnetic field with electromagnetic radiation.

According to quantum mechanics, energy of a nucleus of spin I placed in a constant magnetic field splits into $2I+1$ energetic levels. Dipole moment selection rule allows transitions between neighboring energy states corresponding to energy difference equal to $\Delta E = \gamma\hbar H_0$, where H_0 is a constant magnetic field strength, γ is a gyromagnetic ratio – a constant value defined by a specific atom. Transition between these states is accompanied by absorption or emission of electromagnetic energy of frequency $\nu_0 = \frac{\Delta E}{h} = \frac{\gamma}{2\pi}H_0$.

In pulsed field NMR method the resonant transitions between these states caused by excitation of nuclei is performed by short radio frequency signal ($\mathbf{H}_1$), oriented perpendicularly to constant magnetic field ($\mathbf{H}_0$). According to statistical mechanics at thermodynamic equilibrium the population of nuclei energy levels is described by the Boltzmann distribution $n_i \propto \exp\left(-\frac{E_i}{k_B T}\right)$, where n_i is a number of particles in a state with energy E_i, k_B is a Boltzmann constant and T is a temperature. Since Boltzmann formula provides population decreasing with energy increase, meaning that lower energy level has slightly more population, than a higher one, nuclear magnetic moments, interacting with the constant magnetic field, creates macroscopic magnetization, representing sum of magnetic moments of individual nuclei, precessing around $\mathbf{H}_0$ with a frequency equal to $\omega_0 = \gamma H_0$.

Macroscopic magnetization $\mathbf{M}$ is colinear to $\mathbf{H}_0$.

When radio frequency (RF) pulse perpendicular to $\mathbf{H}_0$ with $\nu_0 = \omega_0/2\pi$ resonant frequency is applied to a sample, a macroscopic magnetization vector starts to deviate from the constant magnetic field direction. Properly chosen duration of RF pulse allows to turn a magnetization vector $\mathbf{M}$ to any certain angle. Thus, RF pulses, turning $\mathbf{M}$ to 90° or 180° are called $\pi/2$- and π-pulse correspondingly.

As $\pi/2$ RF pulse is applied to a sample, magnetization vector $\mathbf{M}$ becomes perpendicular to $\mathbf{H}_0$. A signal having initial amplitude $A(0)$ proportional to $\mathbf{M}$ is registered. This signal, called free induction decay (FID), is a decreasing function of time since $\mathbf{M}$ vector tends to relax to its initial state. Thus, a relaxation of the transverse component (relatively to $\mathbf{H}_0$) of macroscopic magnetization vector $\mathbf{M}_\perp$ appears due to irreversible phase coherence lose of spins precession during energy transfer from spin to spin. This process is characterized by time T_2 and it is called spin-spin relaxation. A relaxation of the longitudinal component $\mathbf{M}_\parallel$ to its initial state arises from interaction between exited spins and its environment. This process is called spin-lattice relaxation and it is characterized by time T_1.

Besides spin-spin and spin-lattice relaxation, nonuniformity of the constant magnetic field results in even faster signal decay. When the magnetic field $\mathbf{H}_0$ is nonuniform along a sample, nuclear spins distributed in a volume are exposed to different field, therefore the spins precess with different frequency. This leads to faster loss of phase coherence between individual magnetic moments, resulting in additional decrease of $\mathbf{M}_\perp$ component.

However, if in some time τ after the first $\pi/2$-pulse to apply π-pulse to a sample, at 2τ magnetic moments of resonant nuclei become coherent again and at this time the signal called echo is observed. The sequence of $\pi/2 - \tau - \pi - \tau$-echo is widely used to measure relaxation times to exclude the affection of nonuniformity of field $\mathbf{H}_0$. This sequence is called Hahn sequence. The action of the π-pulse causes rotation of the relative (to each other) movement of the magnetic moments of nuclei to 180°. Thus, while in $0 - \tau$ time interval (after $\pi/2$ RF pulse and before π-pulse) nuclear magnetic moments scatter by a phase, after π RF pulse they start to to stack till time $t = 2\tau$. This is strongly fullfilled only in the case when precession frequencies of every individual magnetic moment are constant in $0 - 2\tau$ time interval. This means nuclei have not to change their spatial position,

since spatial displacement of a nucleus in nonuniform magnetic field would lead to change of its precession frequency, and, therefore, at $t = 2\tau$ a phase of the nucleus would uncompensated relatively to other nuclei having $\Phi = 0$ phase. As a result, echo signal amplitude will be decreased more as more nuclei experience a translational displacement.

Thus, for conventional NMR technique an external magnetic field has to be uniform as more as possible. But there are a method when nonuniformity of magnetic field is beneficial [45]. It allows to collect the information on translational displacements of molecules by registration of echo signal obtained as a result of certain RF-sequences in a presence of external gradient magnetic fields.

2.2.2 Concept of Self-Diffusion phenomenon

Self-Diffusion is a process of spatial displacement of a molecule at thermodynamic equilibrium. This process appears due to chaotic thermal motion in a system. Trajectories of these translations are defined by interaction with huge number of neighbor particles and has random character.

Mathematically, these movements are described by propagator (Green function) $P(\mathbf{r} - \mathbf{r}_0, t)$. It has the meaning of density of conditional probability to find a molecule (with respect to center of mass) in $\mathbf{r}$ at time t, if initially the molecule is in $\mathbf{r}_0$. For times $t \gg \tau_{\max}$, where $\tau_{\max}$ is the biggest correlation time related to spatial degrees of freedom, propagator has a very simple form, defined by one parameter D_s:

$$P(\mathbf{r} - \mathbf{r}_0, t) = \frac{1}{(4\pi D_s t)^{3/2}} \exp\left(-\frac{|\mathbf{r} - \mathbf{r}_0|^2}{4D_s t}\right) \tag{2.1}$$

Regime of species movement, when $t \gg \tau_{\max}$ called diffusion regime, parameter D_s is a self-diffusion coefficient of a species. Using propagator 2.1 it is possible to calculate mean displacement of molecules in interval t_d (diffusion time):

$$< |\mathbf{r} - \mathbf{r}_0|^2 >= 6D_s t_d \tag{2.2}$$

This ratio is called Einstein equation.

Generally, even if the certain form of $P(\mathbf{r} - \mathbf{r}_0, t)$ is unknown, for effective

diffusion it is possible to write:

$$D_{eff}(t_d) \propto t_d^{2/d_w-1}, \tag{2.3}$$

where d_w is the walk dimension. For normal diffusion $2/d_w = 1$, while for anomalous diffusion $2/d_w \leq 1$

It is necessary to notice, that the concept of self-diffusion is different from mutual diffusion. Mutual diffusion is a process of movement of molecules from a region of high concentration to a region of low concentration at constant pressure. In other words, the process appears in a system which is thermodynamically not equilibrated due to presence the concentration gradient. The equilibrium is achieved due to mutual diffusion. In contrast, self-diffusion appears in a thermodynamically equilibrated system. The main reason of this process is thermal motion of molecules.

2.2.3 Pulsed Gradient Field NMR diffusometry

A molecule, placed in a constant in time gradient field $g_{0x} = \frac{\partial H_0}{\partial x}$ moves to a distance with x-projection equal to $x(t)$. In time t it will be exposed to magnetic field $H_0 = H_0(t) + g_{0x}x(t)$. In addition, precession frequency of nuclear spins of this molecule will change according to $\Delta\omega_0 = \gamma g_{0x}x(t)$. At time $t = 2\tau$ relative difference in their phases for Hahn sequence could be presented as:

$$\Phi(2\tau) = \gamma g_{0x}\Big[\int_0^{\tau} x(t)dt - \int_{\tau}^{2\tau} x(t)dt\Big] \tag{2.4}$$

Generally, an amplitude of spin echo signal $A(2\tau, g)$ obtained at constant in time gradient field g_{0x} could be represented by a distribution function $P(\Phi)$ of nuclear moments by corresponding phases Φ:

$$A(2\tau, g) = A(2\tau, 0)\int_{-\infty}^{\infty} P(\Phi)\cos\Phi d\Phi, \tag{2.5}$$

where $A(2\tau, 0)$ is an signal amplitude in a constant magnetic field H_0 (at $g = 0$). As it seen from E q. 2.5 the function $P(\Phi)$ has to be uniquely connected with distribution function $P(x)$ of nuclear moments by displacements x. Thus, for

Gauss distribution $P(x)$ of diffusion displacements x:

$$P(x) = (2\pi < x^2 >)^{-1/2} \exp(-x^2/2 < x^2 >), \tag{2.6}$$

where $< x^2 >$ is an average of square displacement of nuclear spins, associated with self-diffusion coefficient D_s via Einstein relation:

$$< x^2 >= 2D_s t, \tag{2.7}$$

we obtain:

$$P(\Phi) = (2\pi < \Phi^2 >^{-1/2} \exp(-\Phi^2/2 < \Phi^2 >) \tag{2.8}$$

Here $< \Phi^2 >$ is an average of square phase of an spin ensemble. Substituting Eq. 2.8 into Eq. 2.5 we obtain:

$$A(2\tau, g) = A(2\tau, 0) \exp(- < \Phi^2 > /2) \tag{2.9}$$

The value of $< \Phi^2 >$ at time 2τ could be calculated from:

$$< \Phi^2 >= \gamma^2 g_{0x}^2 \Big\langle \Big[\int_0^{\tau} x(t)dt - \int_{\tau}^{2\tau} x(t)dt \Big]^2 \Big\rangle \tag{2.10}$$

using Eq. 2.7.

Then the final expression of an echo signal amplitude for the two-pulse Hahn sequence at constant in time external magnetic field g_{0k} could be written as:

$$A(2\tau, g) = A(2\tau, 0) \exp(-2/3\gamma^2 g_0^2 \tau^3 D_s) \tag{2.11}$$

Since for an isotropic sample the gradient direction is unimportant, x index for g was skipped. The factor $A(2\tau, 0)$ describes an echo signal decrease due to spin-spin relaxation. For the most simple cases this factor could be obtained as:

$$A(2\tau, 0) = A(0) \exp(-2\tau/T_2), \tag{2.12}$$

where $A(0)$ is an NMR signal amplitude registered immediately after $\pi/2$ RF pulse, and T_2 is the spin-spin relaxation time.

Summarizing, an echo signal amplitude depends on nuclear relaxation processes

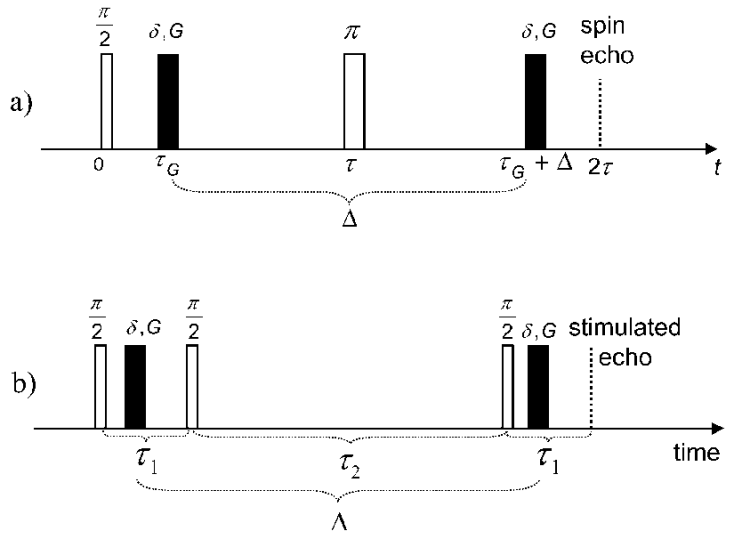

Figure 2.2. Radio frequency pulse sequences for the Hahn spin echo (a) and the stimulated spin echo (b) combined with magnetic field gradient pulses (black).

as well as translational mobility of molecules.

It could be noticed, that at fixed γ^2 and D_s the decrease of an echo amplitude due to diffusion becomes larger with increase of the value of $g_0^2\tau^3$. In other words, the more is $g_0^2\tau^3$ the less D_s value can be measured. The τ value is restricted by the speed of nuclear relaxation and has to be less or an order of T_2. Otherwise the echo signal amplitude would be too small to register it. Then, the value of the gradient field has not to be too large, because otherwise the resonance condition for a whole volume of a sample is violated. Obviously, the observation of the resonance condition is necessary only at excitation of a sample by RF pulses and a signal registration. Therefore, for other time intervals gradient magnetic field value can have values that are sufficiently large.

The first NMR method with pulsed gradient magnetic field (PGF NMR) was suggested by Stejskal and Tanner in 1965 [46]. In this method gradient magnetic field is included in Hahn sequence of RF-pulses (Fig.2.2a). In this method, gradient field is switched on as rectangular pulses. An expression for a spin echo signal amplitude can be obtained in the same way as for a constant in time magnetic gradient. The Eq. 2.4 would be replaced by:

$$\Phi = \gamma\Big[\int_0^{\tau} g(t)x(t)dt - \int_{\tau}^{2\tau} g(t)x(t)dt\Big], \tag{2.13}$$

adding to gradient field dependence on time. As a result for the sequence shown in Fig.2.2a, where $g(t)$ is represented by two components: constant gradient g_0 and two rectangular pulses of amplitude g and duration of δ, we obtain:

$$A(2\tau, g) = A(2\tau, 0)\exp\Big[\gamma^2 D_s[2/3\tau^3 g_0^2 - \delta \times$$
$$\times[t_1^2 - t_2^2 + \delta(t_1 + t_2) + 2/3\delta^2 - 2\tau^2]gg_0 + \delta^2(\Delta - 1/3\delta)g^2]\Big], \tag{2.14}$$

where Δ is a time interval between two gradient pulses, t_1 is a time between $\pi/2$ and the first gradient pulses, while t_2 corresponds to an interval between π and the second gradient pulses.

If g_0 value is too small in comparison to g, all terms, besides the last, in Eg. 2.14 could be neglected:

$$A(2\tau, g) = A(2\tau, 0)\exp(-\gamma^2 g^2 \delta^2 \Delta D_s). \tag{2.15}$$

Therefore, besides possibility of sufficiently increase a value of g in pulsed gradient field method, the time when diffusion is observed is clearly fixed. The factor $A(2\tau, 0)$ has the same meaning as in the Eq. 2.11, it describes a dependence of an echo amplitude on parameters of nuclear relaxation.

In addition to the described two-pulse Hahn method, there is a three-pulse technique of stimulated echo [47]. In this method, an amplitude of a stimulated echo signal $A(2\tau, \tau_1, g)$ is the same as Eq. 2.15, if $g_0 \ll g$. The factor $A(2\tau, 0)$ is replaced by $A(2\tau, \tau_1, 0)$, which in the case of simple relaxation is given by:

$$A(2\tau, \tau_1, 0) = \frac{A(0)}{2}\exp\Big(-\frac{2\tau}{T_2} - \frac{\tau_1}{T_1}\Big), \tag{2.16}$$

where T_1 is the time of spin-lattice relaxation. According to numerous studies on nuclear relaxation is is known that for polymeric melts and solutions $T_1 \gg T_2$.

If the condition $g_0 \ll g$ is not fulfilled, the signal amplitude is represented as:

$$A(2\tau, g) = A(2\tau, 0)\exp(-\gamma^2 g^2 \delta^2(\Delta - 1/3\delta)D_s), \tag{2.17}$$

where where $\Delta - 1/3\delta = t_d =$ is diffusion time.

An important advantage of the stimulated echo method is found in the possibil-

ity of significant increase of diffusion time t_d in comparison to two-pulse technique, where δ and t_d is restricted by the value of T_2. Therefore, in three-pulse technique of stimulated echo the measuring range of self-diffusion coefficients is expanded.

A direct determination of self-diffusion coefficient D_s in an experiment is performed via calculating the slope of the envelope of a stimulated echo signal amplitude ratio $A(2\tau, \tau_1, g)/A(2\tau, \tau_1, 0)$ at switched on and switched off gradient magnetic field when one of the parameters g, δ or t_d is varying. Corresponding envelopes could be denoted as $A(g^2)$, $A(\delta^2)$ and $A(t_d)$. And they are called diffusion decay.

From the practical point of view the most convenient way is to register $A(g^2)$ at fixed δ and t_d. This is also related to the fact that in this case time intervals between RF pulses are also fixed. Then throughout an experiment the contribution of relaxation attenuation of an echo signal $A(2\tau, \tau_1, 0)$ will be constant, that is extremely important in cases of complex polymeric systems, when Eq. 2.12 and Eq. 2.16 could not be used to describe relaxation process.

2.3 Basics of X-ray Powder Diffraction

The method of X-ray diffraction consist of acquisition and analysis of functional dependence of diffracted radiation intensity I on diffraction angle θ. The spatial distribution of diffraction picture arises from interaction of X-ray radiation with electrons of matter.

The model describing X-ray diffraction in crystals is well-known as the Bragg's law or selective reflection. According to this law diffracted X-ray beam could be considered as a result of reflection of incident beam from a certain set of parallel crystallographic plains. The rays, reflected according to reflection law will interfere constructively or destructively between each other depending on difference in distance traveled by beams (PD).

The set of parallel planes (P_0P_0, P_1P_1, P_2P_2 and so on) with interplane distance d is presented in Fig.2.3. The incident angle of the beam is θ. The PD (for example, the ray I and II) is $\Delta l = AB - AC$, and AB is given by $d/\sin\theta$, $AC = AB\cos 2\theta$, thus $\Delta l = 2d\sin\theta$. According to interference theory, the reflected rays will experience constructive interference, causing amplification of the radiation intensity, if the PD Δl is multiple of the incident wave length:

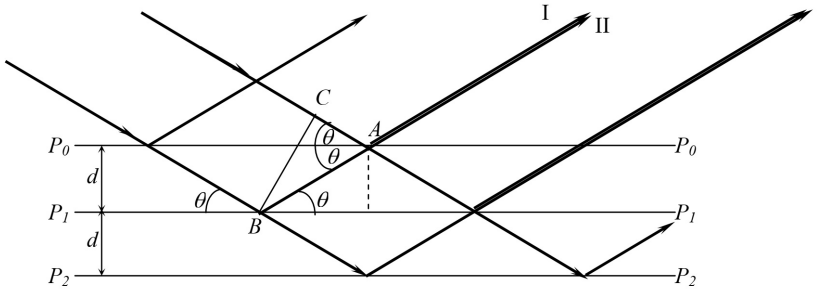

Figure 2.3. Schematic representation of X-ray selective reflection

$$2d_{(hkl)} \sin\theta_i = n\lambda, \tag{2.18}$$

where (hkl) refers to the Miller indices, which describes a family of crystallographic planes. Therefore, obtained diffraction pattern is a set of peaks of different intensity depending on diffraction (or reflection) angle θ. Every peak corresponds to reflection of a beam from certain family of planes in lattice.

The obtained diffraction pattern $I(\theta)$ is analyzed in the way to associate every obtained diffraction peak position (expressed in 2θ) with an interplane distance d, using Eq. 2.18.

Moreover, there is relation between interplane distance $d_{(hkl)}$, unit cell parameters, Muller indices and a type of crystallographic system. In other words, $d_{(hkl)}$ is a function of the size and shape of an unit cell:

$$d^{*2}_{hkl} = h^2a^{*2} + k^2b^{*2} + l^2c^{*2} + 2hka^*b^*\cos\gamma^* + 2hla^*c^*\cos\beta^* + 2klb^*c^*\cos\alpha^*, \tag{2.19}$$

where a^*,b^*, c^*,α^*,β^*,γ^* are parameters of a reciprocal lattice, $d^{*2}_{hkl} = 1/d^2$, $a^* = bc\sin\alpha/abc$, $\cos\alpha^* = (\cos\beta\cos\gamma - \cos\alpha)/(\sin\beta\sin\gamma)$.

In addition, peaks are characterized by their intensity. These intensities are defined by multiple factors, for example:

$$I_{hkl} = I_0 p_{hkl} A(LPG) T(hkl) |F_{hkl}|^2, \tag{2.20}$$

where I_0 is an incident radiation intensity, (hkl) is Muller indices of the given

reflecting plane, p_{hkl} is a repeatability factor, LPG is a factor, combining polarization, geometrical and Lorentz factors, $T(hkl)$ is a texture factor, $|F_{hkl}|^2$ is a structure factor, A is a factor reflecting absorption of X-ray radiation. The repeatability factor takes into account the coincidence of the diffraction angles of reflexes with different indices. LPG factor combines factors, defined by experimental conditions. The texture factor considers predominant orientation of crystallites in a sample. The structure factor quantifies the amplitude of light scattered by a sample. The patterns of atoms in the unit cell scatters strongly in some directions and weakly in others due to interference of the wavelets scattered by the atoms. Structure factor represents square of structural amplitude (F_{hkl}). In its turn, amplitude of scattered light by a sample is determined by the arrangement of atoms in the diffracting planes. F_{hkl} sums the result of scattering from all of the atoms in the unit cell to form a diffraction peak from the (hkl) planes of atoms:

$$F_{hkl} = \sum_{j=1}^{m} N_j f_j \exp\Big[2\pi i(hx_j + ky_j + lz_j)\Big] \tag{2.21}$$

The amplitude of scattered light is determined by where the atoms are on the atomic planes (this is expressed by the fractional coordinates x_j y_j z_j) and what atoms are on the atomic planes. Thus the scattering factor f_j quantifies the relative efficiency of scattering at any angle by the group of electrons in each atom. N_j is the fraction of every equivalent position that is occupied by atom j.

2.3.1 Rietveld refinement

In practise, a typical way to solve a structure using X-ray diffraction after data are collected and primary information mentioned above is obtained, is to find a trial solution and then to refine it.

A widely used technique, called Rietveld refinement [48], is applied in order to refine a theoretical diffraction pattern to match it with measured entire powder diffraction profile. In other words, the method implies calculation a model diffraction pattern based on crystal structure and parametrized profile functions, and adjust structural and profile shape parameters to get the best agreement. Practically, the parameters, describing different contribution to the diffraction pattern

are matched to minimize a function, represented as a difference between calculated y^{calc} and observed y^{obs} diffraction data:

$$M = \sum_i W_i \Big[y_i^{obs} - \frac{1}{c} y_i^{calc} \Big]^2, \tag{2.22}$$

where W_i is a statistical weight and c is an overall scale factor such that $y^{calc} = cy^{obs}$.

Mentioned above parameters are fitted using least squares approach.

Usually, the shape of powder diffraction pattern depends on characteristics of the beam, experimental equipment and a sample size and shape. For most cases the shape of individual reflex could be approximated by Gauss function. Thus in Rietveld method peak shape function is given by:

$$y_i = I_k \exp \Big[-\frac{4 \ln 2}{H_k^2} (2\theta_i - 2\theta_k)^2 \Big], \tag{2.23}$$

where H_k is the full width at half peak height, $2\theta_k$ is the centre of the reflex, I_k is the calculated intensity of the reflex (determined from the structure factor, the Lorentz factor, and multiplicity of the reflection).

To avoid vertical asymmetry appearing at low diffraction angles due to the vertical divergence of the beam, Rietveld introduced a semi-empirical correction factor:

$$A_s = 1 - \Big[\frac{sP(2\theta_i - 2\theta_k)^2}{\tan \theta_k} \Big], \tag{2.24}$$

where P is the asymmetry factor, s=+1, 0, -1 depending on the difference $2\theta_i - 2\theta_k$ being positive, zero or negative correspondingly.

When at given $2\theta_i$ position more than one peak contribute to the diffraction pattern, the intensities of every individual diffraction peak are simply summing.

At higher diffraction angles the peaks were found to be more broaden. In order to include this fact to the diffraction profile calculation, angular dependency on the full width at half peak height is imposed:

$$H_k^2 = U \tan {\theta_k}^2 + V \tan \theta_k + W \tag{2.25}$$

In this relation, U, V and W are referred to the halfwidth parameters which

will be refined.

In powder or polycrystalline samples diffraction peak intensities could vary from predicted to completely random distribution. Last cases in Rietvield method controlled by intensity correction factor:

$$I_{corr} = I_{obs} \exp -G\alpha^2, \tag{2.26}$$

where I_{obs} is the intensity expected for a random sample, G is the parameter referring to preferred orientation and α is the acute angle between the scattering and the normal vector of the crystallites.

2.4 Basics of Impedance Spectroscopy

A large number of interrelated processes occur in electrochemical systems. For example, transport of charged particles, diffusion of neutral particles, sorption, electrochemical reactions. It is not always possible to set up experiments in such a way to isolate and study each elmentary process separately; more often it is necessary to deal with minimal groups of related processes. Impedance spectroscopy significantly expands the electrical approach to the study of electrochemical systems [49].

Generally, the method is based on the analysis of the response of an electrochemical cell on small perturbation by alternating voltage or current. Impedance by its definition is a complex quantity, represented as a ratio between alternating voltage and current. As a result, impedance $Z = Re(Z) + jIm(Z)$ has two components – a real part, that does not depend on frequency (resistance), and active component (imaginary), that depends on frequency (capacitance and inductance). Therefore, analyzing the impedance spectra, it is possible to associate each elementary process occurring in an electrochemical system by not only resistance, but also by a certain capacity (and inductance in some cases), and, therefore, some characteristic relaxation frequency. The specific form of impedance dependence on frequency contains information about the elementary electrochemical processes. Impedance spectra are usially measured by potentiostatic or galvanostatic methods, depending on measuring response - voltage or current respectively.

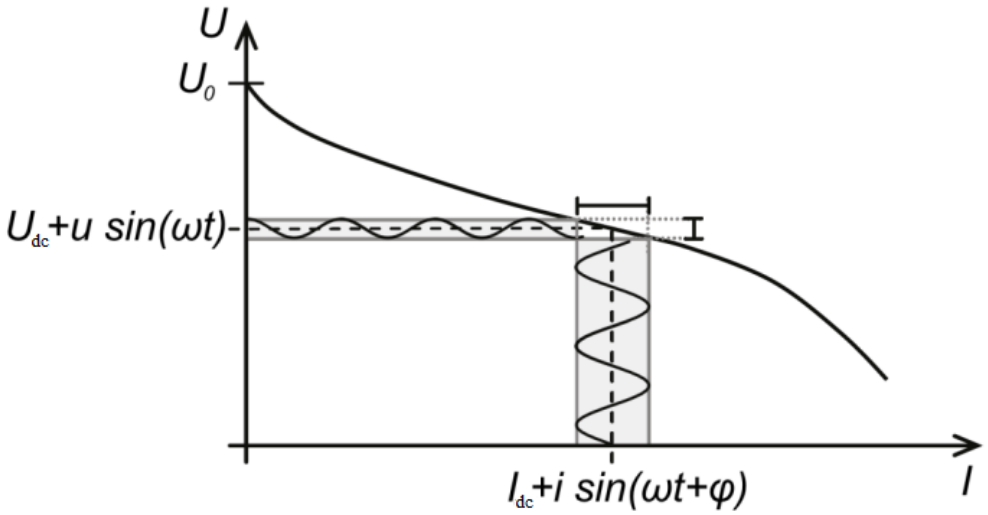

Figure 2.4. An example of impedance measurement process

An example of the cell response acquisition is shown in Fig.2.4, where alternating voltage applied to the system is summed with an alternating signal, and an amplitude of an alternating current and a phase shift is measured.

Analyzing the behavior of different parts of the spectrum moving along a current-voltage curve helps to identify corresponding electrochemical processes. General approach to analyze measured data includes the approximation of the experimental spectra by models, based on equivalent circuits corresponding to certain electrochemical system.

Further, the main elements used to construct equivalent circuits will be considered.

2.4.1 RC-contour

The simplest model of an ideal electrochemical process (besides resistor) is RC-contour, composed of connected in parallel resistor and capacitor (see Fig.2.4.1a). Typical representation of impedance spectra is Nyquist plot showing dependence of imaginary component of impedance on its real one (-Im(Z)(Re(Z))). RC-contour Nyquist plot is shown in Fig.2.4.1b.

The impedance of this contour is:

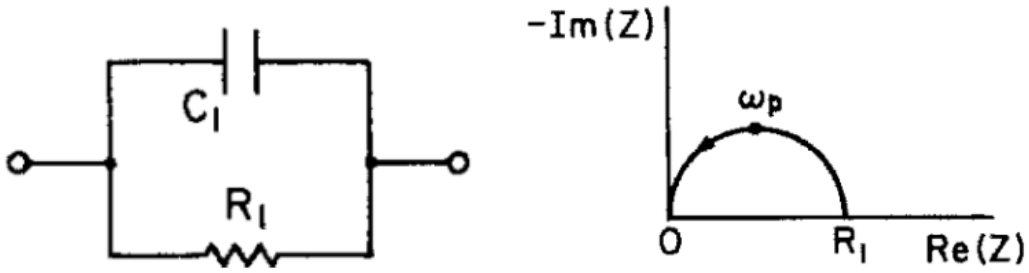

a b

Figure 2.5. RC-contour (a) and Nyquist plot of its impedance hodograph (b)

$$Z_{RC} = \frac{R}{1 + j\omega RC}. \tag{2.27}$$

In Nyquist coordinates, the hodograph has the form of a semicircle, crossing the origin. The center of this semicircle lies on the real axis, its diameter is equal to the resistance of the resistor, and the maximum value of the imaginary axis corresponds to the circular frequency $\omega = 1/RC$. Because of this reason the hodographs are usually plotted in equal axial scales.

2.4.2 RQ-contour

Initially, RQ-contour represents empirical generalization of the RC-contour. Usually, it describes semicircles of impedance spectra with shifted below real axis centers. In this contour constant phase element (CPE) replaces capacitor. The impedance of CPE is represented as:

$$Z_{CPE} = \frac{1}{Q(j\omega)^n}. \tag{2.28}$$

Generally, CPE is an element, behaving as resistor, inductance or capacitor depending on n value equal to 0, -1 or 1 respectively. The main property of this element is constant phase shift $\frac{\pi}{2}n$ between current and voltage.

Then, RQ-contour impedance is:

$$Z_{RQ} = \frac{R}{1 + (j\omega)^n RQ}. \tag{2.29}$$

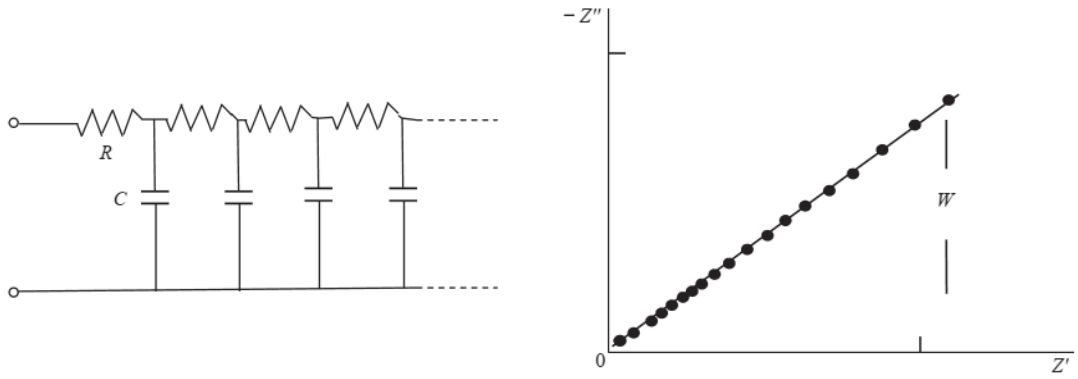

a b

Figure 2.6. Semi-infinite scheme reflecting Warburg element (a) and Nyquist plot of its impedance hodograph (b)

Despite the fact that the general meaning of the CPE is very wide, in electrochemical impedance spectroscopy (EIS) it is preferably used as an effective non-ideal capacitor.

2.4.3 Warburg element

The most common contour, describing diffusion of particles is Warburg element [50]. It models semi-infinite linear diffusion, that physically means unrestricted diffusion of particles to a large planar electrode surface. In terms of circuit elements, Warburg element represents semi-infinite scheme composed of resistors and capacitors (Fig.2.4.3a). Its matematical expression is:

$$Z_W = \frac{W}{\omega^{1/2}} - j\frac{W}{\omega^{1/2}}. \tag{2.30}$$

For this element the phase shift between current and voltage is constant and equal to $\pi/4$. In the Nyquist plot, Warburg element represents a line with a slope of 45 (Fig.2.4.3b).

Constant phase element can also model Warburg element, when its n parameter is equal to 0.5.

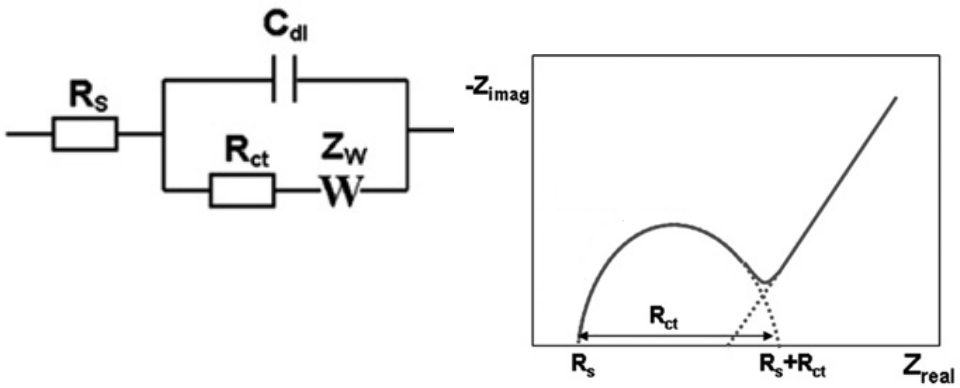

a b

Figure 2.7. Randless circuit (a) and Nyquist plot of its impedance hodograph (b)

2.4.4 Randles circuit

Randless circuit [51] is the most commonly used equivalent circuit in electrochemical impedance spectroscopy. It models semi-infinite diffusion-controlled faradaic reaction to a planar electrode.

The elements of this circuit, represented in equivalent circuit in Fig.2.4.4a, are interpreted as electrolyte bulk resistance (R_s), charge transfer resistance (R_{ct}), double layer capacitance (C_{dl}) and Warburg impedance ((Z_W)). Nyquist plot of the Randless circuit impedance hodograph is shown in Fig.2.4.4b.

Chapter 3

Theoretical methods

3.1 Molecular Dynamics

Molecular dynamics (MD) simulation is a technique allowing to compute the equilibrium and dynamic properties of a classical many-body system. Particles motion in a system obeys classical equation of motion, thus evolution of system could be obtained by integrating Newton's equations of motion for a set of interacting particles:

$$m_i \frac{d^2 \mathbf{r}_i}{dt} = \sum_{j \neq i} \mathbf{F}_{ij} \tag{3.1}$$

where m_i is a mass of a particle i at $\mathbf{r}_i$=(x_i, y_i, z_i) position, $\mathbf{F}_{ij}$ is interaction force between ith and jth particles.

A simulation starts from calculation a force, acting on every particle, given by

$$\mathbf{F}_{ij} = -\nabla_i U(|\mathbf{r}_i - \mathbf{r}_j|) \tag{3.2}$$

where U(| $\mathbf{r}_i$ - $\mathbf{r}_j$ |) is an interaction potential of particles in the system and ∇_i = $\left(\frac{\partial}{\partial x_i}, \frac{\partial}{\partial y_i}, \frac{\partial}{\partial z_i}\right)$. An interaction potential contains prior information, derived from experiments or precomputed by more accurate ab-initio methods. Usually, this information consists of parameters of parameterized interaction potential, including interaction terms of two, three and four particles:

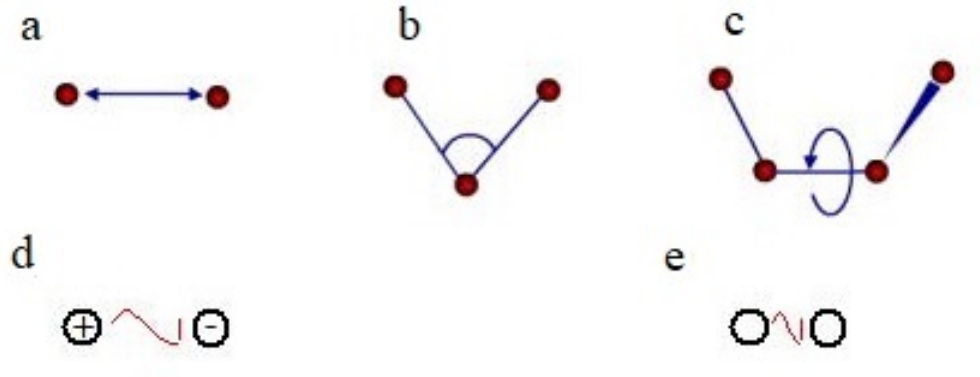

Figure 3.1. The typical interaction potential contains bond length (a), bond valence angle (b), bond dihedral angle (c), non-bonded electrostatic (d) and non-bonded van-der Waals interaction (e) contributions to the total energy of a system

$$V(\vec{r}) = \sum_{bonds} k_i^{bond}(r_i - r_0)^2 + \sum_{angles} k_i^{angle}(\theta_i - \theta_0)^2 + \\ + \sum_{dihedrals} k_i^{dihedrals}(1 + cos(n_i\phi_i + \delta_i) + \\ + \sum_i \sum_{i \neq j} 4\epsilon_{ij}\left((\frac{\sigma_{ij}}{r_{ij}})^{12} - (\frac{\sigma_{ij}}{r_{ij}})^6\right) + \sum_i \sum_{i \neq j} \frac{q_i q_j}{\epsilon r_{ij}} \tag{3.3}$$

In this equation the terms correspond to energy dependence on bond length, bond valence angle, bond dihedral angle, non-bonded electrostatic and non-bonded van-der Waals interactions correspondingly. Schematic representation of the origin of these interactions is presented in Fig. 3.1.

There are different algorithms to solve equation 3.13. One of them is the Verlet algorithm [52], allowing to integrate the Newton 3.13 equations of motion in NVE ensemble with constant parameters: total energy E, the number of particles N and the volume of the simulation box V.

The integration of the equation considers expansion of coordinate forward and backward in time performing Taylor expansion:

$$\mathbf{r}(t + \delta t) = \mathbf{r}(t) + \frac{1}{m}\mathbf{p}(t)\delta t + \frac{1}{2m}\mathbf{F}\delta t^2 + \frac{1}{3!}\dddot{\mathbf{r}}\delta t^3 + \mathcal{O}(\delta^4), \tag{3.4}$$

and similarly,

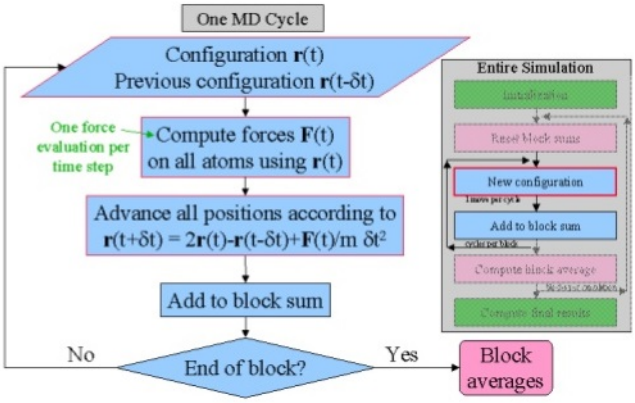

Figure 3.2. The flow chart of Verlet algorithm

$$\mathbf{r}(t-\delta t) = \mathbf{r}(t) - \frac{1}{m}\mathbf{p}(t)\delta t + \frac{1}{2m}\mathbf{F}\delta t^2 - \frac{1}{3!}\dddot{\mathbf{r}}\delta t^3 + \mathcal{O}(\delta^4). \tag{3.5}$$

Add the equations together gives:

$$\mathbf{r}(t+\delta t) + \mathbf{r}(t-\delta t) = 2\mathbf{r}(t) + \frac{1}{m}\mathbf{F}\delta t^2 + \mathcal{O}(\delta^4). \tag{3.6}$$

or

$$\mathbf{r}(t+\delta t) = 2\mathbf{r}(t) - \mathbf{r}(t-\delta t) + \frac{1}{m}\mathbf{F}\delta t^2 + \mathcal{O}(\delta^4). \tag{3.7}$$

The steps of evaluating a force acting on each particle and integrating Newton's equation of motion is repeated until we have calculated the time evolution of the system defined as a simulation time. The flow chart of the algorithm is presented in Fig. 3.2.

To obtain velocities (if necessary to compute some properties, as temperature of diffusion constant) finite difference is used:

$$\mathbf{v} = \frac{1}{2\delta t}\Big[\mathbf{r}(t+\delta t) - \mathbf{r}(t-\delta t)\Big] + \mathcal{O}(\delta^2) \tag{3.8}$$

In practise, an equivalent version of the Verlet algorithm, called velocity Verlet is used. Its steps are implemented as follow:

$$\mathbf{v}(t+\delta t/2) = \mathbf{v}(t) + \frac{\mathbf{F}(t)\delta t}{2m} \tag{3.9}$$

$$\mathbf{r}(t+\delta t) = \mathbf{r}(t) + \mathbf{v}(t+\delta t/2)\delta t \tag{3.10}$$

$$\mathbf{F}(t+\delta t) = \mathbf{F}(\mathbf{r}(t+\delta t)) \tag{3.11}$$

$$\mathbf{v}(t+\delta t = \mathbf{v}(t+\delta t/2) + \frac{\mathbf{F}(t+\delta t)\delta t}{2m} \tag{3.12}$$

From statistical point of view estimated averages in MD simulations come from time averages equivalent to ensemble averages due to ergodicity theorem. The method have an extension allowing to perform simulations at constant temperature (NVT) and constant pressure (NPT).

Nose-Hoover thermostat [53, 54, 55] employed in the present research is well-known as a most accurate and efficient deterministic algorithm. It provides a way to simulate a system which is (asymptotically, i.e. at large times) in the NVT ensemble. The idea begins from introduction a fictitious dynamical variable, whose physical meaning is a friction ζ. It slows down or accelerates particles until the temperature is equal to the target value (estimated by the kinetic energy). The equations of motions transform into:

$$m_i \frac{d^2\mathbf{r}_i}{dt} = \sum_{j\neq i} \mathbf{F}_{ij} - \zeta m_i \mathbf{v}_i \tag{3.13}$$

$$\frac{d\zeta(t)}{dt} = \frac{1}{Q}\Big[\sum_{i=1}^{N} m_i \frac{\mathbf{v}_i^2}{2} - \frac{3N+1}{2} k_B T\Big], \tag{3.14}$$

where Q defines the relaxation of the dynamics of the friction $\zeta(t)$, T is a target temperature.

Basically, discretisation can be implemented using small modifications on velocity Verlet algorithm. The first four steps are given by:

$$\mathbf{r}_i(t+\delta t) = \mathbf{r}_i(t) + \mathbf{v}_i(t)\delta t + \Big(\frac{\mathbf{F}_i(t)}{m_i} - \zeta(t)\mathbf{v}_i(t)\Big)\frac{\delta t^2}{2} \tag{3.15}$$

$$\mathbf{v}_i(t+\delta t/2) = \mathbf{v}_i(t) + \frac{\delta t}{2}\Big(\frac{\mathbf{F}_i(t)}{m_i} - \zeta(t)\mathbf{v}_i(t)\Big) \tag{3.16}$$

$$\mathbf{F}_i(t+\delta t) = \mathbf{F}_i(\mathbf{r}_i(t+\delta t)) \tag{3.17}$$

$$\zeta(t+\delta t/2) = \zeta(t) + \frac{\delta t}{2Q}\Big[\sum_{i=1}^{N} m_i \frac{\mathbf{v}_i^2(t)}{2} - \frac{3N+1}{2}k_B T\Big] \tag{3.18}$$

To follow the two-step parameters update in the velocity Verlet algorithm, $\zeta(t)$ is also first updated at time $t+\delta/2$. This, final steps are:

$$\zeta(t+\delta t) = \zeta(t+\delta t/2) + \frac{\delta t}{2Q}\Big[\sum_{i=1}^{N} m_i \frac{\mathbf{v}_i^2(t+\delta t/2)}{2} - \frac{3N+1}{2}k_B T\Big] \tag{3.19}$$

$$\mathbf{v}_i(t+\delta t) = \frac{\Big[\mathbf{v}_i(t+\delta t/2) + \frac{\delta t}{2}\frac{\mathbf{F}_i(t+\delta t)}{m_i}\Big]}{1+\frac{\delta t}{2}\zeta(t+\delta t)} \tag{3.20}$$

Similar equation of motions are formulated for constant pressure dynamics. The Nose-Hoover equations of motion are given by:

$$\dot{\mathbf{r}}_i = \mathbf{p}_i/m_i + \eta(\mathbf{r}_i - \mathbf{r}_0) \tag{3.21}$$

$$\dot{\mathbf{p}}_i = \mathbf{F}_i - (\zeta+\eta)\mathbf{p}_i \tag{3.22}$$

$$\dot{\zeta} = \frac{1}{\tau_T^2}(T_K(t)/T_S - 1) \tag{3.23}$$

$$\dot{\eta} = \frac{V}{Nk_B T_S}\tau_p^2(p(t) - p_{ext}) \tag{3.24}$$

$$\dot{V} = 3V\eta \tag{3.25}$$

In these equations, η represents a friction evolving in time to minimize the difference between the instantaneous pressure $p(t)$ and the pressure of an external reservoir (target pressure). There are two relaxation times – for thermostat τ_T and barostat τ_p.

The updating of variables are performed in the same way described for Nose-Hoover thermostat.

Chapter 4

Lithium self-diffusion in PEO

This chapter describes the results of $LiClO_4$ doped PEO studied by PGF NMR. This method allows to consider lithium motion on a very short time scales. Two problems were considered – the presence of motional restriction for lithium ions in PEO and temperature effect on lithium transport.

4.1 Experimental details

The standard polyelectrolyte solution was prepared as described in Section 2.1 of Chapter 2. In this study two different samples were examined – as prepared gel polyelectrolyte solution (referred as liquid) and dried polyelectrolyte. Dry sample was formed from the solution as an about 1 mm thick film casted onto a teflon substrate and left to dry for three days under fume hood. Free standing film was detached from the substrate and used for the measurements. The second sample was as prepared polyelectrolyte gel used without drying. For each NMR experiment the sample was placed in a 5 mm glass tube and closed with a plastic stopper to avoid contact with air.

Pulsed gradient field NMR experiments were performed using Bruker AVANCE 400 NMR spectrometer equipped with z-gradient probe head Diff50 (Bruker) with a gradient strength up to 300 G/cm. The 7Li (155.51 MHz) resonance signal was used for measurements. Standard pulse sequence of stimulated-echo was employed [46]. The $\pi/2$ radio frequency pulse duration was 10 μs. The duration of every of two gradient pulses δ from the sequence and time between them Δ was

changed according to $\delta^2\Delta$=const (0.37 - 3 ms for δ and 15 - 1000 ms for Δ) in the diffusion time dependence measurements. For every measurement gradient pulse was varied from 0 up to 300 G/cm. For temperature dependence studies δ and Δ were 1.2 ms and 90 ms correspondingly. Temperature was changed with a step of 15 K in the range . As the target temperature was reached, a sample was kept at this temperature to bring to equilibrium for 10 minutes before measurement.

4.2 Motional restriction probing

The probing self-diffusion coefficients (SDCs) on diffusion time dependence give the information on spatial restriction for lithium transport. This restriction can reflect, for instance, a porous structure of polyelectrolyte. Even in the simplest case of diffusion in reflecting sphere the signal attenuation represents more complicated shape of evidential diffraction minima, rather simple exponential decay [56, 57, 58].

The obtained weighted diffusion decays $A(g^2)/A(0)$ (where $A(0)$ is the signal amplitude after first $\pi/2$ pulse) are shown in Fig.5.4.2 for the liquid (Fig.5.4.2a) and dried (Fig.5.4.2b) samples. Different curves in the plots correspond to different sets of δ and Δ in stimulated echo sequence.

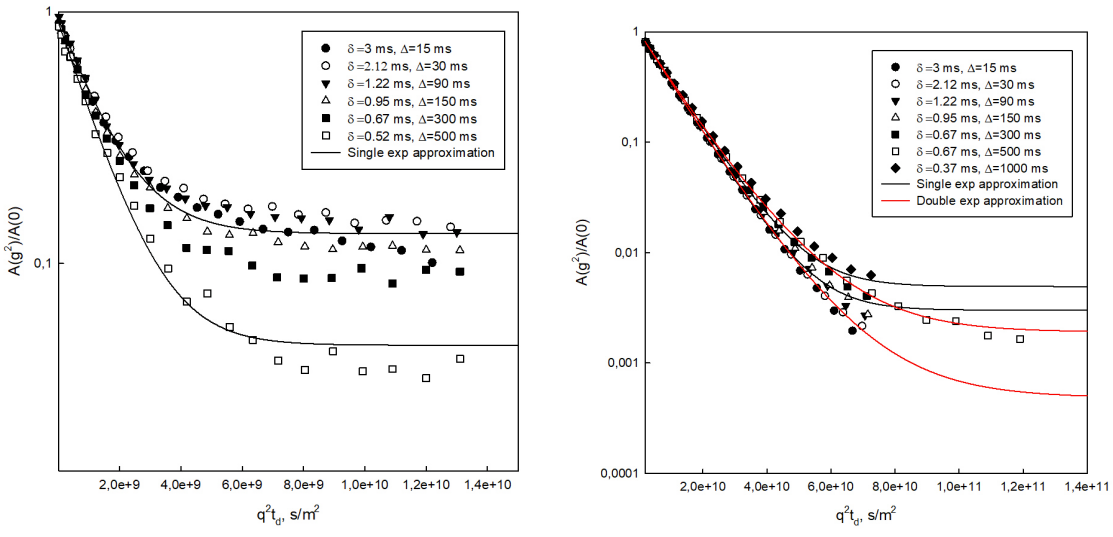

Figure 4.1. PGF NMR signal attenuation for liquid (a) and dry (b) samples for a set of different δ and Δ

First, we can see immediately that for the both samples the signals are not single-exponential. The shape of the signal for the liquid sample likely demonstrates diffraction-like minima for high gradient magnetic field values (high $q^2 t_d$). It complicates signal data analysis, thus we will treat data as exponential function, deriving in this case so-called apparent self-diffusion coefficients, regressing data onto Eq.2.17 as was described in Section 2. The derived mean values of SDC of lithium in liquid polyelectrolyte is D_{app} =8.49×10^{-10} m^2/s (Fig.4.2a). The dependence of SDC on Δ is extremely weak, thus, accordingly Eq.2.3 there is no motional restriction for lithium transport.

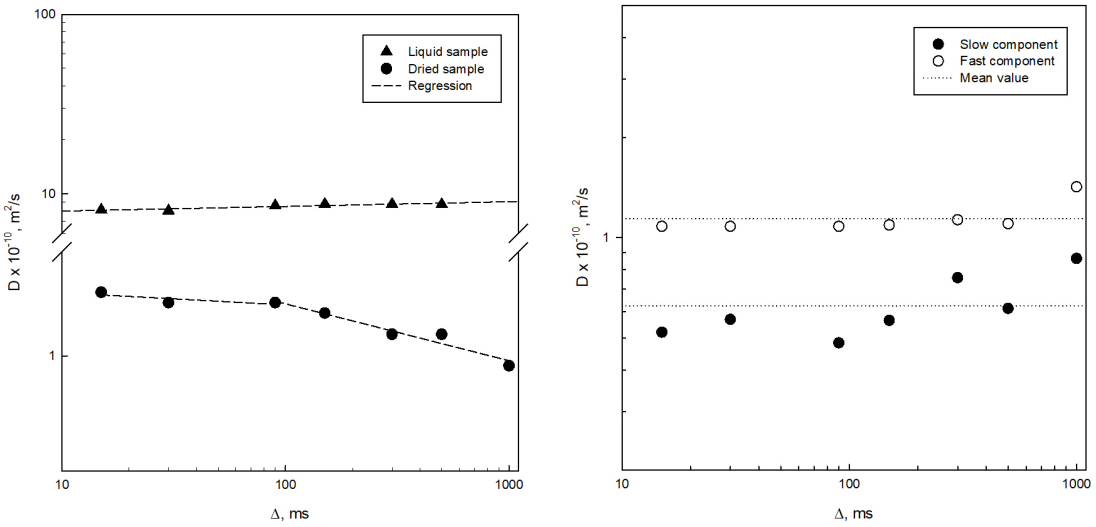

a b

Figure 4.2. Self-diffusion coefficients estimated for liquid (a) and dry (b) samples for a set of different δ and Δ

The data obtained for dried sample does not show diffraction-like behaviour, however, it is clearly seen that signals are bi-exponential. Such result can arise due to the "multiphase" set of resonant nuclei. The mentioned "phase" term is different from thermodynamic phase. In NMR "phase" combines a group of spins possessing the same relaxation times or diffusion coefficients. In this case signal attenuation is a sum of exponents in form Eq.2.17:

$$A(g)/A(0) = \sum_i^N p_i \exp(-\gamma^2 g^2 \delta^2 D_i(\Delta - \delta/3)) \tag{4.1}$$

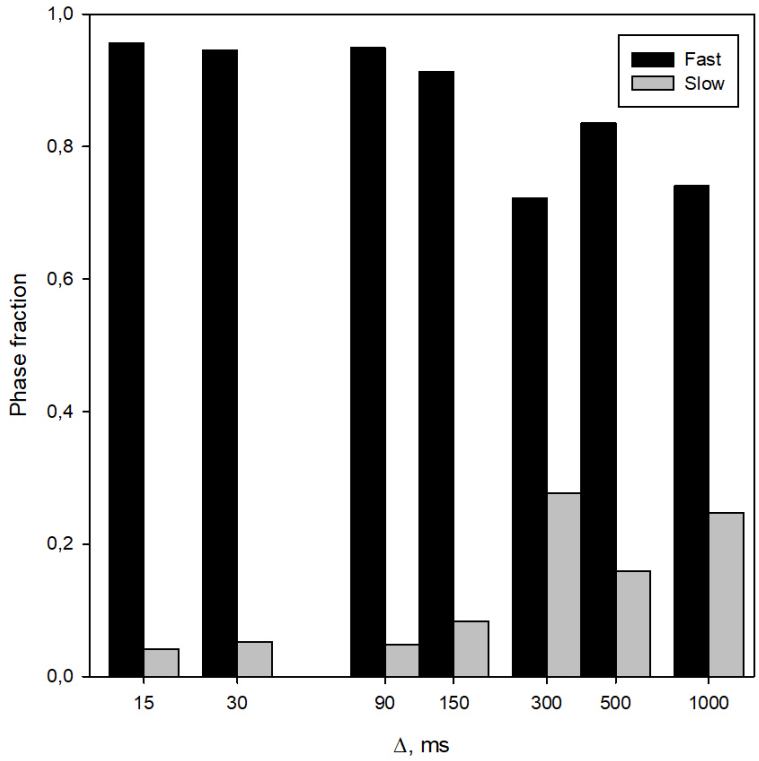

Figure 4.3. Phase fraction distribution

The factor p_i is a relative fraction of corresponding phase having self-diffusion coefficient D_i. The averaged over Δ values of SDC for lithium in dried sample derived from bi-exponential signals are $0.62{\times}10^{-10}$ and $1.14{\times}10^{-10}\,\mathrm{m}^2/\mathrm{s}$, which will be referred as slow and fast diffusion of phase components correspondingly (Fig.4.2). The difference in diffusion coefficients of slow and fast phases is an about two times. The relative phase fraction p_i distribution for every measurement is shown in Fig.4.3. Fast diffusing phase component dominates, while the observed Δ dependence on relative phase fractions is likely the result of the changing contribution of the various components to the signal. The nature of faster and slower lithium ions, probably, is related to the presence in the dried sample dissolved and aggregated salt.

The evidence of multiphase spin system in real samples is rather typical, than single-phase due to inhomogeneities. Thus usually a mean SDC over phases is considered, that can be estimated as:

$$D = \sum_{i}^{N} p_i D_i \tag{4.2}$$

The dependence of diffusion coefficients of lithium ions in dried sample averaged over slow and fast diffusing phases on Δ is shown in Fig.4.2a. Two different regimes of SDC function on diffusion time are observed. For short diffusion time regime this dependence of SDC on Δ is weak. Above a threshold diffusion time of $\Delta_{\text{th}} = 90\,\text{ms}$ a small decrease of diffusion coefficient occurs. The slope estimated according to Eq.2.3 as α=0.04 is very close to zero, thus lithium diffusion in dried sample is considered as normal diffusion similar to liquid sample. The mean apparent SDC over Δ for dried sample was estimated as $1.05{\times}10^{-10}\,\text{m}^2/\text{s}$ from the experimental data points before Δ_{th}.

4.3 Temperature effect on Lithium transport

Further we will discuss temperature effect on lithium motion in PEO. Obviously, increase of lithium diffusion rates is expected, since the driving force of self-diffusion is a thermal energy of a specie.

Experimental parameters, particularly, a pair of times δ and Δ for this part of investigation were chosen according to previous results. Namely, it is necessary to provide enough diffusion time, mostly defined by the separation between the gradient pulses Δ. However, as we see in the previous section, some insufficient deviations of SDC of lithium in dried sample from constant value after Δ_{th} is present, thus $\Delta = 90\,\text{ms}$ was used as optimal one for temperature effect measurements along with $\delta = 1.2\,\text{ms}$.

The resulted signals of liquid and dried samples in $293 - 353\,K$ temperature range are presented in Fig.4.4a and 4.4b correspondingly. Despite the actual shape, all the signals were treated as single-exponential, since even in the dried sample mean SDC is mostly defined by dominated phase (Eq.4.2, which showed higher diffusion coefficients, thus the minor phase will not give sufficient contribution to the mean diffusion rate).

The evaluated SDCs plotted versus reciprocal temperature are shown in Fig.4.5. The line corresponding to liquid sample is about one order of magnitude distinct

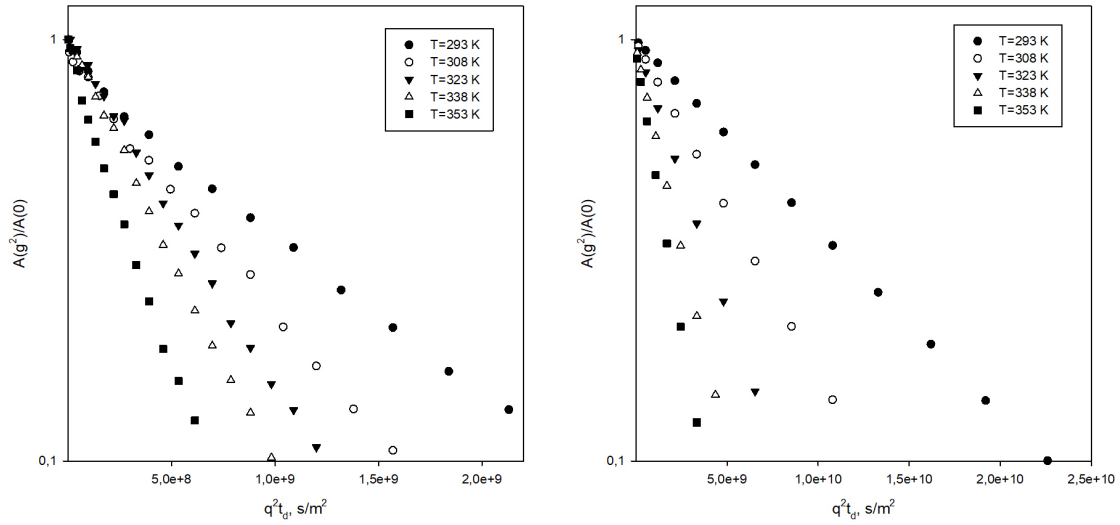

Figure 4.4. PGF NMR signal attenuation for liquid (a) and dry (b) samples for different temperatures in the range 293-353 K

from a values of dry sample. For both samples as expected there is an increase in SDCs as temperature increase. Moreover, for each individual sample there are about one order of magnitude difference in SDC in comparison to the lowest and the highest investigated temperatures. It is important, that in both cases the lines do not change their slope direction. In fact, this means that in present range of temperatures phase transition does not occur, thus the polyelectrolyte structure is kept constant.

Diffusion activation energies were estimated regressing data onto Arrhenius equation $D = D_0 \exp \frac{-E_D}{RT}$. Corresponding values of E_D for liquid and dried samples were 53.16 and 81.16 kJ/mol. In comparison, for PEO-LiTFSI solid polyelectrolyte (PEO molecular weight was $M_w = 10^5$, EO:Li ratio was 30:1) activation energy was found 38.15 kJ/mol [59], that is probably lower due to smaller salt concentration.

4.4 Conclusions

In summary, PGF NMR studies have shown different lithium dynamics in liquid and dried polyelectrolytes. Generally, the structure of both samples are quite

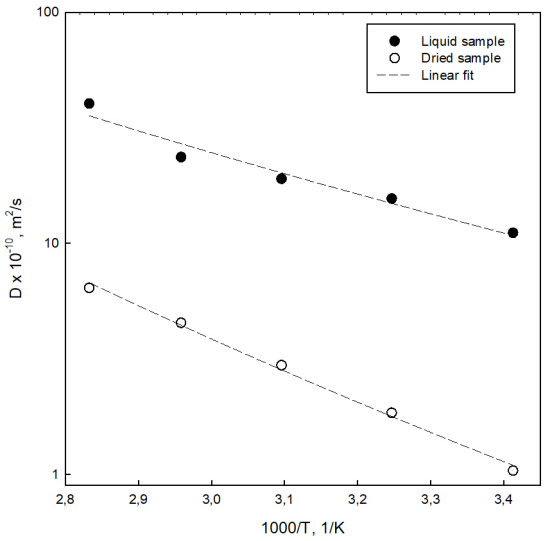

Figure 4.5. Diffusion coefficients

complex, thus the apparent diffusion coefficients were derived – $8.49\times10^{-10}\,\mathrm{m}^2/\mathrm{s}$ and $1.05\times10^{-10}\,\mathrm{m}^2/\mathrm{s}$ for liquid and dried samples correspondingly. The presence of two attenuating signals in case of dried sample can point to differently diffusing lithium phases, such as dissociated and aggregated salt.

Chapter 5

Molecular Dynamics study of PEO-$LiClO_4$

This chapter describes the results of molecular dynamics simulations of structure of the amorphous PEO-$LiClO_4$ polyelectrolyte and lithium transport properties. Two different salt concentrations in PEO were considered – the standard polyelectrolyte composition used for organic memristive device and half of this salt concentration. The effect of water, incorporated to these systems in different proportions, on the polyelectrolyte structure and lithium dynamics were revealed.

This part of the study was motivated by a problem if the standard polyelectrolyte composition, namely salt concentration, provides the optimal ionic transport in PEO and what is the role of water, presenting in the polyelectrolyte systems by the nature.

5.1 The model and computational details

All MD simulations were performed using LAMMPS code [60, 61] implemented in MedeA® program [62]. The commercial PCFF+ (Polymer consistent force field) parameters derived from ab-initio energy surfaces were used to construct interatomic potential describing interactions between atoms. The cation and anion charges were reduced to $\pm 0.5\,e$ to model polarizability of PEO matrix [63]. Van der Waals interactions were calculated by Lennard-Jones potential with added tail corrections [64]; electrostatic interactions were taken into account by particle-particle

particle-mesh (PPPM) method [65], non-bond interactions cutoff was 9.5 $\mathring{A}$.

The initial amorphous bulk polyelectrolyte was constructed by corresponding number of CH_3-O-(CH_2-CH_2-O)$_{19}$-CH_3 and $LiClO_4$ molecules to obtain two salt concentrations with EO:Li ratios of 4.5:1 and 9:1 (P(EO)$_{4.5}$-$LiClO_4$ and P(EO)$_9$-$LiClO_4$ respectively). The molecular mass of pure PEO was 8820 g/mol. Diluted polyelectrolytes were obtained combining different number of PEO oligomers, salt and water molecules corresponding to final water concentration of wt% 19.02, 37.00, 54.02 and 80.00%. Three different simulation cells for every listed structure were generated in order to exclude the influence of initial configuration on the final results. Then every calculated parameter was averaged over these configurations.

All systems, structured initially with an elevated density (1.0 g/cm^3), were, first, minimized using conjugated gradient method, then compressed in NPT ensemble changing pressure from 0.5 to 0.9 GPa at 300 K for 10 ps and annealed in NVT ensemble from 1000 to 300 K with a step of 50 K with equilibration time of 10 ps for every step. Final integration was performed in NPT ensemble at 300 K and 1 atm for 1 ns. Nose-Hoover thermostat and barostat were employed to control temperature and pressure respectively. The subsequent production runs in NPT ensemble for 5 ns were performed to collect trajectories every 2.5 ps and to analyze transport properties. For all the simulations integration time step was 1 fs.

5.2 The model verification

Since for MD simulations we used standard force field developed for polymers, in order to examine usability of PCFF+, we validated pure amorphous PEO model calculating static structure factor S(k) (SSF) reflecting long-range correlations of the system and comparing with neutron diffraction data [66]. The total S(k) was obtained as Ashcroft-Langreth type of superposition of partial static structure factors S$_{\alpha\beta}$(k):

$$S(k) = \frac{\sum_{\alpha,\beta} b_\alpha b_\beta (c_\alpha c_\beta)^{1/2} [S_{\alpha\beta}(k) + 1]}{\sum_\alpha c_\alpha b_\alpha^2}, \tag{5.1}$$

where k is a wave number; $c_\alpha = N_\alpha/N$ is a concentration, defined as a ratio between number of atoms of type α and total number of atoms; b_α is a bound coherent

scattering length of a specie, determined from neutron scattering experiments. Scattering lengths used to calculate pure PEO static structure factor are shown in Tab. 5.1.

Table 5.1. Bound coherent scattering lengths

Specie	**Scattering length [67], fm**
C	6.646
1H	-2.729
O	5.803

Hydrogen atoms for SSF calculations were treated as protons, because neutron experiments were performed on protonated PEO [66].

The partial static structure functions $S_{\alpha\beta}(k)$ were calculated as a Fourier transform of the partial pair correlation functions (PCF):

$$S_{\alpha\beta}(k) = \delta_{\alpha\beta} + 4\pi\rho(c_\alpha c_\beta)^{1/2} \int_0^\infty r^2 \frac{\sin(kr)}{kr}(g_{\alpha\beta}(r) - 1)dr, \tag{5.2}$$

where $\delta_{\alpha\beta}$ is a Kronecker symbol, ρ is a relative number of a species in a given volume, r is an atomic position, $g_{\alpha\beta}(r)$ is a partial pair correlation function of the species α and β given by:

$$g_{\alpha\beta}(r) = \frac{1}{4\pi r^2} \frac{N}{\rho N_\alpha N_\beta} \sum_{i=1}^{N_\alpha} \sum_{j\neq i}^{N_\beta} \langle \delta(\mathbf{r} - |\mathbf{r}_j - \mathbf{r}_i|\rangle, \tag{5.3}$$

where $\mathbf{r}_i$ is a coordinate of atom i, N is a total number of atoms, N_α and N_β is a number of the species α and β correspondingly.

Comparison of experimental and calculated using Eq.5.1 total SSF in comparison with experimental data is shown in Fig.5.1. As we can see, calculated $S(k)$ slightly differs from experimental curve by the peak widths, nevertheless, the achieved agreement is enough. Therefore, commercial PCFF+ forcefield can be employed to model amorphous PEO structure. It is necessary to notice, that experimental data in [66] were obtained for a sample at $363\,K$, while reported data was obtained at $300\,K$. Preliminary test simulations did not show significant difference in pure PEO structure evaluated by total SSF, thus results are presented for the case of room temperature.

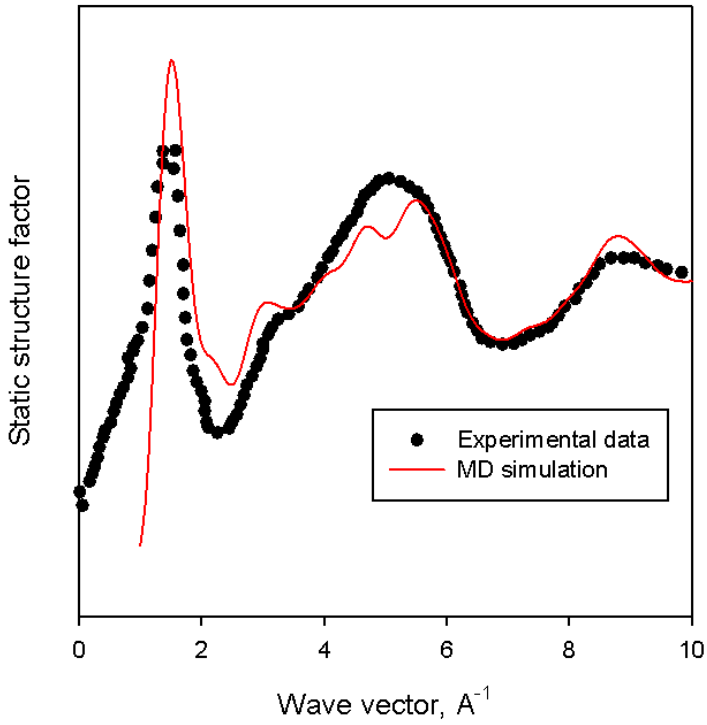

Figure 5.1. Calculated static structure factor of pure amorphous PEO at 300 K compared with experimental data obtained by neutron diffraction [66]

5.3 The polyelectrolyte structural properties

5.3.1 Density

A density of a certain polyelectrolyte cell was evaluated as a ratio between total mass of the polyelectrolyte components and cell volume: $\rho = \sum_\alpha N_\alpha M_\alpha / N_A V$, where N_A is the Avogadro constant, M_α is the atomic mass of certain atomic species, N_α is their number and V is a cell volume.

Typical density evolution during NPT integration performed for last 5 ns is shown in Fig.5.2 for $P(EO)_{4.5}$-$LiClO_4$ in case of wt% 0, 37, 80% hydration levels. A significant change of density of the systems during these 5 ns of integration was not observed, because the previously performed equilibration steps have already brought the systems to equilibrium density. Mean densities, evaluated averaging this data over 5 ns and different initial structures, are listed in Table 5.2.

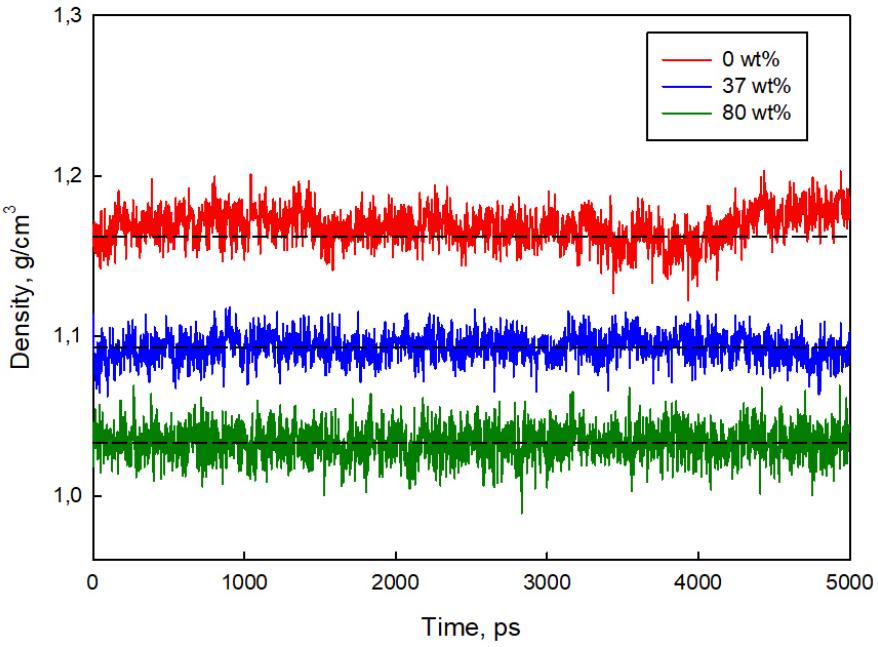

Figure 5.2. Density evolution of waterless and hydrated (wt%=37%; 80%) $P(EO)_{4.5}$-$LiClO_4$ polyelectrolyte during production runs in NPT ensemble

Table 5.2. Equilibrated densities of the modelled systems

System	**Water content, wt%**	**Density, g/cm^3**
pure PEO	-	1.015 ± 0.004[1]
$P(EO)_{4.5}$-$LiClO_4$	0	1.175 ± 0.011
	19.02	1.125 ± 0.001
	37.00	1.093 ± 0.002
	54.02	1.081 ± 0.001
	80.00	1.033 ± 0.001
$P(EO)_9$-$LiClO_4$	0	1.120 ± 0.001
	19.02	1.091 ± 0.003
	37.00	1.072 ± 0.001
	54.02	1.052 ± 0.001
	80.00	1.031 ± 0.001

[1] Exp. 1.21 g/cm^3 [63]

5.3.2 Lithium local environment

To analyze lithium local environment in PEO we calculated partial pair correlation function (PCF). This function defines the probability to find a particle in a distance r from a reference particle. When it is averaged over all Li cations, the information on average lithium short-range structure, which reflects its dissolution in PEO, is given.

Calculated partial PCFs for lithium in waterless $P(EO)_{4.5}$-$LiClO_4$ are presented in Fig.5.3a. First peaks of $g_{\alpha\beta}$ functions of Li-$O_{polymer}$ and Li-O_{salt} pairs are located at different, but very close distances, that means lithium first coordination shell is formed by oxygen atoms from the polymer and salt. The average distance between Li and $O_{polymer}$ is 2.71 $\mathring{A}$, that is slightly higher than experimental value of 2.07 $\mathring{A}$ obtained from the analysis of neutron diffraction data [31] of more diluted $P(EO)_{7.5}$-$LiClO_4$ at 373 K. MD simulations of $P(EO)_8$-$LiClO_4$ gave Li-$O_{polymer}$ distance equal to 1.95 $\mathring{A}$ [68]. Water incorporation does not change lithium local structure significantly (Fig.5.3b for wt% = 37); Li-O_{salt} distance slightly decreases from 3.06 $\mathring{A}$ to 2.95 $\mathring{A}$, and water oxygen ions appear in lithium coordination at distance equal to 2.87 $\mathring{A}$.

The peak intensities refer to running coordination number (CN):

$$n(r) = \int_0^\infty g_{\alpha\beta}(r')dr'. \tag{5.4}$$

The Fig.5.4a shows about three ions of $O_{polymer}$ and the same number of O_{salt} in the first lithium coordination in case of waterless system. Mentioned previously neutron diffraction experiments [31] showed 4-5 oxygen ions surrounding Li. MD simulations [68] have revealed three polymer and two salt oxygen ions in the lithium first coordination, that is consistent with our model.

As it was mentioned above, incorporation of water molecules does not change lithium environment significantly. As it can be seen from Fig.5.4b there are the same number $O_{polymer}$, while a number of O_{salt} slightly reduces. Additional O_{water} ion at average distance 2.83 $\mathring{A}$ appears in cation first coordination. It means that in the presence of water there is less cation-anion interaction, because part of the anions around lithium are replaced by water molecules.

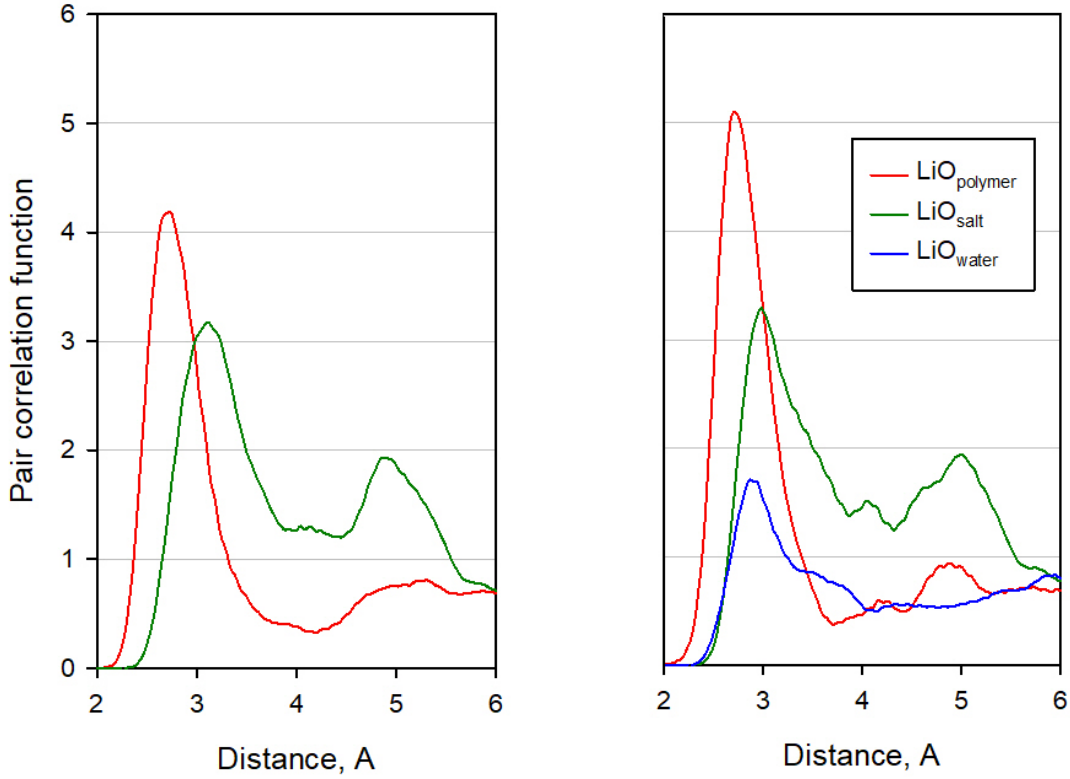

Figure 5.3. Calculated partial pair correlation functions of waterless (a) and hydrated (wt% = 37%) (b) $P(EO)_{4.5}$-$LiClO_4$ polyelectrolyte

5.3.3 Polyelectrolyte long-range structure

On the next step of our study, the long-range structure of modelled systems was calculated and analyzed. The computed functions of waterless and hydrated (in case of hydration level of wt%=37%) $P(EO)_4$-$LiClO_4$ polyelectrolyte compared with the experimental data [31] obtained for $P(EO)_{7.5}$-$LiClO_4$ by means of neutron diffraction are presented in Fig.5.5. A good agreement between calculated and experimental curves for the dry polyelectrolyte is observed, confirming the usability of the standard force field to model the present polyelectrolyte systems.

The small peak, observed in the experimental curve around $k = 0.75\,\mathring{A}^{-1}$ was identified in the literature as a feature related to extended range order, proposed for electrolytes. Namely, the peak appears due to the presence of remnants of

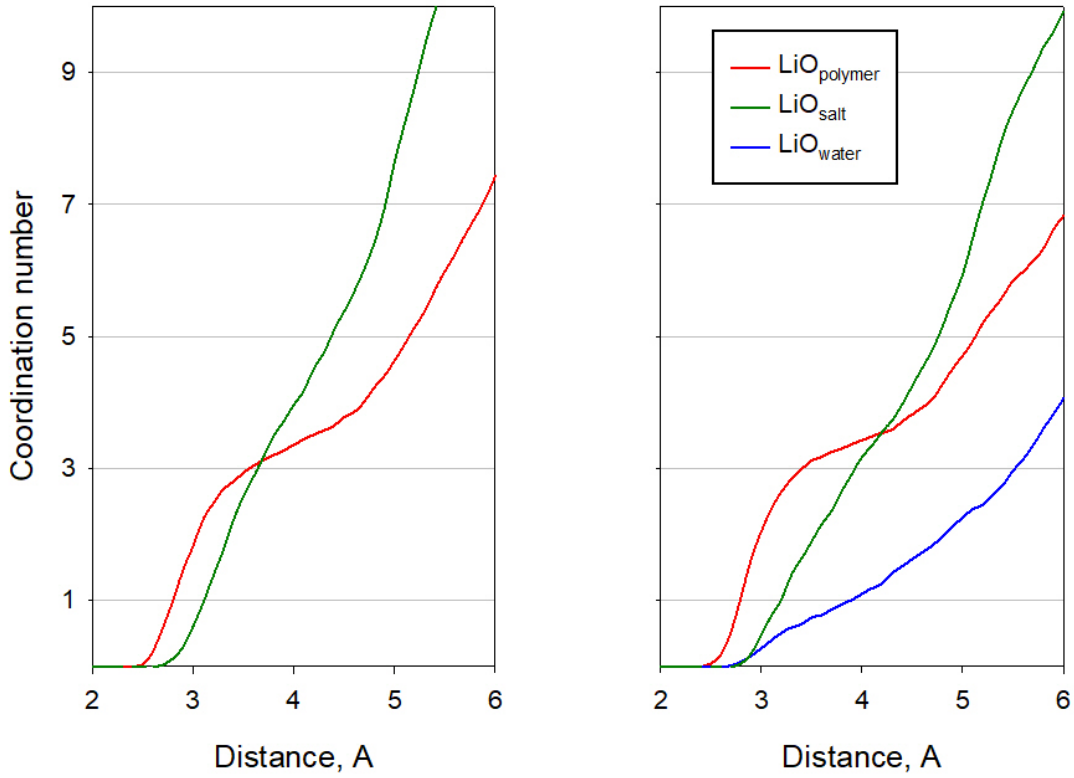

Figure 5.4. Calculated running coordination number of waterless (a) and hydrated (wt% = 37%) (b) $P(EO)_{4.5}$-$LiClO_4$ polyelectrolyte

crystalline phase of $P(EO)_6$:LiX (X = ClO_4 [31], TFSI [69]) even in the amorphous structure. Similar low-k feature for dry polyelectrolyte was found in our simulations, located at $0.63\,\mathring{A}^{-1}$.

The second peak at $k = 1.50\,\mathring{A}^{-1}$ of the experimental and at $k = 1.52\,\mathring{A}^{-1}$ of the calculated SSF is related to intermediate range-order of the polymer chains. The peak intensity dependence on the system density and its enhancement with respect to pure amorphous PEO due to expansion of the polymer network upon complexing with salt were figured out in the previous work [31].

Two differences is observed for calculated SSF in case of hydrated polyelectrolyte model. First, the low-k peak disappears. And the second, main peak becomes slightly weaker.

In order to establish the origin of the peaks observed for the calculated func-

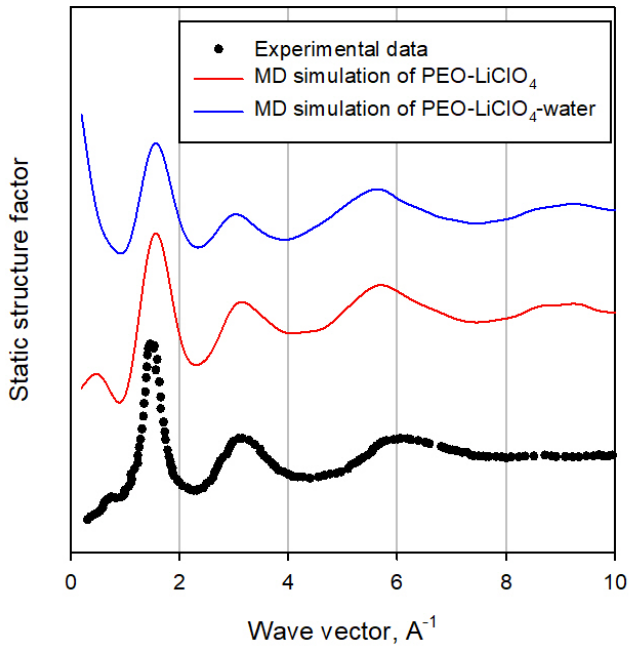

Figure 5.5. Calculated static structure factor of waterless and hydrated (wt% = 37%) $P(EO)_{4.5}$-$LiClO_4$ polyelectrolyte compared with experimental data obtained by neutron diffraction for $P(EO)_{7.5}$-$LiClO_4$ amorphous polyelectrolyte [31]

tions, we plotted partial SSFs (Fig.5.3.3). The $SSF_{polymer}$ considers only PEO and SSF_{salt} only $LiClO_4$ salt atoms, while for $SSF_{polymer\text{-}salt}$ the both polymer and salt were included in evaluation of SSF according to Eq.5.3. The low-k peak comes from SSF_{salt} and $SSF_{polymer}$ (Fig.5.3.3a). The latter also contributes to the main peak at $k = 1.52\,\mathring{A}^{-1}$ along with $SSF_{polymer\text{-}salt}$. These results confirm that extended-range order found in the experimental SSF [69] of the amorphous $LiClO_4$ doped PEO arises from a long-range order of salt and PEO chains. In case of hydrated polyelectrolyte, as it is seen in Fig.5.3.3b, the long-range order of ionic species disappears. Thus water acts preventing ordered arrangement of the polyelectrolyte components.

The little decrease of the main peak in SSF of hydrated system is related to corresponding decrease of $SSF_{polymer\text{-}salt}$ (Fig.5.3.3b). As it was pointed above, this intermediate range order reflects complexation of PEO with salt, therefore the peak decrease can indicate the less complexation of the polymer matrix and salt

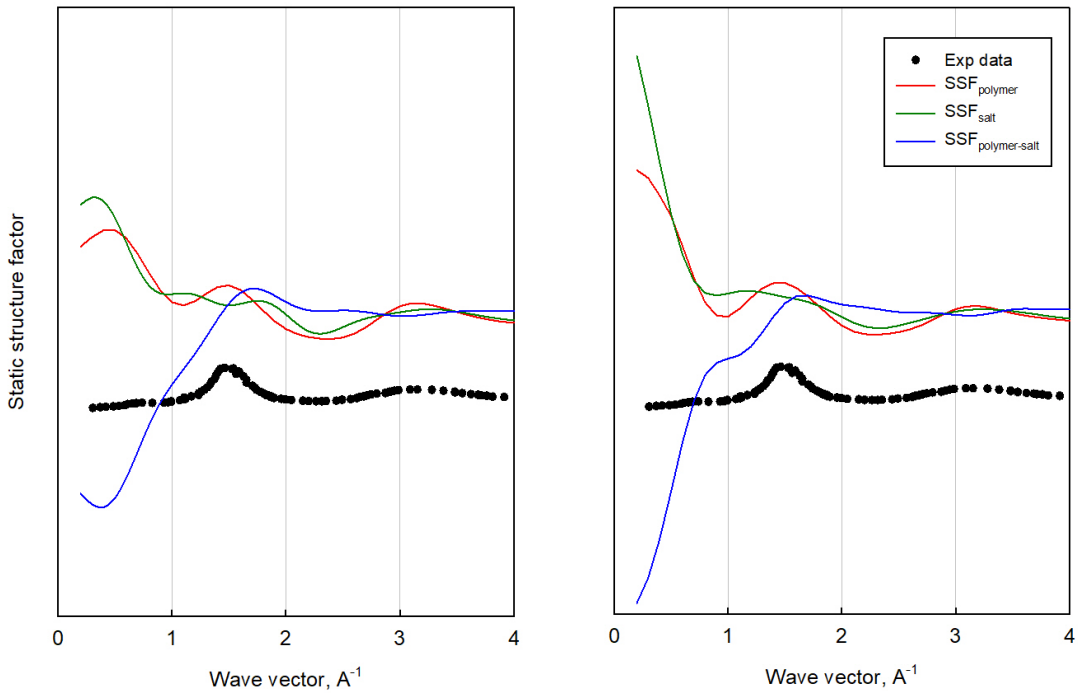

Figure 5.6. Calculated partial static structure factors of waterless (a) and hydrated (wt% = 37%) (b) $P(EO)_{4.5}$-$LiClO_4$ polyelectrolyte

in the presence of water.

5.3.4 Fractional Free Volume

Free volume is an important value, when transport of ionic species and small molecules in polymers are studied. According to the free volume theory, it characterizes volume, created by segmental motion of polymer chains, accessible for molecules and ions to migrate into [70]. Quantitatively, fractional free volume (FFV) can be defined as:

$$FFV = \frac{V - 1.3V_{vdW}}{V}, \tag{5.5}$$

where V is the total and V_{vdW} is the van der Waals volume. While the total volume can be easily calculated from the spatial sizes of simulation box, V_{vdW} reflects the volume occupied by a molecule. This occupied space, which is impenetrable to

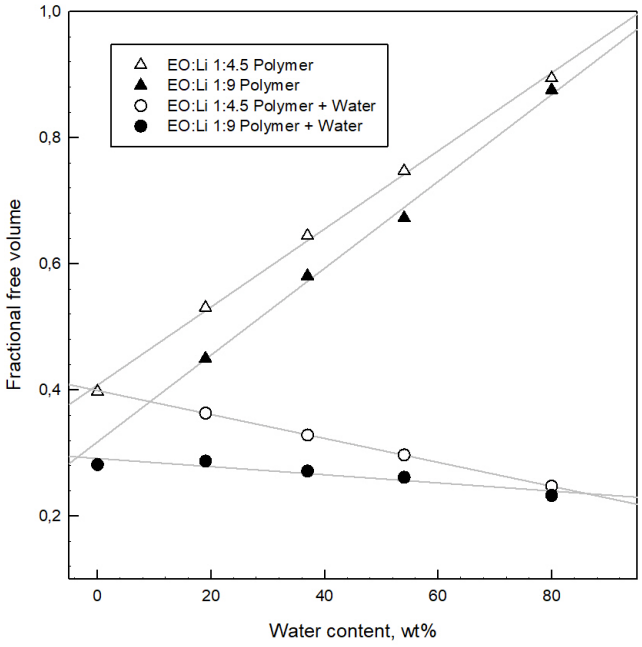

Figure 5.7. Fractional free volume created by polymer or polymer and water together in $P(EO)_{4.5}$-$LiClO_4$ and $P(EO)_9$-$LiClO_4$ at different water content

other species, can be evaluated using following expression [71]:

$$V_{vdW} = N_A \left[\frac{4}{3}\pi R^3 - \sum \pi h_i^2 \left(R - \frac{h_i}{3}\right) \right], \tag{5.6}$$

with

$$h_i = R - \frac{l_i}{2} - \frac{R^2}{2l_i} + \frac{r_i^2}{2l_i},$$

where N_A is the Avogadro constant, r_i is the radius of the i-th atom, l_i is the bond distance between the i-th and the neighboring atom. Usually, V_{vdW} of a molecule can be calculated as a sum of the precalculated volumes of the composing structural groups. We used the Bondi method to calculate V_{vdW} of the polymer under study.

Calculated FFV of the modelled systems depending on water concentration is shown in Fig.5.7. As expected, FFV value increases with water addition, that can be due to the effect of water on segmental mobility of the polymer chains: the more mobile the chains, the more free volume they create. When the volume, occupied by polymer and water considered together, that means the free

volume accessible for salt only is calculated, FFV in case of high salt concentration ($P(EO)_{4.5}$-$LiClO_4$) decreases with water concentration increase, whereas it is almost constant in case of the lower salt concentration in PEO ($P(EO)_9$-$LiClO_4$). This different behaviour can be explained as follows: at high salt concentration salt molecules form aggregates, and consequently, salt does not occupy the voids produced by polymer chains. Instead, it creates additional volume in the system. At lower salt concentration salt is dissolved in the polymer matrix, thus it occupies free volume created by polymer chains, and consequently there is no significant alternation of accessible free volume for salt with changing water concentration. Therefore, water helps to prevent salt aggregation, when its concentration is too high to dissociate in the polymer matrix.

5.3.5 Spatial density distribution of the polyelectrolyte components

The polyelectrolyte composition was quantitatively estimated by constructing spatial density functions for every polyelectrolyte component (polymer, cation, anion, water) and calculating their mutual overlapping. Every atom density was simply represented by the Gaussian function:

$$\rho_i(r) = \frac{1}{\sqrt{2\pi}\sigma} \exp -\frac{r^2}{2\sigma}, \tag{5.7}$$

where $\mathbf{r}$ is a position of the i-th atom. The total spatial density function of the given species was calculated as their sum in a spatial mesh of size 60×60×60:

$$\rho_\alpha(r) = \sum_i \rho_i(r), \tag{5.8}$$

where α corresponds to a certain polyelectrolyte component.

Relative mutual penetration of every pair of atomic species was evaluated by:

$$p = \int_r \rho_\alpha(r)\rho_\beta(r)dr, \tag{5.9}$$

where $\rho(r)$ is the spatial distribution of atomic density of α and β pair of atomic species; p =1 means total overlapping, while p =0 stands for no overlapping.

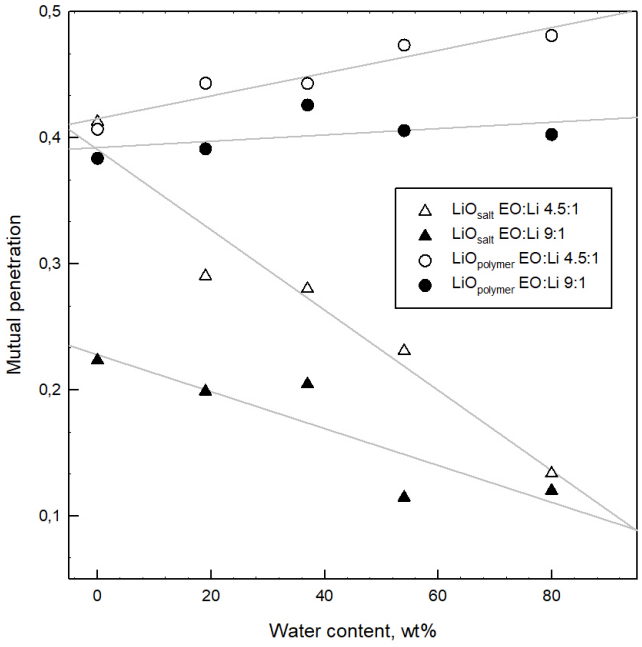

Figure 5.8. Relative mutual penetration of lithium ions with polymer and salt oxygen ions in the polyelectrolyte systems with salt concentrations corresponding to EO:Li ratios of 4.5:1 and 9:1 with different water content

Calculated p values for Li-$O_{polymer}$ and Li-O_{salt} pair components at different hydration levels in the modelled polyelectrolyte systems are shown in Fig.5.8. It is clearly seen that the overlap of the density of lithium with the density of its anion decreases with increasing the water content for both salt concentrations. This indicates salt dissociation with water incorporation. Moreover, the overlap of the density of lithium with the density of the polymer oxygen atoms increases significantly in case of $P(EO)_{4.5}$-$LiClO_4$, meaning that water addition not only prevents cluster formation, but also enhance the association of lithium with polymer, or in other words, its dissolution in PEO matrix.

Three dimensional plots of the density surfaces calculated for every polyelectrolyte component using Eq.5.8 are shown in Fig.5.9 for dry (b) and wet (c) (water concentration wt%=54.02%) polyelectrolyte systems with EO:Li ratio of 4.5:1. The formation of salt clusters in the dry polyelectrolyte is observed, whereas less aggregation is visually seen in the presence of water.

The composition of the equilibrated amorphous polyelectrolytes were quanti-

tatively estimated by the mutual penetration of the polymer, water and salt by constructing the spatial density distribution function for given components and calculating their overlapping.

Density of a particle of the system was represented by the Gaussian function:

It is seen from calculated p values, that in waterless system Li density is more overlapped by cation density, than polymer. This results, again, from high salt concentration in the system. Water addition decrease Li-O_{salt} overlapping, as well as Li-$O_{polymer}$ p value decreases. Moreover, it could be noticed, that when water concentration increase, no significant changes appear.

Representation of three dimensional spatial density distribution is shown in Fig.5.9. In case of dry polyelectrolyte (Fig.5.9a) salt clusters are observed, while addition of water to the amorphous polyelectrolyte makes these aggregates smaller (Fig.5.9b).

5.4 Transport properties

5.4.1 Lithium self-diffusion coefficients

Lithium self-diffusion coefficients were evaluated from the linear diffusive regime of their mean square displacement (MSD) using Einstein equation:

$$D = \frac{1}{6t} \sum_{i}^{N} \langle [\mathbf{r}_i(t) - \mathbf{r}_i(0)]^2 \rangle, \tag{5.10}$$

where difference of a lithium ion position at time t and initial $t = 0$, defined as $[\mathbf{r}_i(t) - \mathbf{r}_i(0)]$, represents its displacement during time t, N is a total number of diffusing species.

Calculated lithium SDCs are presented in Fig.5.10 for $P(EO)_{4.5}$-$LiClO_4$ and $P(EO)_9$-$LiClO_4$ at different water content compared to experimentally obtained values by PGF NMR technique (Chapter 4). It is worth to notice that for experimental SDC values the water content of the gel sample was evaluated directly from volumes used for solution preparation, while for dried sample the minimal amount of water corresponding to hydrated lithium ions was only considered.

First, it is necessary to notice that for the dry polyelectrolyte models $P(EO)_{4.5}$-

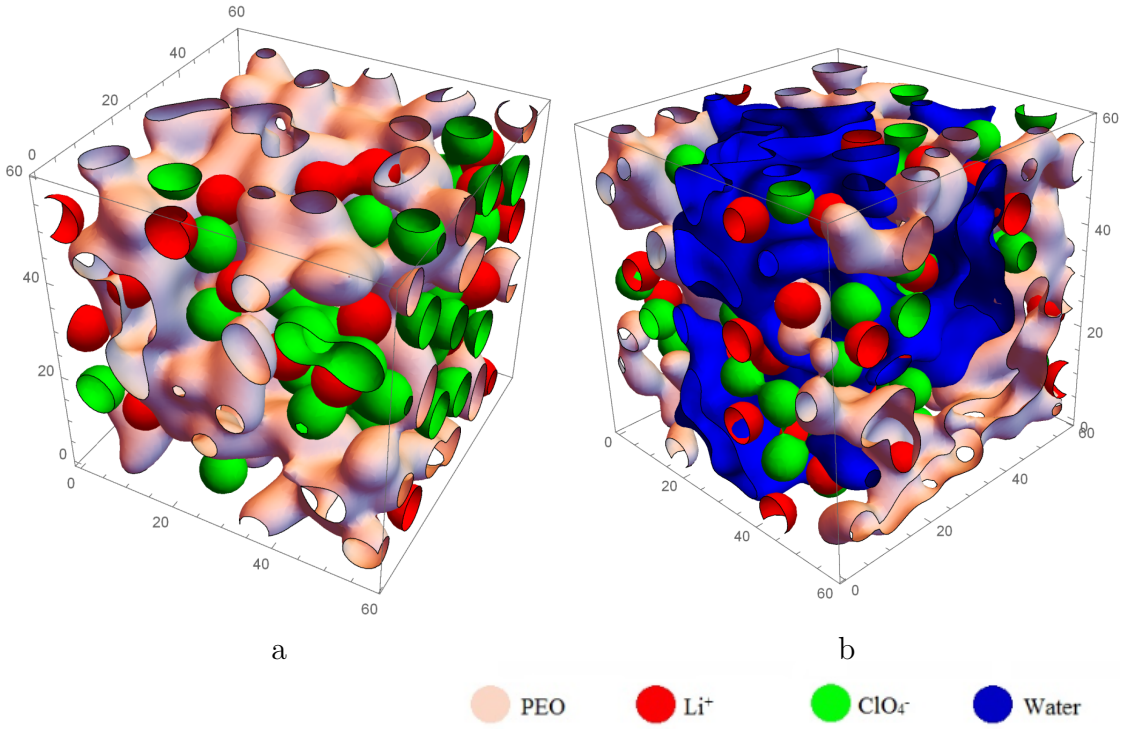

Figure 5.9. Density distribution of the polymer, water and salt components of the amorphous P(EO)-$LiClO_4$ systems. Pink areas represent the polymer density, red corresponds to the density of the cations, the green – anions, the blue – water. Simulation cell dimension is about 30 $\AA$. density distribution of the polymer, water and salt components of the amorphous P(EO)-$LiClO_{4.5}$ in dry condition (b) and containing wt% = 54.02% of water (c)

$LiClO_4$ gives almost twice less Li self-diffusion coefficient, than P(EO)$_9$-$LiClO_4$ ($(1.61 \pm 0.07)\times10^{-11}$ and $(2.57 \pm 0.11)\times10^{-11}\,m^2/s$ correspondingly). Second, as expected, water concentration increase leads to Li self-diffusion coefficients growing, that can be a combined effect of free volume increase and reduction of Coloumbic interactions between cations and anions, preventing salt aggregates formation. Calculated values are in a good agreement with experimentally measured data. Although the most diluted sample was inaccessible for the simulations due to extremely large number of particles leading to time-consuming calculations, the tendency of the self-diffusion coefficient to vary as a function of the water concentration in the polyelectrolyte is well followed according to the measured values.

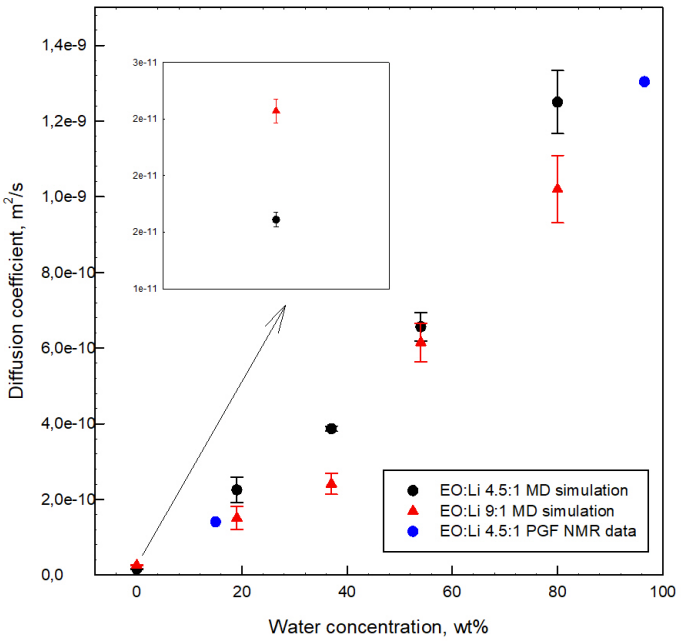

Figure 5.10. Self-diffusion coefficients of Li ions in the polyelectrolyte systems with salt concentrations corresponding to EO:Li ratios of 4.5:1 and 9:1 with different water content. Experimentally measured lithium self-diffusion coefficients are presented for comparison

5.4.2 Lithium instantaneous environment

In order to trace lithium hoppings in time we calculated lithium instantaneous coordination number. Lithium correlations with polymer, anion and water oxygen atoms were considered. Calculated lithium coordination numbers for $P(EO)_{4.5}$-$LiClO_4$ containing 0, 54.02 and 80% of water content are presented in Fig.5.11. At dry conditions, lithium is equally coordinated by polymer and salt oxygen ions, while water addition leads to the decrease a number of salt oxygen ions replacing them by water. For the most diluted system lithium moves coordinated by polymer as well as with water oxygen ions, and the contribution of salt drops almost to zero. This result confirms the previous suggestion: such lithium dynamics arises from decreased cation-anion interaction in the presence of water, while in a dry system the elevated salt concentration does not allow salt dissociation.

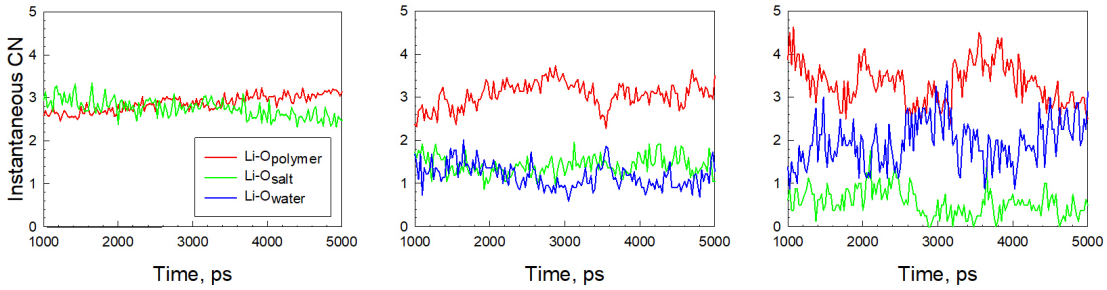

Figure 5.11. Evolution of instantaneous lithium coordination number in $P(EO)_{4.5}$-$LiClO_4$ (a) and water contained polyelectrolytes with wt% = 54.02% (b) and wt% = 80%

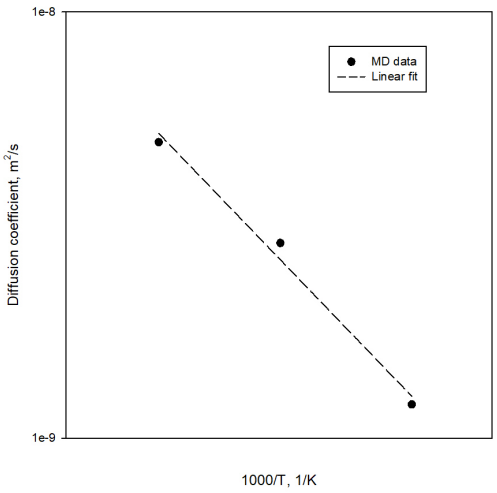

Figure 5.12. Calculated lithium self-diffusion coefficients for $P(EO)_{4.5}$-$LiClO_4$ containing wt%=80% of water plotted versus reciprocal temperature

5.4.3 Temperature effect

Temperature effect was evaluated calculating lithium SDC from trajectories obtained at 300, 325 and 350 K for $P(EO)_{4.5}$-$LiClO_4$ containing 80% of water. Arrhenius analysis gave diffusion activation energy of 71.62 kJ/mol, that is higher comparing to experimental data obtained for the most diluted sample (96% of water), but still is in a good agreement with it.

5.5 Conclusions

MD simulations have shown that salt concentration in the standard OMD preparation $P(EO)_{4.5}$-$LiClO_4$ polyelectrolyte is too high that leads to salt aggregation, whereas the system with a half of this concentration does not show salt aggregates formation. In terms of self-diffusion coefficients calculated from lithium trajectories, former system has almost twice less self-diffusion coefficient than the latter one. In the presence of water, the interactions between cations and anions are reduced. This leads to an increased dissolution of the salt in the polymer matrix. Consequently, water prevents the formation of salt aggregates.

Calculated self-diffusion coefficients are in a good agreement with the measured data. The growth of the self-diffusion coefficients with an increase of water concentration is associated both with the formation of more free volume and salt aggregation decrease.

Chapter 6

Phase composition of the polyelectrolytes

Generally, solid polymer electrolytes has a semicrystalline structure. As it was pointed out in the Section 1.2 of the Chapter 1, crystalline fraction can be formed by pure PEO, as well as by PEO-$LiClO_4$ complexes. An increase of the ionic conductivity up to the maximal value and its subsequent decrease due to possible salt aggregation in the amorphous PEO-$LiClO_4$ was emphasized in the literature [30]. In this chapter using X-ray diffraction the phase composition of the polyelectrolyte samples prepared using different salt concentration is discussed. The effect of hydrochloric acid addition, necessary to provide acidic environment for OMD operation, on the final polyelectrolyte structure is considered. Surface morphology of the polyelectrolyte samples was observed using optical microscopy.

6.1 Experimental details

The polyelectrolyte solutions were prepared as described in Section 2.1 of Chapter 2. Three different salt concentrations were used – 0.1 M, 0.05 M and 0.0025 M. The required amount of HCl was added to prepared solutions to provide pH=1 environment. Six different polyelectrolytes of three salt concentrations and each of them in acidic environment were casted on glass substrates of size about 5×3 mm and left to dry overnight at ambient environment prior to measurements. The XRD patterns of these samples were obtained using Philips HR-XRD (High Resolution

X-ray Diffractometer), based on a Goebel Mirror, that provides a parallel beam. The monochromator is based on two Germanium crystals oriented in (220) plane. The X-ray source was a cooper Cu(Kα1) line with a wavelength λ=1.5418 Å) and power 40 kV, 30 mA. The XRD patterns were recorded with a step of 0.01^o, acquisition time was 2 seconds for each step in the diffraction angles in range ($2\theta^o$) 6-60^o.

The highly dried sample with 0.1 M concentration prepared using standard protocol and casted onto teflon substrate was stored in a glove box in argon atmosphere for 4 weeks prior to measurements. The dried film was detached from the substrate and its XRD pattern was acquired using Bruker D8 Advance X-ray diffractometer with rotating sample holder using cooper Cu(Kα) (α = 1.5418 Å) radiation and continuous scan with speed of 0.005^o per second in the range of diffraction angles 10 - 100^o.

Rietveld refinement of the sample mentioned above was made using GSAS-II software [72].

Optical microscope Nikon was used to obtain micrographic images of the solid polyelectrolyte samples in reflected light mode.

6.2 X-ray diffraction data analysis

The relationship between the crystalline structure and the diffraction pattern can be solved by analyzing the characteristic diffraction peaks. First, we analyzed highly dried samples to probe a long-term polyelectrolyte structure towards stabilization of the endurance of the device. XRD pattern of PEO-$LiClO_4$ prepared in the standard salt concentration is shown in Fig.6.1.

Characteristic peaks corresponding to pure PEO crystallization are around 2θ $\approx$ 19^o and 23^o [73]. There is only one PEO peak at 2θ =23.2^o in the presented XRD pattern (Fig.6.1), while the remained peaks according to Rietveld refinement (Section 2.3.1 of Chapter 2) correspond to lithium perchlorate trihydrate phase. This can underline the fact that the formation of specific PEO-$LiClO_4$ complexes was not possible using the hydrated lithium salt found in the previous studies [15]. This is most likely due to the extremely hygroscopic nature of the lithium salts, thus even drying the polyelectrolyte in the anhydrous atmosphere does not prevent

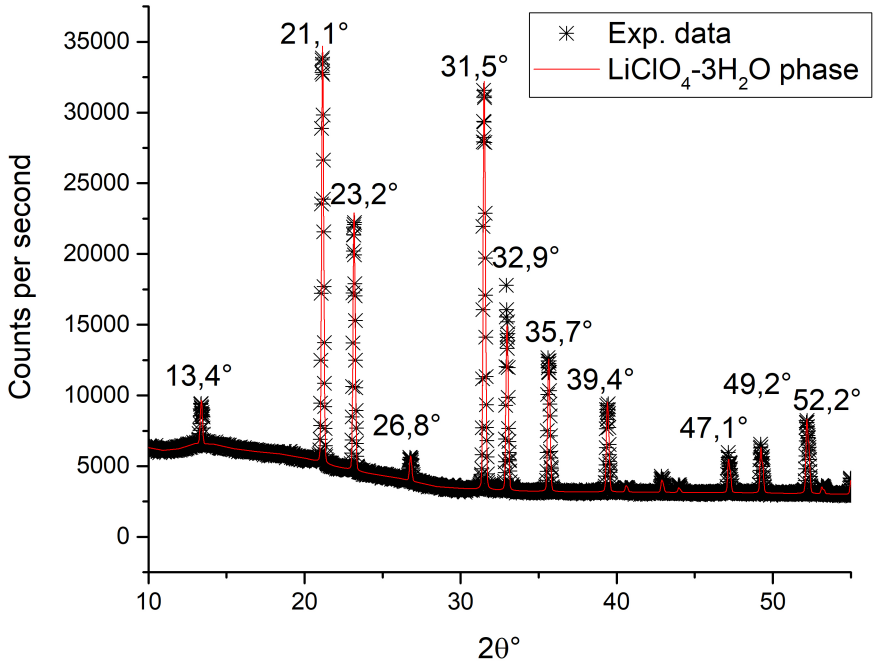

Figure 6.1. XRD pattern of the highly dried PEO-$LiClO_4$ polyelectrolyte prepared in the standard salt concentration (0.1 M $LiClO_4$ or EO:Li ratio 4.5:1) compared to refined data of $LiClO_4$ phase using Rietveld technique

the salt hydrates [74].

Further, polyelectrolytes dried at ambient environment were studied in order to define their phase composition. There are three weak diffraction peaks in the XRD pattern recorded for PEO-$LiClO_4$ presented in Fig.6.2a. The one at 2θ =23.06^o, as it was mentioned previously, corresponds to pure PEO (The partial absence of characteristic PEO peaks can be connected to the orientation of the crystallites relatively to the incident beam). The peaks at 2θ =13.2^o and 2θ =35.5^o are the characteristic salt peaks, indicating the presence of the salt crystalline aggregates even in the sample dried at atmospheric humidity. Thus, this salt concentration does not provide the full salt dissociation in PEO matrix and results in salt aggregation. This pattern persists for the sample, prepared in acidic environment (Fig.6.2b) and one additional peak of pure PEO at 2θ =19.1^o appears. However the peak intensities, reflecting a fraction of a certain phase in a sample, are higher.

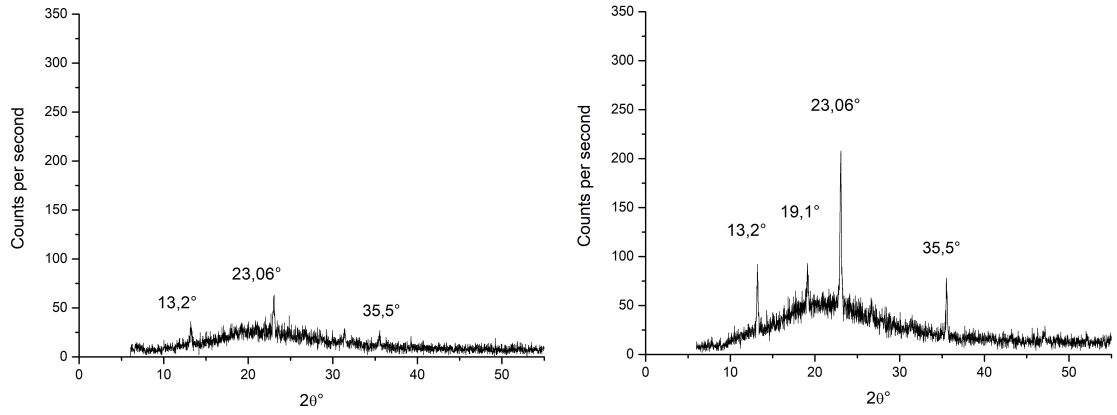

Figure 6.2. XRD pattern of PEO-$LiClO_4$ polyelectrolyte prepared in 0.1 M salt solution in neutral (a) and acidic (pH=1) environment (b)

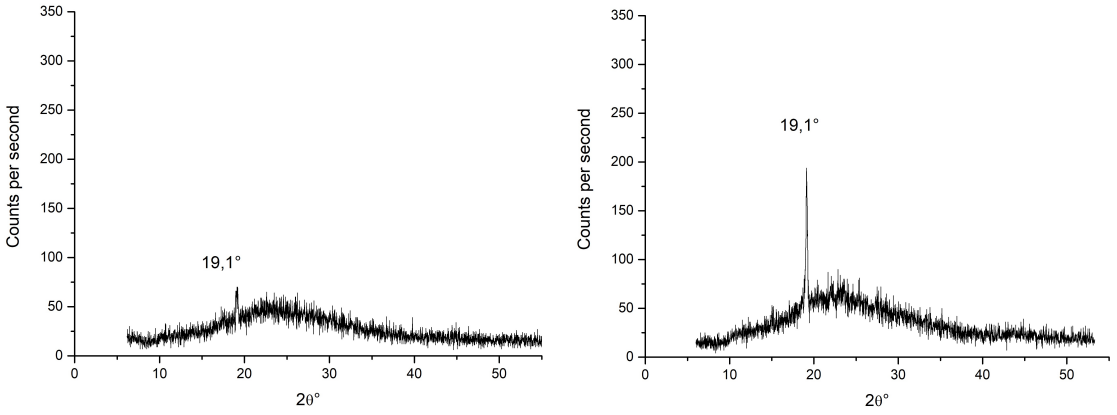

Figure 6.3. XRD pattern of PEO-$LiClO_4$ polyelectrolyte prepared in 0.05 M salt solution in neutral (a) and acidic (pH=1) environment (b)

The recorded XRD data of PEO-$LiClO_4$ polyelectrolyte prepared in 0.05 M salt solution are presented in Fig.6.3. In this salt concentration characteristic $LiClO_4 \times 3H_2O$ peaks are not observed. The only one PEO peak at $2\theta = 19.1^o$ is kept (Fig.6.3a), whereas HCl addition as in the previous case increases the total crystalline fraction of the semicrystalline sample (Fig.6.3b).

The formation of salt aggregates was also not detected in the samples with the 0.025 M salt concentration, that means its complete dissociation in the host polymer (Fig.6.4a). Similarly to the previous XRD patterns, the intensity of the pure PEO crystalline peak at $2\theta = 19.1^o$ increases with HCl addition (Fig.6.4b).

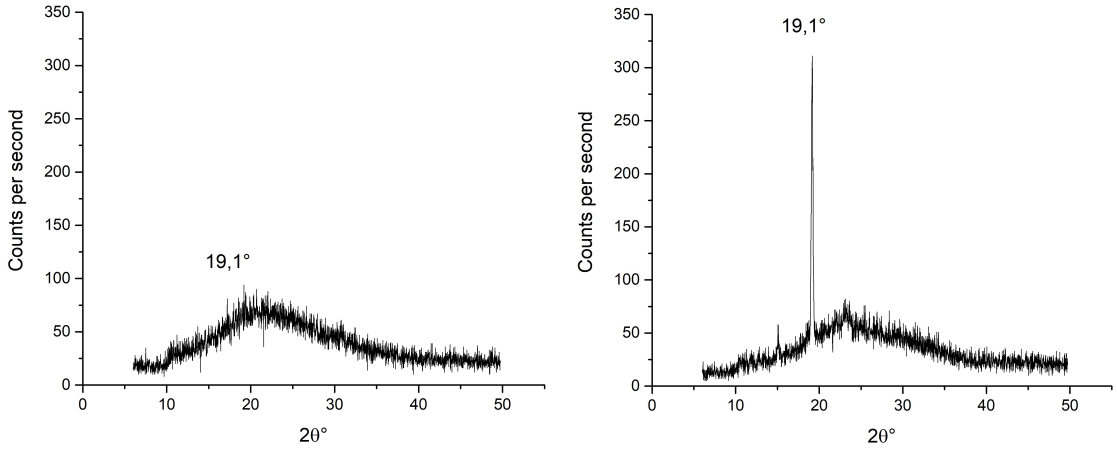

Figure 6.4. XRD pattern of PEO-$LiClO_4$ polyelectrolyte prepared in 0.025 M salt solution in neutral (a) and acidic (pH=1) environment (b)

The general trend of increasing pure PEO peaks with salt concentration decrease in lithium perchlorate trihydrate doped PEO was emphasized in the past [73]. This effect was associated with the dispersion of the ordered polymer chains due to homogeneous distribution of the salt in the PEO host. In case of neutral environment in polyelectrolytes this tendency is not clearly observed due to weak peaks compared to background amorphous component. However, for the samples prepared with HCl addition, this PEO peak intensity behaviour with variation of the salt concentration is clearly seen. Generally, the higher crystalline fraction in the samples with the acid addition can be due to the fact that the hydrochloric acid, preferably interacting with water, prevents its retention by a polymer matrix or salt, therefore, the final composition of solid polyelectrolyte, when other conditions were equal, contains less water, that facilitates crystallization of the polyelectrolyte components.

6.3 Surface morphology

The surface morphology of the solid polyelectrolyte films prepared in neutral and acidic (pH=1) solutions are shown in Fig.6.5-6.7. It can be noticed that polyelectrolytes without HCl (Figs. 6.5a,6.6a,6.7a) and one in case of HCl addition with 0.05 M salt concentration (Fig.6.6b) form spherical structures, with average

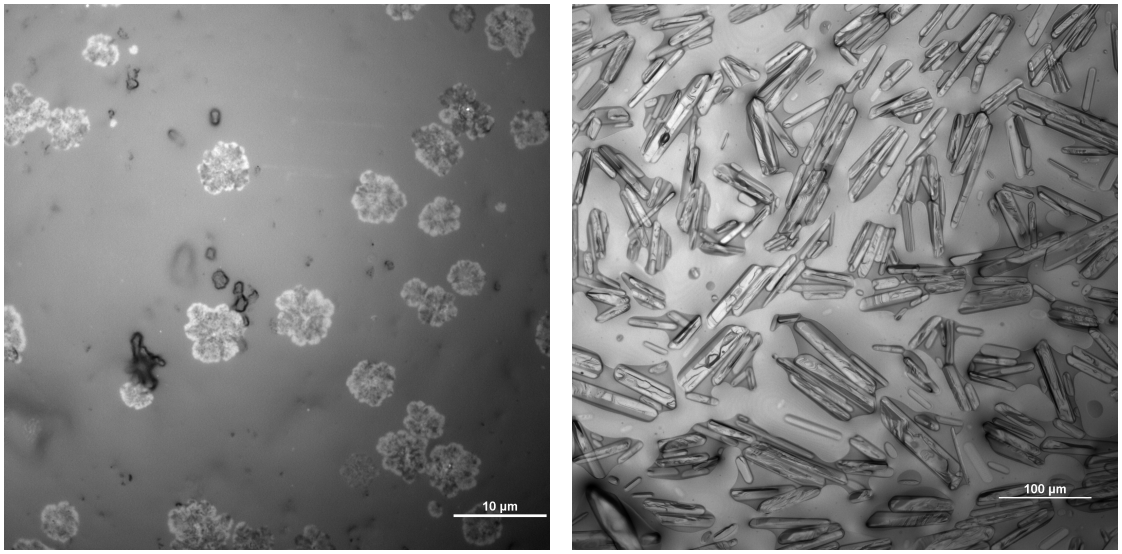

a b

Figure 6.5. Surface morphology of PEO-$LiClO_4$ polyelectrolyte prepared in 0.1 M salt solution in neutral (a) and acidic (pH=1) environment (b)

diameters of 5, 8, 1, 10 μm correspondingly.

The addition of HCl in case of 0.1 M and 0.025 M salt concentrations changes dramatically the polyelectrolytes morphology. The formation of cylindrical structures are seen in Fig.6.5b,6.7b. The latter case combines needle-like structure with spherolites of the size about 8 μm.

6.4 Conclusions

The high degree of PEO crystallinity in the polyelectrolytes is not desirable, because it reduces the total fraction of the amorphous phase of the sample, where ionic transfer appears. In the same time, formed salt aggregates decrease total number of charge carriers due to obstructed ionic transport in this phase. According to XRD study, the standard 0.1 M salt concentration in the polyelectrolyte does not provide the full salt dissolution in PEO, leading to salt aggregation during polyelectrolyte drying. The diffraction peaks of salt were not observed in case of reduced salt concentration of 0.05 M and 0.025 M. The general effect of hydrochloric acid on the structure of the polyelectrolytes was found to result in the total increase of the fraction of crystallites.

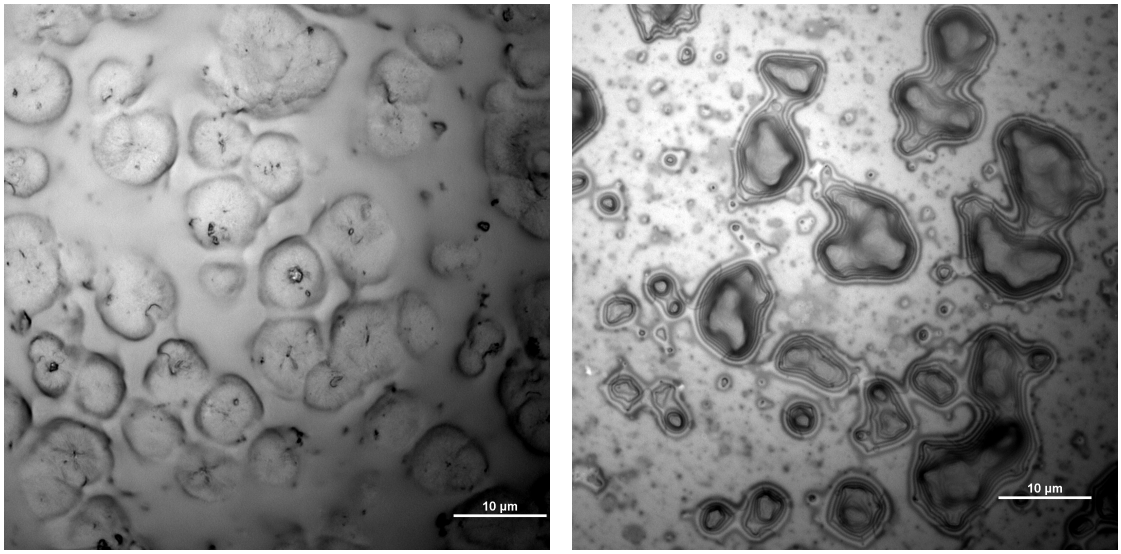

a b

Figure 6.6. Surface morphology of PEO-$LiClO_4$ polyelectrolyte prepared in 0.05 M salt solution in neutral (a) and acidic (pH=1) environment (b)

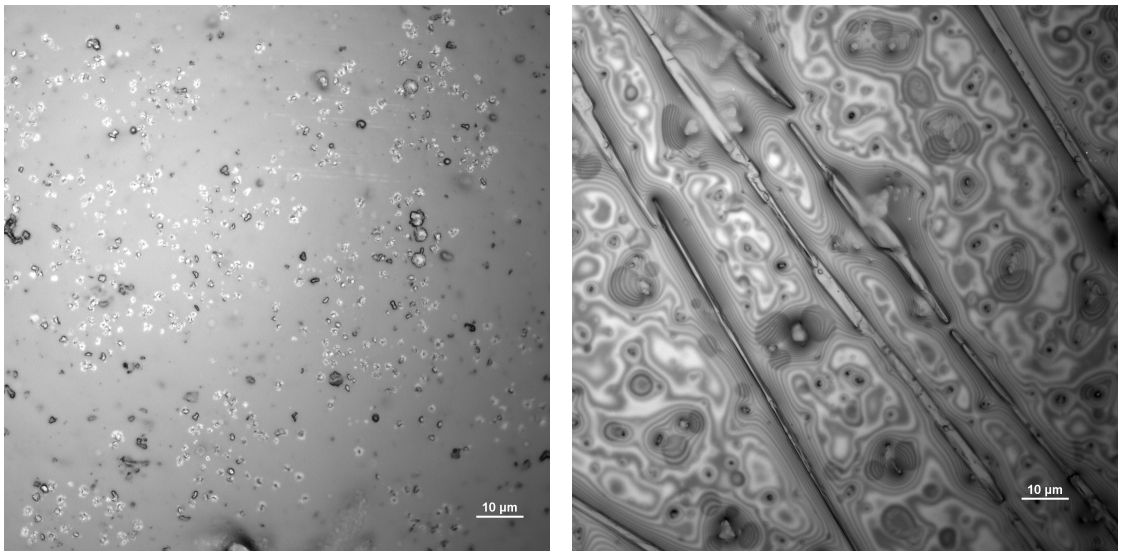

a b

Figure 6.7. Surface morphology of PEO-$LiClO_4$ polyelectrolyte prepared in 0.025 M salt solution in neutral (a) and acidic (pH=1) environment (b)

Chapter 7

Electrochemical characterization of interfaces with PEO-$LiClO_4$

The present chapter describes the results of electrochemical characterization of the polyelectrolyte/electrode and polyelectrolyte/PANI interfaces using electrochemical impedance measurements. In the study of polyelectrolytes using insoluble electrodes, the most important information that can be obtained using electrochemical impedance spectroscopy techniques is the assessment of ionic conductivities. In the case of studying a complex polyelectrolyte/PANI interface the information about variation of charge transfer processes due to PANI redox transformations can be analyzed.

7.1 Experimental details

The polyelectrolyte solutions in neutral and acidic environment were prepared as described in Section 2.1 of Chapter 2. Three salt concentrations were used – 0.1 M, 0.05 M and 0.0025 M. The amount of HCl elevated compared to standard one was added to prepared solutions to provide pH=-1 environment.

Every of six polyelectrolyte was casted onto commercial screen printed electrodes (Metrohm DropSens) schematically represented in Fig.7.1. The formed electrochemical cells were let to dry overnight before measurements. All data, derived from spectra were averaged over several independent measurements.

In order to study the polyelectrolyte/PANI interface the thin LB layer of PANI

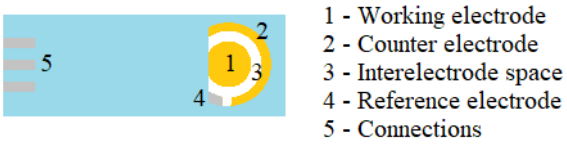

Figure 7.1. Schematic representation of the screen-printed electrode: working (1) and counter (2) gold electrodes, ceramic interelectrode space (3), silver reference electrode (4), electrode connections (5)

(see Section 2.1.1 of Chapter 2) of total number of 40 monolayers was deposited onto working electrode surface. The polyelectrolyte of standard composition (0.1 M LiClO4, pH=1) was casted onto PANI layer, to provide conducting media between working and counter electrodes and also dried prior to measurements. Two independent samples were prepared for these measurements. The bias during EIS measurements was, first, increased (applied voltage sequence was E_{dc} = -0.2 V, +0.1 V, +0.2 V, +0.3 V, +0.8 V) and then decreased back.

Cyclic voltammetry (CV) of the polyelectrolyte/PANI-coated electrode cell was recorded in the range of -1 V - +0.8 V with a scan rate of 0.1 V/s.

Impedance data and CV were collected by PalmSens4 potentiostat/impedance analyzer, using alternating voltage amplitude of E_{ac}=0.05 - 0.1 V in the range of frequencies of 1-10^6 Hz in the back sweep mode. The PSTrace5 software, supplied with the equipment were used to fit experimental impedance spectra.

7.2 Polyelectrolyte/electrode interface characterization

Typical impedance spectra recorded for PEO-$LiClO_4$/electrode samples of different salt concentration are shown in Fig.7.2a as -Im(Z)(Re(Z)) called Nyquist plot. The impedance values lying below the Re(Z) axis were observed for high frequencies (High frequency impedance values are typically plotted closer to the plot origin). In terms of equivalent electric circuit elements the presence of these negative values indicates inductive behaviour. Its interpretation is quite complex, because inductance is generally defined by electromagnetic force generated to counteract a current change. The possible explanation of this effect was done in the past: in

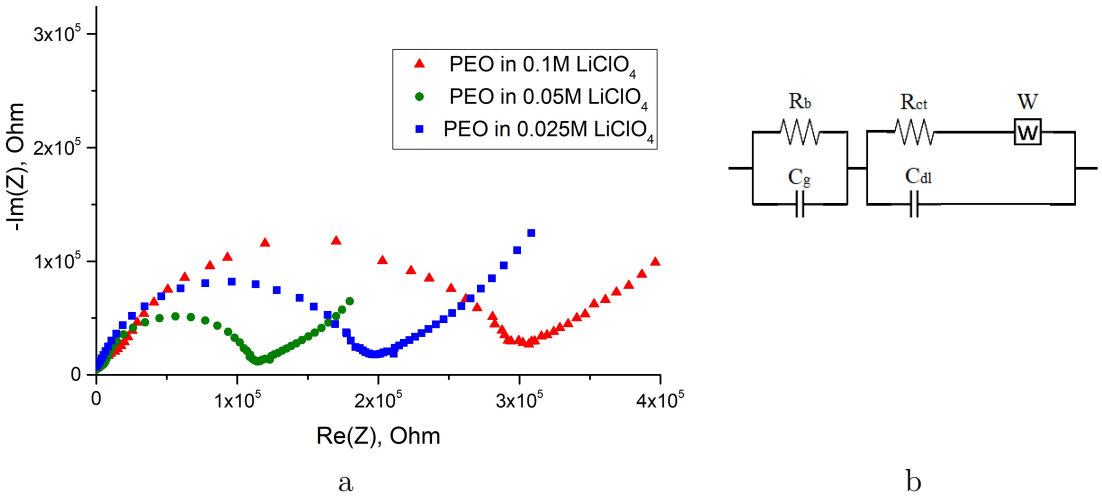

Figure 7.2. Nyquist plot of PEO-$LiClO_4$ polyelectrolyte/electrode cell impedance (a) and equivalent circuit of the system (b)

electrolytes, such a force can be created by friction resulting from the relaxation effect in the ionic atmosphere and the electrophoretic effect [75, 76]. Due to complexation of analysis, including inductance, we considered it as parasitic component and did not include in the final equivalent circuit to describe our systems.

Equivalent circuit describing obtained impedance behaviour of the polyelectrolyte/electrode interface is shown in Fig.7.2b, where R_b can be interpreted as the polyelectrolyte bulk resistance, C_g is the parasitic geometrical capacitance, R_{ct} is the charge-transfer resistance through the double layer of capacitance C_{dl} formed in the polyelectrolyte/electrode interface, W represents Warburg impedance, reflecting diffusion of the reactants to the electrode surface. This type of circuit is called Randless circuit [51] commonly used to explain electrochemical processes in the polyelectrolyte systems and their interfaces.

Parameters, derived from the described circuit of the polyelectrolyte/ electrode interface depending on salt concentration in PEO are presented in Fig.7.3. Interestingly, bulk resistance R_b (Fig.7.3a) has a minimum value at 0.05 M salt concentration implying the maximal conductivity at this salt concentration. This confirms the results of XRD study (Chapter 6) showing salt crystallization at 0.1 M salt concentration (the highest resistance), whereas higher resistance of the polyelectrolyte with 0.025 M salt concentration compared to 0.05 M salt concentration can be explained by the not sufficient amount of charge carriers. The interpreta-

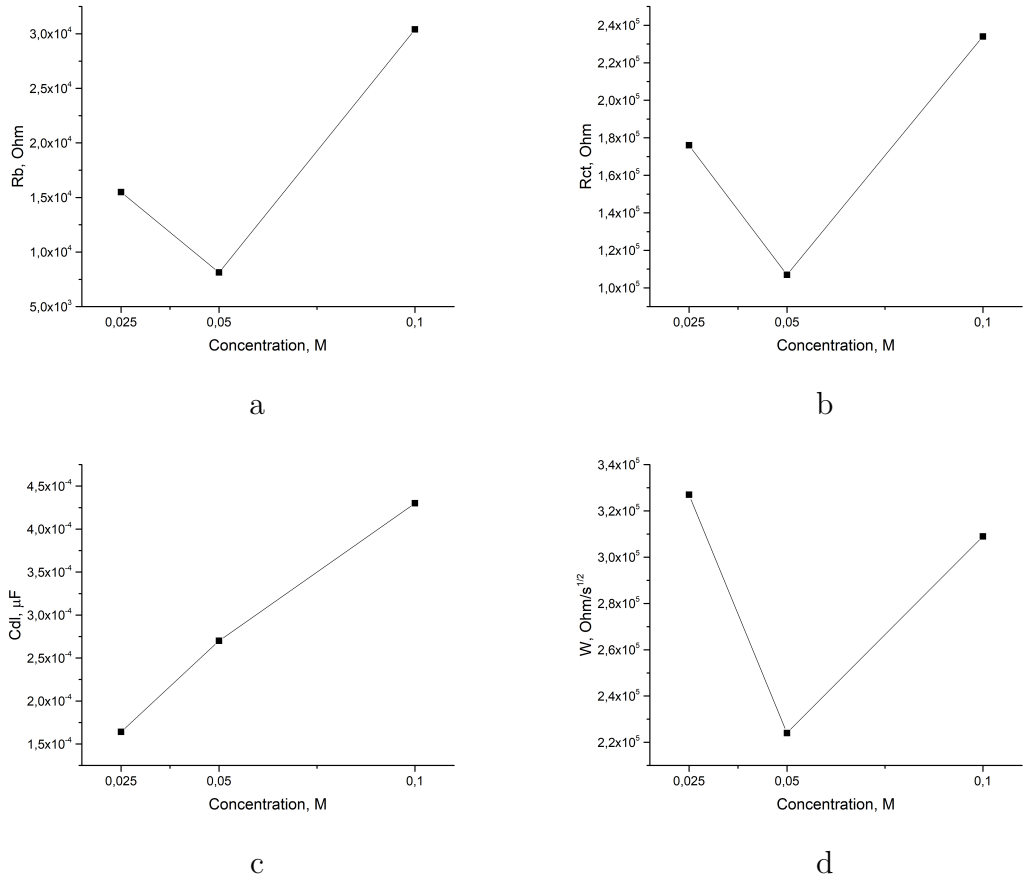

Figure 7.3. Derived parameters of the equivalent circuit, represented in Fig.7.2b of PEO-$LiClO_4$ polyelectrolyte/electrode cell: polyelectrolyte bulk resistance R_b (a), charge-transfer resistance R_{ct} (b), double layer capacitance C_{dl} (c) and Warburg impedance coefficient W (d)

tion of the dependence of the other circuit parameters on the salt concentration is rather difficult, but similar to R_b behaviour depending on salt concentration is observed also for R_{ct}.

Further, the effect of hydrochloric acid on the impedance of the PEO-$LiClO_4$ polyelectrolyte/electrode cell was studied. Impedance spectra of this cell depending on salt concentration are presented in Fig.7.4. The shape of the curves is similar to previous case: two consecutive semicircles (first one is not seen) are followed by the line, typically indicating diffusive effect. Derived equivalent circuit parameters versus salt concentration are shown in Fig.7.5. As for the acidless cells, minimal polyelectrolyte bulk resistance is found in case of 0.05 M $LiClO_4$ con-

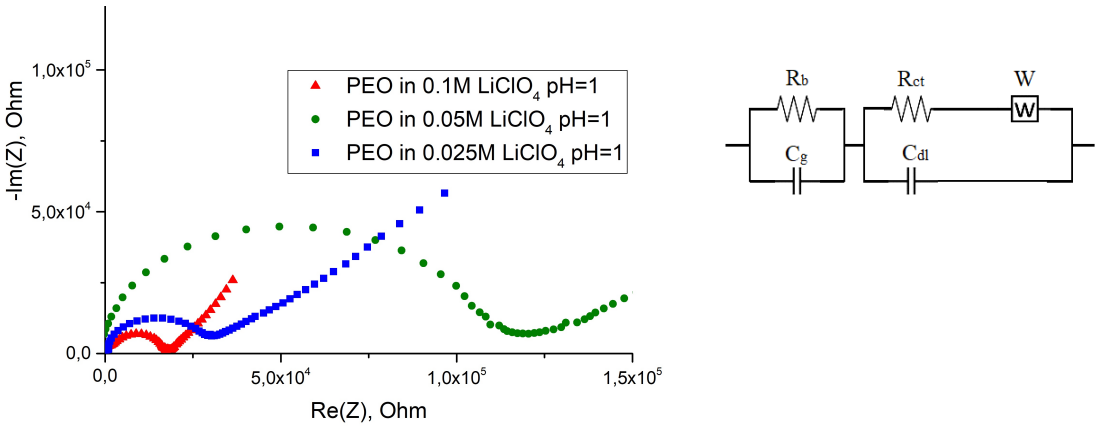

a b

Figure 7.4. Nyquist plot of prepared in pH=-1 environment PEO-$LiClO_4$ polyelectrolyte/electrode cell impedance (a) and equivalent circuit of the system (b)

centration in PEO, and maximal in case of 0.1 M salt concentration, confirming, again, the previous chapter conclusions about obstructed ionic transfer at high salt concentration when it forms aggregates. The charge transfer resistance, as well as Warburg element coefficient compared to acidless samples has completely opposite behaviour, that has not been explained in the framework of the present research.

7.3 Polyelectrolyte/PANI-coated electrode interface characterization

The cyclic voltammetry characterization of PANI-coated electrode was made in order to determine the values of the voltages necessary for transferring between the various redox states of PANI, controlling them in the EIS measurements. Obtained CV curve is shown in Fig.7.6. Two pairs of redox peaks are observed, identified, according to literature [77], as transferring between following states: at 0.12 V oxidation from leucoemeraldine base (LB) to emeraldine salt (ES), at 0.48 V oxidation to pernigraniline salt (PNS), at 0.44 V of back voltage sweep reduction to emeraldine salt and at -0.16 V reduction to leucoemeraldine base.

Nyquist plot of PEO-$LiClO_4$/PANI-coated electrode cell impedance is shown in Fig.7.7a. First semicircle appeared due to parasitic geometrical capacitance is followed by second semicircle and steep spike, degenerating into third semicircle

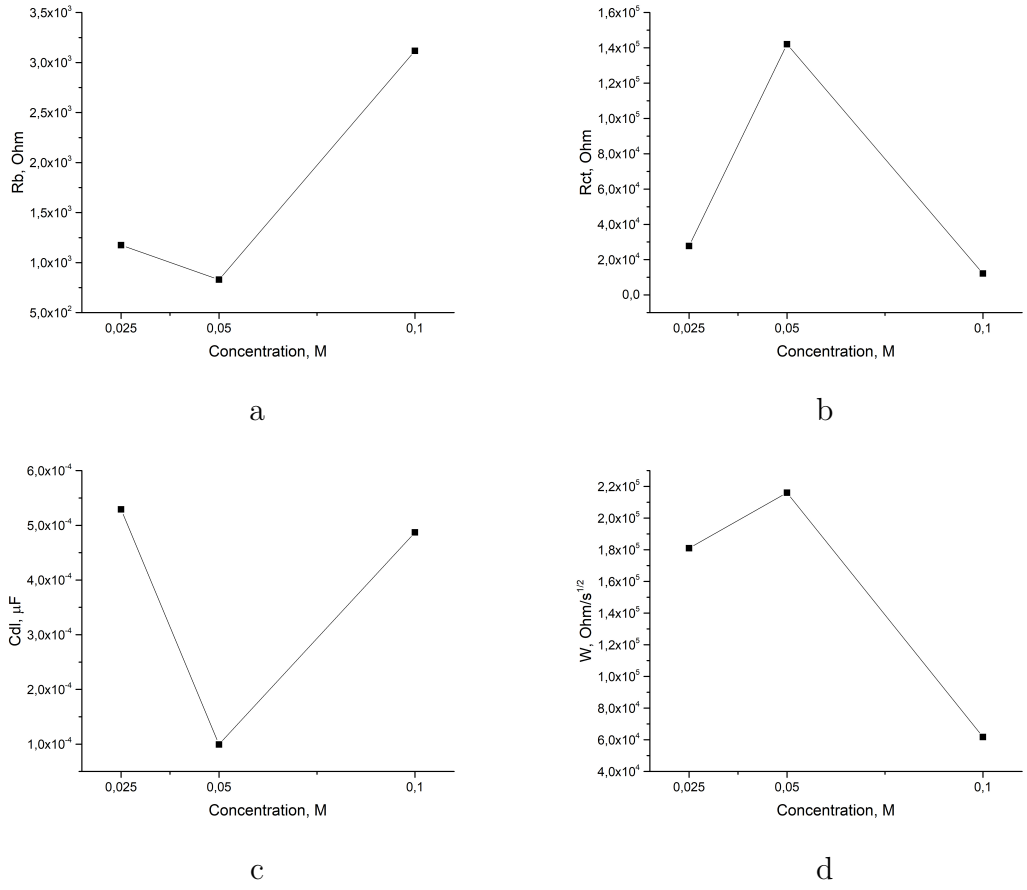

Figure 7.5. Derived parameters of the equivalent circuit, represented in Fig.7.4b of prepared in pH=-1 environment PEO-$LiClO_4$ polyelectrolyte/electrode cell: polyelectrolyte bulk resistance R_b (a), charge-transfer resistance R_{ct} (b), double layer capacitance C_{dl} (c) and Warburg impedance coefficient W (d)

at +0.8 V applied bias.

The size of second semicircle is changing according to applied voltage. The intercept of the right border of this semicircle with the Re(Z) axis reflects charge transfer resistance. The full equivalent circuit used to fit obtained impedance spectra is shown in Fig.7.7b, where, as was pointed out above, R_b is the polyelectrolyte bulk resistance, C_g is the parasitic geometrical capacitance, R_{ct} is the charge-transfer resistance and C_{dl} the double layer capacitance. In this case diffusion was taken into account by means of constant phase element, characterized by two parameters Q and n, because of the variation in the inclination angle of low-frequency part of the spectra (diffusion effect).

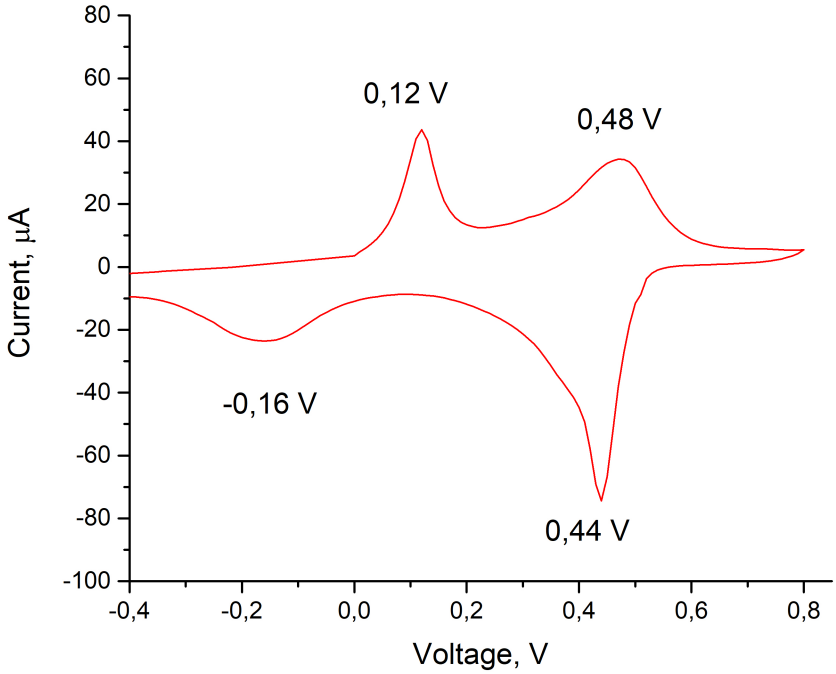

Figure 7.6. Cyclic voltammetry characterization of PANI-coated gold electrode using solid PEO-$LiClO_4$ polyelectrolyte prepared in pH=-1 acidic environment

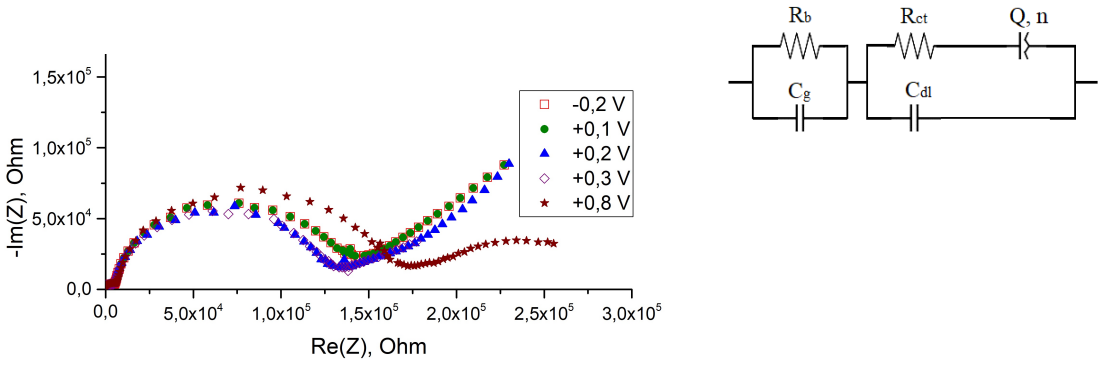

a b

Figure 7.7. Nyquist plot of PEO-$LiClO_4$ polyelectrolyte/ PANI-coated electrode cell impedance (a) and equivalent circuit of the system (b)

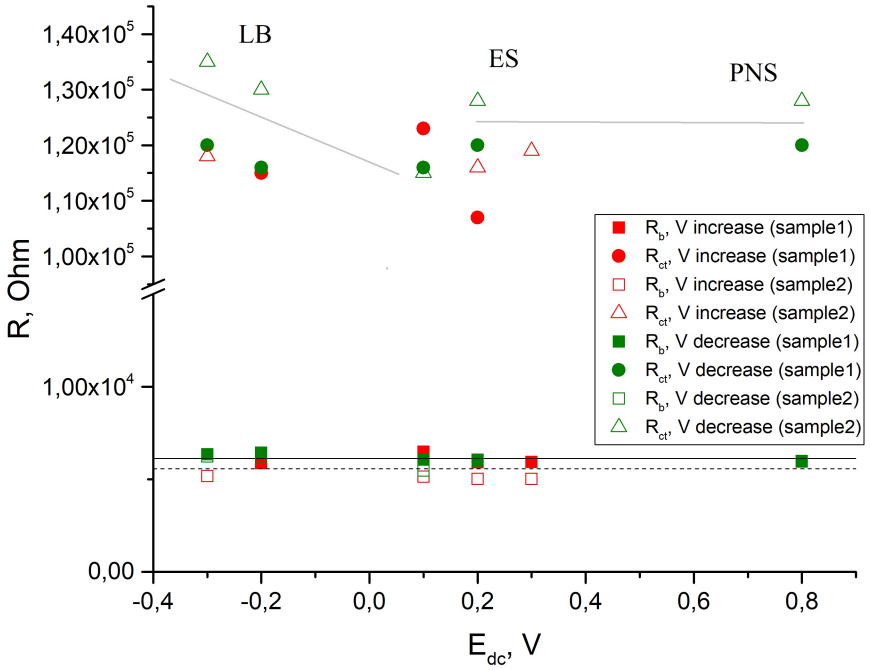

Figure 7.8. Derived parameters of the equivalent circuit, represented in Fig.7.7b of the PEO-$LiClO_4$ polyelectrolyte/PANI-coated electrode cell at different applied biases: polyelectrolyte bulk resistance R_b and charge-transfer resistance R_{ct} (b). Continuous lines are drawn to guide the eye

The polyelectrolyte bulk resistance values obtained for two independent samples and averaged over data obtained at different biases are 5578.12 and 6119.14 Ohm (Fig.7.8). The small difference in these values can be due to additional unequal doping in HCl vapours of the prepared cells after polyelectrolyte drying.

The general trend of charge resistance change as a result of applied voltages and thus transferring PANI between different redox states is shown by a lines in Fig.7.8). First, as LB form of PANI is poorly conductive, its transferring into high conductive ES is accompanied by charge transfer resistance decrease. Between ES and PNS states R_{ct} qualitative behaviour is the same, as PNS is also conductive.

Fitted values of C_{dl} were constant for all the voltage parameters, probably, due to inclusion of the CPE element to the equivalent circuit, thus, all the information on double layer and ionic diffusion to the PANI surface is contained in the CPE

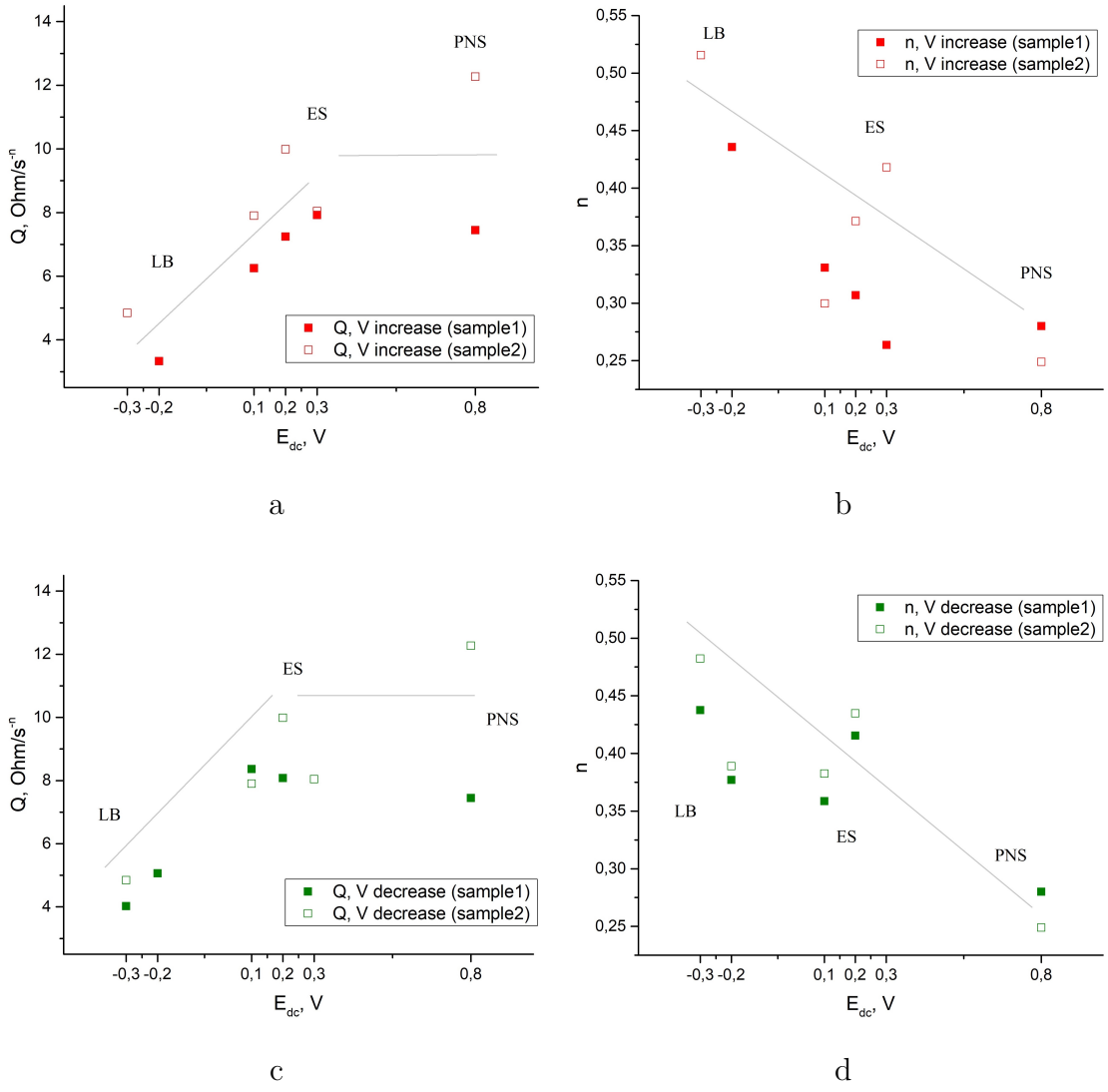

Figure 7.9. Derived parameters of constant phase element of the equivalent circuit, represented in Fig.7.7b of the PEO-$LiClO_4$ polyelectrolyte/PANI-coated electrode cell at different applied biases: Q coefficient at bias increase (a), n coefficient at bias increase (b), Q coefficient at bias decrease (c), n coefficient at bias decrease (d). Continuous lines are drawn to guide the eye

parameters (see Eq.2.28 in Section 2.4 of Chapter 2), showed in Fig.7.9 at different biases. Generally, the tendency of changing Q parameter between LB and ES states is opposite to R_{ct}, thus, probably, it reflects mostly a double layer capacitance behaviour (Fig.7.9a,c). However, the n parameter in its general trend of decreasing from 0.5 towards 0 shows transformation between Warburg impedance and purely

resistive behaviour. These results can be interpreted ambiguously, so this problem will be a subject of our future research.

7.4 Conclusions

The evaluated polyelectrolyte bulk resistance values depending on salt concentration confirms the results of the previous XRD study, showed that 0.1 M salt concentration leads to salt aggregates formation and, as a result, low ionic conductivity. The smallest studied concentration of 0.025 M, probably, does not provide sufficient amount of charge carriers, thus also gives smaller ionic conductivity compared to 0.05 M salt concentration.

Chapter 8

Optimized Organic memristive device

Taking into account the results obtained in the previous chapters, the present one discusses the results of a study of the effect of salt concentration in polyelectrolyte on the kinetics of the organic memristive device.

8.1 Experimental details

Organic memristive devices were fabricated as described in Section 2.1 of Chapter 2. Three different salt concentrations were used to prepare polyelectrolyte solutions – 0.1 M, 0.05 M and 0.025 M. For every salt concentration three series of the devices were assembled to provide reliable results.

Electrical measurements were performed using Keithley 236 and Keithley 6514 electrometers, former was used simultaneously as a voltage source and total current meter, whereas the latter was used as ionic current meter.

Voltage sweep of current-voltage characterization was increased from 0 V with a step of 0.1 V up to +1 V, and decreased up to -0.5 V at back sweep. The delay at every voltage value was 60 s, to provide enough time for the electrochemical processes. For kinetic characterization, first 0.8 V was applied for 60-90 min, and then -0.2 V for 10-20 min.

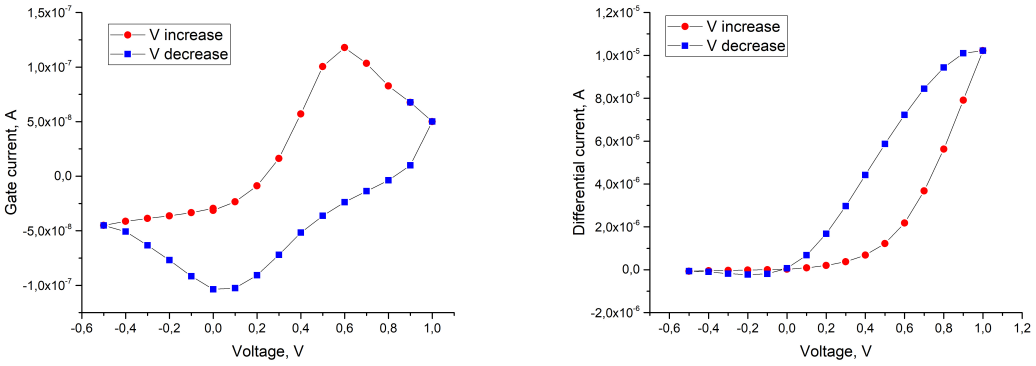

a b

Figure 8.1. Typical current-voltage plots of the organic memristive device, fabricated using PEO-$LiClO_4$ polyelectrolyte with 0.05 M salt concentration for ionic (gate) (a) and electronic (differential) (b) currents

8.2 Current-voltage characterization

As it was mentioned in the Section 2.1.2 of Chapter 2, the final state of the OMD is evaluated measuring current at voltage sweep. Usually, the total current between source and drain electrodes is measured. Although, the control of ionic current is necessary to understand the functioning mechanism of OMD, therefore gate current is measured along with current between drain and source.

Typical current-voltage plots of OMD, fabricated using the polyelectrolyte containing 0.05 M $LiClO_4$ concentration, for ionic and electronic currents (the difference between total and ionic currents) are shown in Fig.8.1.

Initially, the active zone was at insulating state (right branch of Eq.1.1), thus electronic current has a low value up to +0.3 V. The peak around +0.6 V in ionic current-voltage plot indicates maximal concentration of anions near the PANI active zone, and its further decrease expressed in ionic current decrease for higher voltages. At the same time differential current increases, indicating PANI oxidation, or, in other words, the transition to conducting state (left branch of Eq.1.1). Chlorine ions compensate PANI, positively charged in its conducting state, while lithium ions move into negatively charged polyelectrolyte volume, formed by $ClO4^{-}$ ions. Further voltage increase leads to significant electronic current grow up to maximal value at +1 V. At back voltage sweep linear decrease of differential current is observed up to +0.1 V, that in ionic current-voltage plot corresponds to

minima, meaning PANI reduction and transition to insulating state. As a result, low electronic current values are observed at negative voltages. The most important fact is that this switch provides a difference in resistivity between the fully oxidized and reduced PANI layer in the active zone by up to four orders of magnitude. Such type of resistivity switching is the most significant characteristic of OMD.

8.3 Kinetic characterization

The response speed of the device is expressed in its kinetic behaviour. Typical response of the device to the application of constant voltage is presented in Fig.8.2 as an electronic current versus time plot. It is seen that, after the application of a positive potential of +0.8V, a slow increase of current up to a saturated value is observed, whereas at the negative potential of -0.2V the drop of the current to a negative value and the subsequent decay to zero occur significantly faster. Such different behaviour of OMD at oxidation and reduction arises from different initial potential distribution in the active zone of the device [78]. Briefly, in the case of oxidation, when the potential applied at the drain electrode is abruptly changed from -0.2 V (initializing potential) to +0.8 V, in order to convert PANI into conductive state, time is needed for PANI layer to reach the oxidation potential. Such a process, in fact, is controlled by the ion diffusion through PEO. At the beginning of the conversion process, only the part of the active zone located more closely to the drain electrode resulted at a potential value higher than the oxidation potential (that is about of +0.3 V). When in all the active zone of the PANI layer the potential overcomes the oxidation voltage, the conductivity conversion of PANI can be completed. Thus, the oxidation occurs gradually from the part of the active zone that is closer to the drain electrode, towards the middle of the active zone below the gate, and then, less important, towards the source electrode. Reduction process, instead, takes places when PANI is in conducting form (reduction potential of PANI is +0.1V), therefore, when -0.2 V is applied, the entire active zone reaches at once the reduction potential (becomes rapidly a nearly equipotential surface), thus the reduction reaction occurs simultaneously in the whole active area. More interesting is the fact that the speed of current saturation for the above potentials is

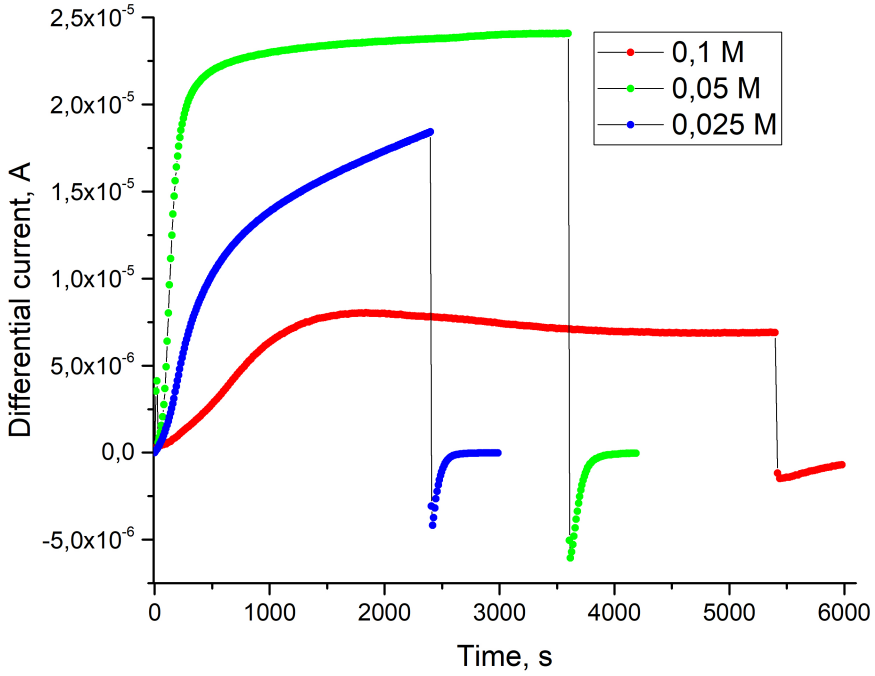

Figure 8.2. Kinetics of organic memristive device at +0.8 V and -0.2 V for the memristors based on PEO prepared with 0.1 M (red), 0.05 M (green) and 0.025 M (blue) $LiClO_4$ water solutions

different for the devices with different levels of polyelectrolyte doping with lithium salt.

In order to understand this dependence of OMD kinetics on lithium salt concentration in PEO, the behaviour of ionic currents at constant voltages was examined.

Ionic currents, registered at +0.8 V and -0.2 V respectively for OMDs, composed using polyelectrolyte with different salt concentrations are shown in Fig.8.3.

As the potential is abruptly set at +0.8 V, first, ionic current increases up to a maximal value, and then slowly drops to almost zero. This is consistent with the above picture, indicating that immediately after the voltage setting, only the part of the active layer located near the drain contact is at the required potential for the oxidation process. Then, ions start to diffuse toward this part crossing PEO, so beginning the oxidation process. During time, a wider and wider part of the active layer overcomes the oxidation voltage and further ions enter to PANI for

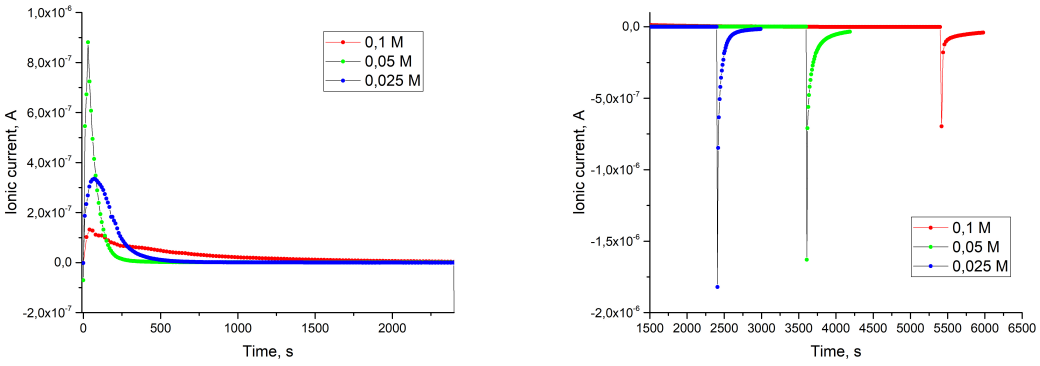

a b

Figure 8.3. Ionic currents, measured at applied constant voltage +0.8 V (a) and -0.2 V(b) for organic memristive devices, composed using polyelectrolytes with different salt concentration

a progressive conductivity conversion. Then ionic current firstly increases during time. When the oxidation process is becoming complete in the full PANI-layer thickness, the ionic current goes down to zero, whereas, at the same time, the total current, saturates at its maximum value (as discussed above), corresponding to the high conductivity of PANI. The assessment of the potential at the PANI surface is comparable to the charging process of a capacitor, however, because the initial current is zero, and then it increases up to a maximal value in a finite time, the equivalent circuit describing the processes is more complex than a simple RC one.

When the -0.2 V potential is applied, the conductive PANI layer behaves as a nearly equipotential surface, therefore, the reduction process starts rapidly in the whole area, so that the initial rising up of the lithium ion current is very fast. Such current fluxes from PANI to the gate electrode as in a process of a capacitor discharge, and then decrease to zero during time. The observed difference in the decay times of the current during oxidation and reduction processes (curves of the same colour in Fig.8.2 and 8.3) is expected to be related to the resistance (the conductivity state) of PANI, as for a decay times $\tau = RC$ in charge-discharge processes of a capacitor. In fact, the slower charge process takes place when PANI is poorly conductive, the reverse is true for the faster discharge process. However, also the doping level of PEO plays a significant role, as highlighted by comparing

the behaviour of devices with differently-doped PEO layers (see green and blue curves in Fig.8.2 and 8.3). Both charge and discharge time constants are increased in the device where PEO is less conductive. A separated discussion is needed for the device corresponding to the red curve, which will be discussed below.

Considering for simplicity an equivalent RC circuit, both charge-discharge processes of the capacitor are controlled by the redox reaction (Eq.1.1 of Section 1.1 of Chapter 1), but are realized by ionic charge carriers involved in the reaction. This underlines the importance of ionic species presented in the system. The decay to zero of the ionic currents both in the charge and discharge processes was then analysed in a simple model, using the exponential function $\propto \exp(-t/\tau)$, where τ is a characteristic time constant.

Fitted values of τ for the ionic current, related to capacitor charging at +0.8 V, applied to OMD with different salt content of the polyelectrolyte is shown in Fig.8.4a. The faster charging process corresponds to 0.05 M salt concentration, while the maximal 0.1 M salt concentration shows the slowest charging. When -0.2 V potential is applied to a device, two different processes, characterized by two time constants are observed Fig.8.4b). The faster process follows the same concentration dependence as the charging process, i.e. the lowest time constant is in case of 0.05 M salt concentration and the highest for 0.1 M salt concentration in polyelectrolyte. These time constants represent the discharging time of the capacitor. The second process follows linear behaviour - the less salt content in polyelectrolyte, the faster is exponential saturation.

Interestingly, peak values and ionic current decay rates are different for the devices with different salt concentration of polyelectrolytes, however, the total passed ionic charge, that is an integral of current with respect to time $\int_0^t I(t)dt$, is almost the same for all salt concentrations in case of oxidation and reduction (Table 8.1).

Table 8.1. Total passed ionic charges for organic memristive devices, composed using polyelectrolytes with different salt concentration

Salt concentration	**0.025 M**	**0.05 M**	**0.1 M**
Total passed ionic charge at +0.8 V	7.04×10^{-5}	6.53×10^{-5}	6.85×10^{-5}
Total passed ionic charge at -0.2 V	1.19×10^{-4}	1.74×10^{-4}	1.22×10^{-4}

Therefore, this results suggest that OMD composed using PEO doped by

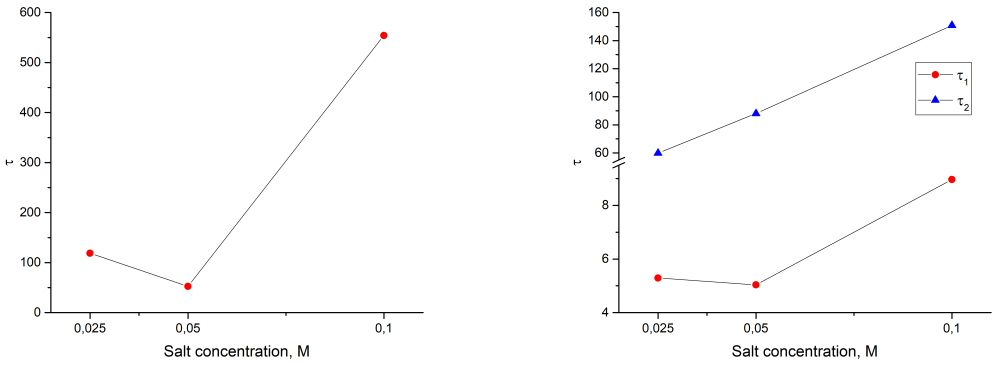

a b

Figure 8.4. Time constants of a capacitor charge processes, obtained by fitting ionic currents at constant +0.8 V (a) and -0.2 V (b) voltages, applied to organic memristive devices, composed using polyelectrolytes with different salt concentration

0.05 M salt concentration provides faster capacitor charging-discharging, and faster OMD kinetics, because the total ionic flux towards and backwards the PANI-polyelectrolyte interface is controlled by redox reactions. This is clearly seen from time constants of electronic current (For example, in case of oxidation at +0.8 V in Fig.8.5).

Therefore, analysis of ionic currents associated with the processes of capacitors charging-discharging, as well as electron currents in OMD with different content of salt in PEO-based solid polyelectrolyte, showed the possibility of improving the response speed of the device.

Standard salt concentration of 0.1 M has shown the slowest kinetics of the device. It has been shown that such result is related to obstructed ionic transport due to formation of salt aggregates, as the result of high salt concentration. The effect of salt association at applied to OMD fabricated by standard protocol +0.6 V was observed by Raman spectroscopy [79]. The fastest kinetics correspond to 0.05 M salt concentration in PEO, while 0.025 M salt concentration gives intermediate results. For this case salt aggregation was not observed, and slower kinetics of the smallest salt concentration is related to insufficient number of charge carriers.

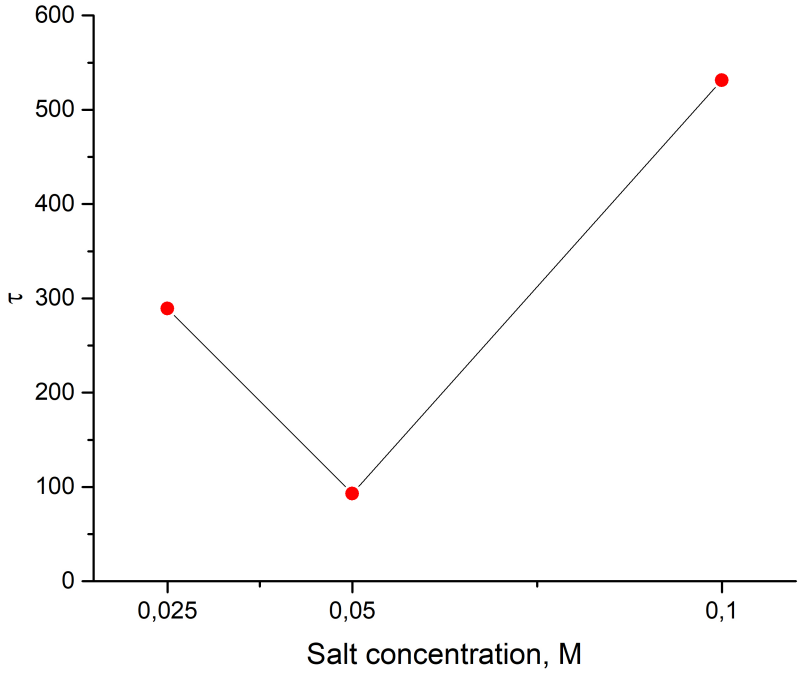

Figure 8.5. Time constants of electronic current at +0.8 V depending on salt concentration of the polyelectrolyte

8.4 Conclusions

The possibility of increasing the OMD response speed by optimizing the composition of the polyelectrolyte using different doping salt contents was demonstrated. Analyzing electronic currents, measured at constant voltages, we found, that standard salt concentration of the polyelectrolyte gives the slowest kinetics of the device, while it can be optimized using halved concentration. This behaviour is the result of polyelectrolyte composition - at high concentration of salt tends to form aggregates, thus ionic transport is obstructed. Even if the lowest salt concentration of the investigated range can prevent the formation of the aggregates, it does not provide the required amount of charge carriers, leading to slow OMD kinetics.

Chapter 9

Conclusions

In the present research combined theoretical and experimental methods were used to study poly(ethylene oxide) - lithium perchlorate solid polymer electrolyte, that is one of a key material of the organic memristive device. Using NMR diffusometry, allowing to access individual lithium hopings, we have observed different lithium dynamics in liquid and dried polyelectrolytes. Generally, the structure of both samples was found to be quite complex. The different diffusing phases in the case of dried sample were detected, that can indicate the presence of dissociated and aggregated salt in the sample.

MD simulations have shown that salt concentration in PEO, used in the standard OMD composition, indeed is too high that leads to salt aggregation, whereas the system with a half of this concentration does not show salt aggregates formation. Calculated self-diffusion coefficients of former system has almost twice less self-diffusion coefficient than the latter one. Effect of water on the system, can, in principle, reduce the interaction strength between cations and anions. This fact results in the enhancement of the dissolution of the salt in the polymer matrix. And consequently, water prevents the formation of salt aggregates. Calculated self-diffusion coefficients are in a good agreement with the measured data. The growth of the self-diffusion coefficients with an increase of water content in the system is associated with both the formation of more free volume and salt aggregation decrease.

This results underline the importance of the hydration level control towards reproducible ionic transport properties in PEO. In long-term operation of OMD, the

stable polyelectrolyte structure, and therefore stable ionic conductivity, provides the endurance of OMD. XRD studies have shown a large fraction of salt aggregates in the sample prepared using standard salt concentration and dried for a month in argon atmosphere. This salt aggregation, although in a less fraction, appears even in a sample dried overnight at ambient environment. This results point out the poor stability of the polyelectrolyte structure, and thus, difficulty in providing OMD endurance.

The decreased salt concentration in the polyelectrolytes dried at standard conditions did not show salt crystallization. However, crystallization of PEO itself decreases amorphous polyelectrolyte phase responsible for ionic transport. Moreover, the general effect of hydrochloric acid, usually added to the polyelectrolyte to provide acidic environment for redox reactions, on the structure of the polyelectrolytes was found to result in the total increase of the fraction of crystallites.

Electrochemical impedance spectroscopy method used to characterize polyelectrolyte/ electrode electrochemical behaviour confirmed XRD results: the standard polyelectrolyte composition gives the smallest ionic conductivity values due to obstructed ionic transport and aggregates formation, whereas the highest conductivity is in the case of halved of standard concentration. The smallest studied concentration, probably, does not provide sufficient amount of charge carriers, thus it also gives lower ionic conductivity compared to previous case. The study of the polyelectrolyte/PANI interface have shown very complex electrochemical behaviour due to changing internal resistance of PANI layer. The solving of this problem will require additional studies.

Finally, we have demonstrated, that increased ionic conductivity in the PEO-based polyelectrolyte, is observed when it is prepared using 0.05M lithium salt concentration. In this case we have also registered faster kinetics of the resistance switching of organic memristive device, comparing to ones, fabricated using standard polyelectrolyte composition of 0.1M salt concentration, as well as 0.025M salt concentration. This sufficiently increased the response speed of the device.

Bibliography

[1] Strukov, D. B., G. S. Snider, D. R. Stewart, and R. S. Williams (2008) "The missing memristor found," *nature*, **453**(7191), p. 80.

[2] Chua, L. (1971) "Memristor-the missing circuit element," *IEEE Transactions on circuit theory*, **18**(5), pp. 507–519.

[3] Erokhin, V., T. Berzina, and M. P. Fontana (2005) "Hybrid electronic device based on polyaniline-polyethyleneoxide junction," *Journal of Applied Physics*, **97**(6), p. 064501.

[4] Erokhin, V., G. D. Howard, and A. Adamatzky (2012) "Organic memristor devices for logic elements with memory," *International Journal of Bifurcation and Chaos*, **22**(11), p. 1250283.

[5] Erokhin, V., T. Berzina, P. Camorani, A. Smerieri, D. Vavoulis, J. Feng, and M. P. Fontana (2011) "Material memristive device circuits with synaptic plasticity: learning and memory," *BioNanoScience*, **1**(1-2), pp. 24–30.

[6] Demin, V., V. Erokhin, A. Emelyanov, S. Battistoni, G. Baldi, S. Iannotta, P. Kashkarov, and M. Kovalchuk (2015) "Hardware elementary perceptron based on polyaniline memristive devices," *Organic Electronics*, **25**, pp. 16–20.

[7] Emelyanov, A., D. Lapkin, V. Demin, V. Erokhin, S. Battistoni, G. Baldi, A. Dimonte, A. Korovin, S. Iannotta, P. Kashkarov, et al. (2016) "First steps towards the realization of a double layer perceptron based on organic memristive devices," *Aip Advances*, **6**(11), p. 111301.

[8] Erokhina, S., V. Sorokin, and V. Erokhin (2015) "Polyaniline-based organic memristive device fabricated by layer-by-layer deposition technique," *Electronic Materials Letters*, **11**(5), pp. 801–805.

[9] Heeger, A. J. (2001) "Nobel Lecture: Semiconducting and metallic polymers: The fourth generation of polymeric materials," *Reviews of Modern Physics*, **73**(3), p. 681.

[10] Kang, E., K. Neoh, and K. Tan (1998) "Polyaniline: a polymer with many interesting intrinsic redox states," *Progress in polymer science*, **23**(2), pp. 277–324.

[11] Berzina, T., S. Erokhina, P. Camorani, O. Konovalov, V. Erokhin, and M. Fontana (2009) "Electrochemical control of the conductivity in an organic memristor: a time-resolved X-ray fluorescence study of ionic drift as a function of the applied voltage," *ACS Applied materials & interfaces*, **1**(10), pp. 2115–2118.

[12] Stephan, A. M. (2006) "Review on gel polymer electrolytes for lithium batteries," *European polymer journal*, **42**(1), pp. 21–42.

[13] Xue, Z., D. He, and X. Xie (2015) "Poly(ethylene oxide)-based electrolytes for lithium-ion batteries," *Journal of Materials Chemistry A*, **3**(38), pp. 19218–19253.

[14] Fenton, D. (1973) "Complexes of alkali metal ions with poly (ethylene oxide)," *polymer*, **14**, p. 589.

[15] Fullerton-Shirey, S. K. and J. K. Maranas (2009) "Effect of LiClO4 on the structure and mobility of PEO-based solid polymer electrolytes," *Macromolecules*, **42**(6), pp. 2142–2156.

[16] Bandara, L., M. Dissanayake, and B.-E. Mellander (1998) "Ionic conductivity of plasticized (PEO)-LiCF 3 SO 3 electrolytes," *Electrochimica Acta*, **43**(10), pp. 1447–1451.

[17] Kim, Y.-T. and E. S. Smotkin (2002) "The effect of plasticizers on transport and electrochemical properties of PEO-based electrolytes for lithium rechargeable batteries," *Solid State Ionics*, **149**(1), pp. 29–37.

[18] Vignarooban, K., M. Dissanayake, I. Albinsson, and B.-E. Mellander (2014) "Effect of TiO 2 nano-filler and EC plasticizer on electrical and thermal properties of poly (ethylene oxide)(PEO) based solid polymer electrolytes," *Solid State Ionics*, **266**, pp. 25–28.

[19] Fergus, J. W. (2010) "Ceramic and polymeric solid electrolytes for lithium-ion batteries," *Journal of Power Sources*, **195**(15), pp. 4554–4569.

[20] Srivastava, S., J. L. Schaefer, Z. Yang, Z. Tu, and L. A. Archer (2014) "25th anniversary article: polymer–particle composites: phase stability and applications in electrochemical energy storage," *Advanced Materials*, **26**(2), pp. 201–234.

[21] Krawiec, W., L. Scanlon, J. Fellner, R. Vaia, S. Vasudevan, and E. Giannelis (1995) "Polymer nanocomposites: a new strategy for synthesizing solid electrolytes for rechargeable lithium batteries," *Journal of Power Sources*, **54**(2), pp. 310–315.

[22] Gadjourova, Z., Y. G. Andreev, D. P. Tunstall, and P. G. Bruce (2001) "Ionic conductivity in crystalline polymer electrolytes," *Nature*, **412**(6846), pp. 520–523.

[23] Gadjourova, Z., D. Martín y Marero, K. H. Andersen, Y. G. Andreev, and P. G. Bruce (2001) "Structures of the polymer electrolyte complexes PEO6: LiXF6 (X= P, Sb), determined from neutron powder diffraction data," *Chemistry of materials*, **13**(4), pp. 1282–1285.

[24] Borodin, O. and G. D. Smith (2006) "Mechanism of ion transport in amorphous poly (ethylene oxide)/LiTFSI from molecular dynamics simulations," *Macromolecules*, **39**(4), pp. 1620–1629.

[25] Andreev, Y., P. Lightfoot, and P. Bruce (1996) "Structure of the polymer electrolyte poly (ethylene oxide) 3: LiN (SO2CF3) 2 determined by powder diffraction using a powerful Monte Carlo approach," *Chemical Communications*, (18), pp. 2169–2170.

[26] Marzantowicz, M., J. Dygas, F. Krok, Z. Florjańczyk, and E. Zygadło-Monikowska (2007) "Influence of crystalline complexes on electrical properties of PEO: LiTFSI electrolyte," *Electrochimica Acta*, **53**(4), pp. 1518–1526.

[27] Martin-Litas, I., Y. G. Andreev, and P. G. Bruce (2002) "Ab initio structure solution of the polymer electrolyte poly (ethylene oxide) 3: LiAsF6," *Chemistry of materials*, **14**(5), pp. 2166–2170.

[28] Andreev, Y. G., V. Seneviratne, M. Khan, W. A. Henderson, R. E. Frech, and P. G. Bruce (2005) "Crystal Structures of Poly (ethylene oxide) 3: LiBF4 and (Diglyme) n: LiBF4 (n= 1, 2)," *Chemistry of materials*, **17**(4), pp. 767–772.

[29] Robitaille, C. and D. Fauteux (1986) "Phase Diagrams and Conductivity Characterization of Some PEO-LiX Electrolytes," *Journal of The Electrochemical Society*, **133**(2), pp. 315–325.

[30] Vallée, A., S. Besner, and J. Prud'Homme (1992) "Comparative study of Poly(ethylene oxide) electrolytes made with LiN (CF 3 SO 2) 2, LiCF 3 SO 3 and LiClO 4: Thermal properties and conductivity behaviour," *Electrochimica acta*, **37**(9), pp. 1579–1583.

[31] Mao, G., M.-L. Saboungi, D. Price, Y. Badyal, and H. Fischer (2001) "Lithium environment in PEO-LiClO4 polymer electrolyte," *EPL (Europhysics Letters)*, **54**(3), p. 347.

[32] Henderson, W. A. and S. Passerini (2003) "Ionic conductivity in crystalline–amorphous polymer electrolytes–P (EO) 6: LiX phases," *Electrochemistry communications*, **5**(7), pp. 575–578.

[33] Lauenstein, A., A. Johansson, and J. Tegenfeldt (1994) "Water Absorption of the Polymer Electrolyte Systems Pb (CF 3 SO 3) 2 PEO n and Zn (CF 3 SO 3) 2 PEO n," *Journal of the Electrochemical Society*, **141**(7), pp. 1819–1823.

[34] DeLongchamp, D. M. and P. T. Hammond (2004) "Highly ion conductive poly (ethylene oxide)-based solid polymer electrolytes from hydrogen bonding layer-by-layer assembly," *Langmuir*, **20**(13), pp. 5403–5411.

[35] Huq, R., G. Chiodelli, P. Ferloni, A. Magistris, and G. Farrington (1987) "Poly (ethylene oxide) Complexes of Lead Halides New Polymeric Conductors of Pb2+," *Journal of the Electrochemical Society*, **134**(2), pp. 364–369.

[36] Hashmi, S. (1998) "Influence of water absorption on poly–ethylene oxide-based polymer electrolytes complexed with ammonium, sodium and magnesium perchlorates," *Journal of materials science*, **33**(4), pp. 989–993.

[37] Johansson, A., A. Lauenstein, and J. Tegenfeldt (1995) "Effect of water on diffusion and ionic conductivity in PEG and LiCF3SO3PEG10," *The Journal of Physical Chemistry*, **99**(16), pp. 6163–6166.

[38] Donoso, J., M. Cavalcante, T. Bonagamba, O. Nascimento, and H. Panepucci (1995) "Magnetic resonance study of water absorption in some peo-lithium salt polymer electrolytes," *Electrochimica acta*, **40**(13-14), pp. 2357–2360.

[39] Wendsjö, Å., J. O. Thomas, and J. Lindgren (1993) "Infra-red and X-ray diffraction study of the hydration process in the polymer electrolyte system M (CF3SO3) 2PEOn for M= Pb, Zn and Ni," *Polymer*, **34**(11), pp. 2243–2249.

[40] Tongraar, A., K. R. Liedl, and B. M. Rode (1998) "The hydration shell structure of Li+ investigated by Born–Oppenheimer ab initio QM/MM dynamics," *Chemical physics letters*, **286**(1-2), pp. 56–64.

[41] Pye, C. C., W. Rudolph, and R. A. Poirier (1996) "An ab initio investigation of lithium ion hydration," *The Journal of Physical Chemistry*, **100**(2), pp. 601–605.

[42] Zhang, Z., M. Ohl, S. O. Diallo, N. H. Jalarvo, K. Hong, Y. Han, G. S. Smith, and C. Do (2015) "Dynamics of Water Associated with Lithium Ions Distributed in Polyethylene Oxide," *Physical review letters*, **115**(19), p. 198301.

[43] Epstein, A., J. Ginder, F. Zuo, R. Bigelow, H.-S. Woo, D. Tanner, A. Richter, W.-S. Huang, and A. MacDiarmid (1987) "Insulator-to-metal transition in polyaniline," *Synthetic Metals*, **18**(1-3), pp. 303–309.

[44] MacDiarmid, A., J. Chiang, A. Richter, Epstein, and AJ (1987) "Polyaniline: a new concept in conducting polymers," *Synthetic Metals*, **18**(1-3), pp. 285–290.

[45] Duer, M. J. (2004) *Introduction to solid-state NMR spectroscopy*, Blackwell Oxford.

[46] Stejskal, E. O. and J. E. Tanner (1965) "Spin diffusion measurements: spin echoes in the presence of a time-dependent field gradient," *The journal of chemical physics*, **42**(1), pp. 288–292.

[47] Tanner, J. E. (1970) "Use of the stimulated echo in NMR diffusion studies," *The Journal of Chemical Physics*, **52**(5), pp. 2523–2526.

[48] Rietveld, H. (1969) "A profile refinement method for nuclear and magnetic structures," *Journal of applied Crystallography*, **2**(2), pp. 65–71.

[49] Barsoukov, E. and J. R. Macdonald (2018) *Impedance spectroscopy: theory, experiment, and applications*, John Wiley & Sons.

[50] Lasia, A. (2002) "Electrochemical impedance spectroscopy and its applications," in *Modern aspects of electrochemistry*, Springer, pp. 143–248.

[51] Randles, J. E. B. (1947) "Kinetics of rapid electrode reactions," *Discussions of the faraday society*, **1**, pp. 11–19.

[52] Verlet, L. (1967) "Computer" experiments" on classical fluids. I. Thermodynamical properties of Lennard-Jones molecules," *Physical review*, **159**(1), p. 98.

[53] Hoover, W. G. (1985) "Canonical dynamics: equilibrium phase-space distributions," *Physical review A*, **31**(3), p. 1695.

[54] Nosé, S. (1984) "A unified formulation of the constant temperature molecular dynamics methods," *The Journal of chemical physics*, **81**(1), pp. 511–519.

[55] ——— (1984) "A molecular dynamics method for simulations in the canonical ensemble," *Molecular physics*, **52**(2), pp. 255–268.

[56] Balinov, B., B. Jonsson, P. Linse, and O. Soderman (1993) "The NMR self-diffusion method applied to restricted diffusion. Simulation of echo attenuation from molecules in spheres and between planes," *Journal of Magnetic Resonance, Series A*, **104**(1), pp. 17–25.

[57] Valiullin, R. and V. Skirda (2001) "Time dependent self-diffusion coefficient of molecules in porous media," *The Journal of Chemical Physics*, **114**(1), pp. 452–458.

[58] Hayamizu, K., E. Akiba, T. Bando, Y. Aihara, and W. S. Price (2003) "NMR studies on poly (ethylene oxide)-based polymer electrolytes with different cross-linking doped with LiN (SO2CF3) 2. Restricted diffusion of the polymer and lithium ion and time-dependent diffusion of the anion," *Macromolecules*, **36**(8), pp. 2785–2792.

[59] Huynh, T.-V. (2015) *NMR study of lithium mobility in polymer electrolytes*, Ph.D. thesis, Université d'Orléans.

[60] Plimpton, S. (1995) "Fast parallel algorithms for short-range molecular dynamics," *Journal of computational physics*, **117**(1), pp. 1–19.

[61] LAMMPS.
URL `http://lammps.sandia.gov`

[62] Design, M. (2006), "MEDEA software, Version 2.2.1. Materials Design," .
URL `https://www.materialsdesign.com/`

[63] van Zon, A., B. Mos, P. Verkerk, and S. de Leeuw (2001) "On the dynamics of PEO-NaI polymer electrolytes," *Electrochimica acta*, **46**(10), pp. 1717–1721.

[64] Frenkel, D. and B. Smit (2002) *Understanding molecular simulation: from algorithms to applications*, vol. 1, Elsevier (formerly published by Academic Press).

[65] Luty, B. A. and W. F. van Gunsteren (1996) "Calculating electrostatic interactions using the particle-particle particle-mesh method with nonperiodic long-range interactions," *The Journal of Physical Chemistry*, **100**(7), pp. 2581–2587.

[66] Annis, B., O. Borodin, G. D. Smith, C. Benmore, A. Soper, and J. Londono (2001) "The structure of a poly(ethylene oxide) melt from neutron scattering and molecular dynamics simulations," *The Journal of Chemical Physics*, **115**(23), pp. 10998–11003.

[67] Sears, V. F. (1992) "Neutron scattering lengths and cross sections," *Neutron news*, **3**(3), pp. 26–37.

[68] Siqueira, L. J. and M. C. Ribeiro (2005) "Molecular dynamics simulation of the polymer electrolyte poly (ethylene oxide)/LiClO4. I. Structural properties," *Journal of Chemical Physics*, **122**(19), p. 4911.

[69] Mao, G., M.-L. Saboungi, D. L. Price, M. B. Armand, and W. Howells (2000) "Structure of liquid PEO-LiTFSI electrolyte," *Physical review letters*, **84**(24), p. 5536.

[70] Agrawal, R. and G. Pandey (2008) "Solid polymer electrolytes: materials designing and all-solid-state battery applications: an overview," *Journal of Physics D: Applied Physics*, **41**(22), p. 223001.

[71] Van Krevelen, D. W. and K. Te Nijenhuis (2009) *Properties of polymers: their correlation with chemical structure; their numerical estimation and prediction from additive group contributions*, Elsevier.

[72] Toby, B. H. and R. B. Von Dreele (2013) "GSAS-II: the genesis of a modern open-source all purpose crystallography software package," *Journal of Applied Crystallography*, **46**(2), pp. 544–549.

[73] Gurusiddappa, J., W. Madhuri, R. P. Suvarna, and K. P. Dasan (2016) "Studies on the morphology and conductivity of PEO/LiClO4," *Materials Today: Proceedings*, **3**(6), pp. 1451–1459.

[74] Simmons, J. P. and C. D. Ropp (1928) "THE SYSTEM LITHIUM PERCHLORATEWATER," *Journal of the American Chemical Society*, **50**(6), pp. 1650–1653.

[75] Atkins, P. W., J. De Paula, et al. (2009) *Elements of physical chemistry/Peter Atkins, Julio de Paula.*

[76] Bardos, A., R. N. Zare, and K. Markides (2005) "Inductive behavior of electrolytes in AC conductance measurements," *Chemical physics letters*, **402**(1-3), pp. 274–278.

[77] Dabke, R., A. Dhanabalan, S. Major, S. Talwar, R. Lal, and A. Contractor (1998) "Electrochemistry of polyaniline Langmuir–Blodgett films," *Thin Solid Films*, **335**(1-2), pp. 203–208.

[78] Erokhin, V. and M. Fontana (2011) "Thin film electrochemical memristive systems for bio-inspired computation," *Journal of Computational and Theoretical Nanoscience*, **8**(3), pp. 313–330.

[79] Berzina, T., V. Erokhin, and M. Fontana (2007) "Spectroscopic investigation of an electrochemically controlled conducting polymer-solid electrolyte junction," *Journal of applied physics*, **101**(2), p. 024501.

Acknowledgments

I would like to express my deep and sincere gratitude to my supervisor, Dr. Viktor Erokhin, for his guidelines, patience, constant attention and coonfidence in me. I want to thank my second supervisor Prof. Dmitrii Tayurskii from Kazan Federal University for his understanding and help at all stages of my work. I also want to thank my scientific co-tutor Dr. Silvia Battistoni for her life philosophy, for encouraging me to be better myself and to ask the right questions.

I would like to express heartfelt thanks to Dr. Tatiana Berzina for her tireless support in various scientific and life problems, for giving me hope and forcing me to believe in myself. My special thanks to Prof. Antonella Parisini for sharing her experience and providing me a great scientific support.

I want to thank all those who helped me to open a new world of experimental research and contributed to my study: Prof. Salvatore Ianotta, Dr. Svetlana Erokhina, Prof. Claudio Ferrari, Dr. Sara Beretta, Dr. Oleg Gnezdilov and Prof. Laura Pastorini.

I also would like to say thanks to my new and old friends, who brightened my stay away from home and gave me a great moral support - Carlo, Stefano, Adelya, Roma and Vale.

And of course, thanks to my big family, and especially to Marsic, who patiently went all through good and bad times with me, did not doubt me for a second, and supported me at every step of my journey.